INL/RPT-23-75961
Revision 0

Nuclear-Driven Chemical Conversion Pathways

December 2023

Byung-Hee Choi, Eliezer A. Reyes Molina, Maria A. Herrera Diaz, Elizabeth K. Worsham, Levi M. Larsen, Haydn C. Bryan, L. Todd Knighton, Richard Boardman

Idaho National Laboratory

IES
Integrated Energy Systems

INL is a U.S. Department of Energy National Laboratory operated by Battelle Energy Alliance, LLC

INL/RPT-23-75961
Revision 0

Nuclear-Driven Chemical Conversion Pathways

Byung-Hee Choi, Eliezer A. Reyes Molina, Maria A. Herrera Diaz, Elizabeth K. Worsham, Levi M. Larsen, Haydn C. Bryan, L. Todd Knighton, Richard Boardman
Idaho National Laboratory

December 2023

Idaho National Laboratory
Integrated Energy Systems
Idaho Falls, Idaho 83415

http://www.ies.inl.gov

Prepared for the
U.S. Department of Energy
Office of Nuclear Energy
Under DOE Idaho Operations Office
Contract DE-AC07-05ID14517

Page intentionally left blank

EXECUTIVE SUMMARY

With the seemingly inevitable decline in coal power plant generating capacity on the U.S. grid, there is interest in investigating transitioning coal power plant sites to nuclear power plant (NPP) sites. Closing coal-fired power plants and mining infrastructure would have a social and economic impact on the surrounding communities. Additionally, coal is a valuable domestic carbon resource. This study analyzes the feasibility of building an NPP and "coal refinery" on the sites of currently existing coal power plants. These "coal refineries" could use nuclear energy to convert the coal to nonfuel carbon-based commodity products. This pathway would facilitate transitioning the mining and coal industry to a clean industrial base in which coal is used to produce needed commodity products and the CO_2 generated is sequestered into the end products.

The purpose of this work is to explore the possibilities of using coal as a carbon resource in a "coal refinery" by converting the coal to fuels and chemicals using energy provided by an NPP. While other studies have focused on coal gasification, which requires combusting a portion of the coal to produce heat, this study implements a choice of pyrolysis over gasification, thus preserving the energy content in the coal for conversion to end products. Nuclear heat can be supplemented where needed instead of combusting the carbon. Coal pyrolysis also results in a large portion of solid char, which can be converted into activated carbon (AC) and sold to various markets. This study also uses hydrogen, produced by high-temperature steam electrolysis (HTSE) using nuclear-supplied heat and electricity, to be combined with the synthesis gas (syngas) (CO and H_2) stream from the pyrolysis unit to make methanol, which has many pathways for further processing into fuels, chemicals, and plastics. This study focuses on methanol pathways to nonfuel products, specifically polymers. CO_2 captured within the refinery model can also be combined with hydrogen to make chemical products and reduce CO_2 emissions. Demonstrating a coal conversion to methanol and AC presents a low greenhouse-gas -emitting pathway to utilizing coal. Figure ES-1 shows the block flow diagram for the processes analyzed in this study.

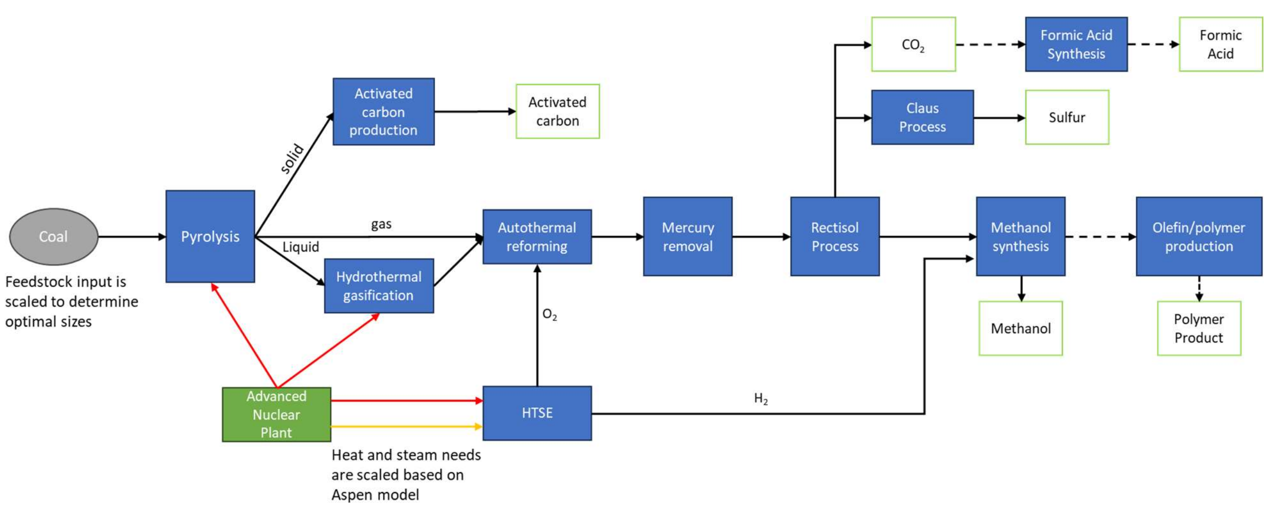

Figure ES-1. High-level flowsheet of the carbon conversion process.

Coal is used in this system model as a carbon feedstock, the building block of the products at the refinery. Not shown in Figure ES-1 are the necessary pretreatment steps performed on the coal, such as drying and crushing. Pittsburgh #8 bituminous coal is assumed here, as the target region for economic development is the Appalachian Mountain region. In pyrolysis, the coal is broken down in the absence of oxygen into solid products (char and ash), liquids and heavy hydrocarbons (tar and oil), and gas (syngas and CO_2). The liquid stream, including tar, is sent to hydrothermal gasification process, where heavy compounds such as tar are further broken down into syngas. This step is necessary as markets for tar are shrinking, so tar is more valuable converted to a gas product than as a marketable byproduct on its own. The solid products are converted to AC in a steam activation process. The activation process is exothermic, so heat is generated along with the AC product and a stream of syngas. All the generated syngas is combined in autothermal reforming, which converts the excess CH_4 in the syngas stream to CO_2 and H_2. Mercury is removed by electrostatic precipitation (ESP) configuration and selective catalytic reduction (SCR), which are industry-standard processes. The Rectisol process removes CO_2 from the syngas stream, which is recycled as a transport gas in the pyrolysis process as well a stream for carbon conversion to formic acid (FA). The Claus process removes sulfur from the gas stream and condenses it to a solid form, so it can also be sold as a product if captured in sufficient quantities. The clean syngas stream is converted to methanol and can be further converted to produce polymers, which is not modeled. The system also includes an NPP that provides heat to the process and to the HTSE plant, where hydrogen is used for the methanol synthesis process and FA production.

Markets for coal refinery products were identified through a market analysis that considered the size of the market, price, and expected market growth. Other insights about each potential market were considered, including recent events and market forces. The research focuses on markets in the United States but also includes global statistics and utilizes the most recent data available—generally 2020 or later. Additionally, this paper includes and discusses historical trends in product pricing and other key metrics An objective of this study was to ensure that the maximum amount of CO_2 produced had a final disposition in end products and was not released to the environment. The most favorable markets determined by this previous study for CO_2 utilization were FA and urea. FA synthesis is a technically simplistic process requiring only CO_2 and hydrogen, which are both produced in the current coal refinery model. FA production through CO_2 hydrogenation is gaining interest as a hydrogen fuel carrier, which may result in market growth for this product.

Urea production is not included in this analysis but could be included in future work. It is a slow-release commercial fertilizer used extensively to increase agricultural food production yields. It is another large market with expected growth due to inevitable global population increases. Urea synthesis is currently the largest market for CO_2 use in the U.S. It is synthesized by reacting ammonia and CO_2. Two of the feedstocks needed for urea and FA production (CO_2 and H_2) are produced in the coal refinery, as modeled in Figure ES-1. Future work could include an air separation unit to produce the nitrogen for producing the ammonia needed for urea production.

For methanol pathways, the main area of focus in this study is olefin and polymer production. Polymers are a large market, and even with many industries shifting away from single-use plastics, there is still a need for plastics in the medical and food industries. As the overall goal of the coal refinery is to utilize coal while effectively managing emissions, converting coal to plastics ensures that the carbon will be sequestered indefinitely, as opposed to fuels that would eventually be burned, releasing CO_2 emissions that would need to be managed.

An Aspen Plus process model was completed with the hypothetical configuration already described. At this point, only a process model study was done, and this work does not include an economic analysis. The inputs and outputs from the modeling results on a mass basis for the coal refinery are given in Table 1. Results from the modeling of this coal refinery show that, for every 1,000 tons of coal per day used as feedstock, 339 tons of AC and 398 tons of methanol are produced. Methanol yields could be increased by recycling the offgases produced from AC production. Table 1 gives the energy requirement for each unit.

Table 1. Mass and energy balance.

Unit [tonne/day]	IN	OUT
Coal	1,000	—
AC	—	339
Ash	—	102
CO_2	—	428
Water	7,632	7,546
Oxygen	478	—
Hydrogen	24	—
Light Gas	—	532
Methanol	—	398
Sulfur	—	~2
$HgCl_2$	—	Small
Unit [MW]	IN	OUT
Heat	23	83
Electricity	24	—

While the process is technically feasible, based on the capacity of 1,000 tpd coal, the amount of CO_2 produced is also too large to be converted into a single market. 420 tons of CO_2 would be converted into over 500 tons of FA per day, which is 25% of the market annually. This production rate would require an additional 31 tpd H_2 capacity, more than doubling the already large energy requirement. Additional markets should be explored, including large markets like urea and pure CO_2 product markets.

The 24 tpd hydrogen demand from methane would require 35.3 MW-e and 6.1 MW-t of the NPP capacity to produce hydrogen. NPP-generated hydrogen through NPP is used to shift the syngas to the proper carbon monoxide to hydrogen ratio for methanol production. This is done in place of using a water-gas-shift reactor. Adding in the FA production would increase hydrogen demand to 55 tpd and the NPP capacity to 80.9 MWe and 13.9 MWt. An additional 6.3 MWe would be required for FA production equipment. The energy balance in Table 1 suggests that the refinery could sustain itself on internal process heat, as 83 MWt are generated mainly from AC production and 23 MWt are required in the refinery total. The heat from AC generation could also be recovered to generate steam for the HTSE process, lowering the thermal load on the NPP. The refinery also requires 24 MWe to run equipment like pumps and compressors. When added to the electric requirement to generate hydrogen and FA, the minimum total electric load is 59.3 MWe. This is only a small portion of the typical small modular reactor (SMR) size (300 MW), indicating that there is a potential for the carbon refinery to share its NPP load with other processes or applications. If only an electric load is required, this could be supplied by most SMR designs, especially lower temperature, light-water designs.

These results show that a carbon refinery such as this one should only be done on a small scale. A technoeconomic analysis would give an optimum size for energy requirements and market capacity. Between West Virginia and Pennsylvania, two of the largest coal producers in the Appalachian region, there is 19.3 GW of coal-fired power plant capacity. The coal requirement to produce that electricity is about 173,700 tons of coal per day. From these results, carbon conversion through this refinery method would not be enough to replace the current coal use in the region. Rather, coal conversion to products should be one of several solutions considered to replace coal-fired power plants.

Future work also includes optimizing the refinery to make use of internal heat generation, rather than relying solely on the NPP. While pyrolysis consumes the most heat of any of the process units, the AC process releases a significant amount of heat that could be recycled to heat the pyrolysis unit and other heat-consuming processes. This would significantly reduce the heat duty from the nuclear reactor. In previous Idaho National Laboratory studies on coal pyrolysis, a portion of coal was gasified to provide high-temperature heat to the other processes. The AC process is similar to coal gasification but preserves much of the carbon over the goal of total gasification. These results are important for future iterations of this study. Reducing the nuclear heat load through AC production and a portion of coal gasification could lower overall costs when sizing the reactor. Additionally, the temperatures obtained through coal gasification are higher and could increase the syngas yield from pyrolysis. A full technoeconomic analysis would need to be performed to determine the optimized benefits of using coal gasification.

Page intentionally left blank

CONTENTS

FIGURES

TABLES

ACRONYMS

AC	activated carbon
ASTM	American Society for Testing and Materials
CFPP	coal-fired power plant
CPD	chemical percolation devolatilization
ESP	electrostatic precipitation configuration
FA	formic acid
FC	fixed carbon
FF	fabric filter
FOM	figure of merit
HTG	hydrothermal gasification
HTSE	high-temperature steam electrolysis
INL	Idaho National Laboratory
NC	nonconventional
SCR	selective catalytic reduction
SEP	separation
STOIC	stoichiometric
VM	volatile matter

Page intentionally left blank

Nuclear-Driven Chemical Conversion Pathways

1. INTRODUCTION

This report communicates the results of modeling and simulation efforts made toward nuclear-driven chemical conversion processes using coal as a feedstock. Modeling was completed on converting coal to methanol using pyrolysis and hydrothermal gasification (HTG). Olefins and polymers modeling was not completed at this time. Market analysis of chemical and carbon dioxide (CO_2) synthesis products, including ammonia and urea, is included first, followed by a detailed description of the modeling efforts and results. The following subsections describe the project goals, along with the high-level results.

The initial modeling work for this work package consists of a "carbon refinery" setup to convert coal to a variety of valuable, non-fuel products. The flowsheet in Figure 1-1 has been developed to meet the goals outlined in the following sections. Each goal is associated with a figure of merit (FOM), which is either qualitative or quantitative to measure the success of the model results.

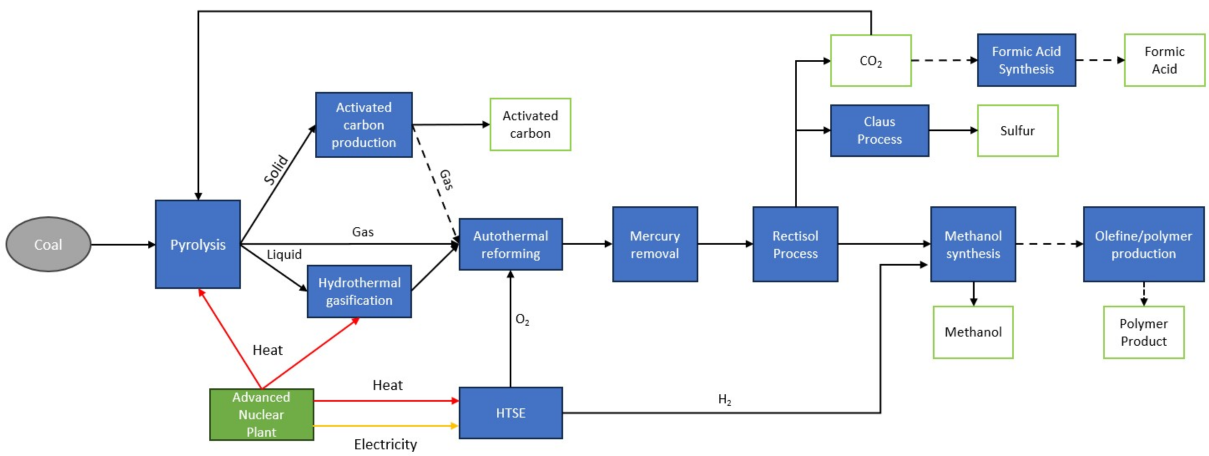

Figure 1-1. High-level flowsheet of the carbon conversion process.

Section 4 of this report describes the modeling performed for each of these individual processes. Specifically, this includes information on coal drying and pyrolysis, HTG, activated carbon (AC) production, the Rectisol process, and methanol synthesis. For more technical information on these processes and the decision-making process involved in their selection, reference *Design for Carbon Conversion Product Pathways with Nuclear Power Plant Integration* by Worsham et al. (2022).

1.1 Objectives

The initial modeling work for this work package consists of a "carbon refinery" setup to convert coal to a variety of valuable, nonfuel products. The flowsheet in Figure 1-1 has been developed to meet the goals outlined in the following sections. Each goal is associated with a FOM that is either qualitative or quantitative to measure the success of the model results.

1.1.1 Include Coal to Products Models in the HYBRID Library

Idaho National Laboratory (INL) researchers have performed several extensive technoeconomic studies or technical evaluations (TEVs) on coal gasification and pyrolysis to convert subbituminous coal to fuels and chemicals. While this report is not repeating work performed in these studies, they contain modeling of some standard process models, like Rectisol for CO_2 removal, Claus for sulfur removal, and methanol synthesis, that are leveraged in this study. The outputs of these models can also be used for verification independently from the coal feedstock used because they depend on the post-pyrolysis gas compositions. In addition to the previous INL studies, the models can be verified using the extensive literature on the thermal decomposition of different coal types, and more specifically, the Pittsburgh #8 coal we are targeting in this study.

In addition to technical validation, using standardized processes and equipment is important for the future economic analysis. Processes like Rectisol were already deployed on a full scale by the time these INL studies were performed, and thus, the prices listed in the TEV are likely still accurate after adjusting for inflation and comparing to recent estimates.

The model validation will be documented so that these process models can be added to the HYBRID library in the Framework for Optimization of ResourCes and Economics. The open-source models can then be used for future internal and external case studies. The FOM for this goal is shown in Equation 1.

$$FOM = All\ models\ successfully\ imported\ to\ HYBRID \tag{1}$$

Section 3 of this document validates each model in HYBRID. Future model users can refer to this document to understand how and why the models were designed and the assumptions and prior data that were used to build and validate them. These models are open source, meaning they can be utilized by the general public as well as in future INL case studies.

1.1.2 Convert Coal to Nonfuel Products

Much of the current research on coal devolatilization focuses on converting coal to other fuel sources that are purer, burn cleaner, and make carbon capture easier. This study aims to demonstrate the viability of converting coal into nonfuel products as an alternative to CO_2- and energy-intensive methods required to produce chemicals, plastics, fertilizers, and more. The end use of these products also does not typically result in CO_2 emissions that will need to be controlled at the use point.

In this study, the market options come from the conversion of coal to synthesis gas (syngas) generated by coal pyrolysis and HTG, which is converted to methanol. Methanol is a valuable product on its own, but it can also be further processed into a variety of chemicals. The CO_2 captured from the syngas can be combined with additional hydrogen and other materials to form valuable chemicals, carboxylic acids, and fertilizers.

The exploration of these pathways during this project has created documentation on the size of markets, global and regional producers, and the probability of a small producer succeeding in this market. These market analyses have helped us make decisions on the product pathways to pursue in this case and determine which markets should be targeted in future cases. The FOM for this goal is the net present value (NPV) of the coal refinery, shown in Equation 2:

$$FOM = NPV_{refinery} \tag{2}$$

Although there is not a quantitative value associated with the product markets, Section 3 details the market analysis of many potential products for a carbon refinery. Nuclear-driven chemical conversion processes will continue to be a priority for future research, even if coal is not used as the feedstock.

1.1.3 Maximize Byproducts Utilization

Maximum utilization of byproducts is targeted first to minimize the costs associated with the offsite transportation and disposal of the byproducts. Second, by utilizing byproducts internally, the overall carbon intensity of the whole operation can be minimized. Lastly, internal utilization can lead to lower overall plant operating costs. This is especially true of AC, a very effective sorbent for mercury in flue gas; however, the barrier to its use is mainly the cost of the material. CO_2 is also considered a waste product in this process, but it is converted to formic acid (FA) instead of being sequestered or released into the atmosphere. The FOM for this goal is shown in Equation 3:

$$FOM = (Levelized\ Cost\ of\ AC + Revenue\ of\ AC\ Sold) - Cost\ to\ purchase\ AC \quad (3)$$

Through modeling efforts, we determined that mercury removal by AC was not the most effective method. Instead, the SCR with electrostatic precipitation configuration (ESP) was studied as the most convenient technology due to its targeted emission reduction, high efficiency, wide applicability, long-term stability, environmental benefits, and regulatory compliance, especially in industries where elemental mercury and nitrogen oxides (NOx) emissions are a significant concern.

Some of the advantages of SCR/ESP over AC technologies considered for mercury removal are:

1. Targeted Emission Reduction:
   - SCR is primarily used for reducing NOx emissions along with the catalytic oxidation of elemental mercury (Hg^0), which are harmful air pollutants. SCR is highly effective in oxidizing Hg^0 into its oxidized form (Hg^{2+}) or particulate-bound mercury (Hg^p) and reducing NOx to nitrogen and water.
   - AC is mainly used for adsorbing volatile organic compounds and other organic pollutants but is less effective in NOx and Hg^0 removal. Surface functionalization of the solid substrate led to a further implementation of toxic systems (e.g., acid/alkaline or amine functionalization), increasing the operational cost.
2. High Efficiency:
   - SCR systems can achieve high elemental Hg oxidation and NOx removal efficiency, often exceeding 90% in both cases.
   - AC systems may have variable efficiency depending on the specific surface functional groups as well as the pollutants restrained in the gaseous stream and conditions (temperature and pressure) and may not be as effective for Hg^0 removal.
3. Wide Range of Applications:
   - SCR technology is widely employed in power plants, industrial boilers, and diesel engines to meet stringent emission regulations.
   - AC is primarily used for air and water purification, odor control, and solvent recovery, making it less suitable for Hg^0 and NOx reduction in many industrial processes.
4. Long-Term Stability:
   - SCR catalysts can provide stable performance over an extended period when properly maintained.
   - AC beds need frequent replacement or regeneration, leading to higher operational costs due to their short lifespan.
5. Environmental Impact:
   - SCR reduces Hg^0 and NOx emissions without producing additional waste or byproducts.
   - AC adsorption generates spent carbon, which requires disposal or regeneration processes, potentially contributing to environmental impacts.
6. Regulatory Compliance:
   - Many emission control regulations and standards specifically recommend or require SCR technology for Hg^0 and NOx reduction in certain industries.
   - AC may not always meet the stringent requirements of emissions standards for both Hg^0 and NOx control.

1.1.4 Perform a Cost Comparison of Using Light-Water Reactors and High-Temperature Gas Reactors for High-Temperature Processes

INL is releasing a new open-source tool to estimate the cost of advanced nuclear reactor technologies. This tool will be used to estimate the cost of the reactor based on the heat and electricity requirements of the coal refinery. Using a high-temperature gas reactor would not require any heat topping for steam to be input into the HTG process and recovered for lower temperature processes. A light-water reactor would have to be scaled to account for heat topping provided by either direct electric heating or hydrogen combustion. The FOM for this goal is shown in Equation 5. This analysis is deferred to other studies currently in progress with a hyperfocus in this area.

$$FOM = NPV_{LWR} - NPV_{HTGR} \tag{5}$$

2. MARKET ASSESSMENT

Fully exploring the opportunities presented by nuclear combined heat and power involves not only an understanding of the technical requirements of a given process but also of the product's market. This paper examines the market dynamics for various products currently being examined for production integration with nuclear power, placing a specific focus on the competitive forces that shape market pricing and demand. The products examined in this report are ammonia, urea, oxygen, AC, and FA. The market dynamics studied include price history, demand influences, and recent technological advances. Table 2 and Figure 2-1. Recent price histories of select study products (Business Analytiq 2023a; b; c; d).

display basic statistics and trends for the studied materials.

Table 2. Basic information on studied markets.

Summary Statistics						
Market	Price		Global Production or Consumption		CAGR	
Ammonia	\$530/mt	Sept. 2023[1]	150 MMT	2021[2]	1.0%	2020–2050[3]
Urea	\$350/mt	Sept. 2023[4]	180 MMT	2021[2]	1.3%	2020–2050[3]
Oxygen	\$0.13/Nm^3	Jan. 2018[5]	380 MMT	2018[6]	8.4%	2023–2033[7]
AC	\$4220/mt	Sept. 2023[8]	5.8 MMT	2022[9]	6.0%	2023–2028[10]
FA	\$780/mt	Sept. 2023[11]	0.75 MMT	2022[12]	4.5%	2022–2035[12]

SOURCES:
1. Business Analytiq 2023b
2. Statista 2023a
3. International Energy Agency 2021
4. Business Analytiq 2023d
5. Intratec 2023
6. GlobeNewswire 2019
7. Future Market Insights 2022
8. Business Analytiq 2023a
9. Statista and AgileIntel Research 2023
10. Mordor Intelligence 2023
11. Business Analytiq 2023c
12. ChemAnalyst 2023

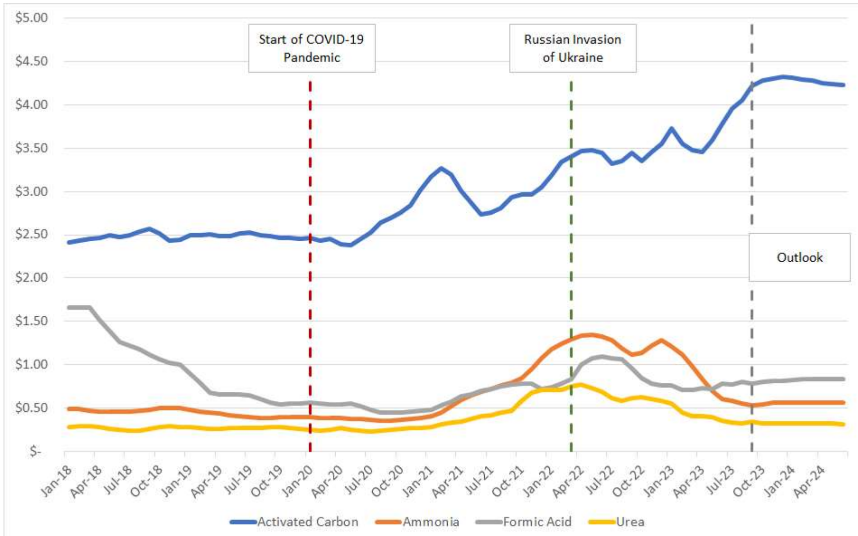

Figure 2-1. Recent price histories of select study products (Business Analytiq 2023a; b; c; d).

2.1 Ammonia and Urea

Ammonia (NH_3) is a colorless gas and an important precursor for many products, including fertilizers, pharmaceuticals, and chemicals. Urea ($CO(NH_2)_2$) is one such ammonia-based product and is a highly soluble, nontoxic compound used to produce fertilizers, resins, and medical products. Both ammonia and urea are critical for the agricultural sector that relies on nitrogenous fertilizers to maintain productivity. An ammonia fertilizer typically has a higher nitrogen content than urea fertilizer, with nitrogen accounting for up to 82% of its weight. Urea fertilizer, on the other hand, typically contains around 46% nitrogen (International Energy Agency 2021).

2.1.1 Supply

Ammonia is traditionally produced through the Haber-Bosch process, which combines nitrogen and hydrogen gases under high pressure and temperature, using a catalyst to promote the reaction between the gases. Urea is produced through additional processing where carbon dioxide is reacted with ammonia.

Many countries produce ammonia, with China, Russia, and the United States together accounting for nearly half (48%) of global production (International Energy Agency 2021). About 10% of ammonia produced is traded internationally, meaning that 90% of global consumption is produced by the consumer country. By contrast, 28% of urea is traded in global markets—the higher percentage is partially attributable to urea's relative innocuousness compared to ammonia, which makes the material safer and easier to transport and handle. Figure 2-2 shows that the global production of the two products has generally increased, with a slight dip between 2014 and 2018.

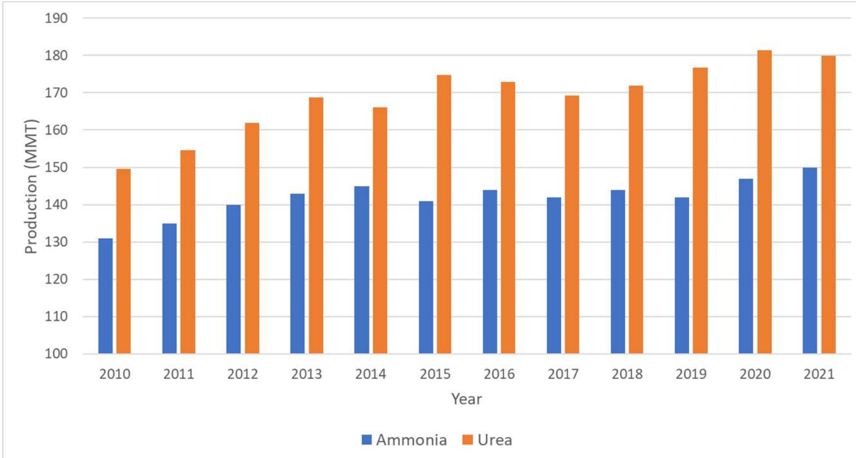

Figure 2-2. Global production of ammonia and urea (Statista 2023a).

Domestic production of ammonia and urea is relatively concentrated, with only 17 and 10 firms producing each of the products, respectively. CF Industries Incorporated is the largest producer of each, constituting 40% of ammonia and 50% of United States urea production. Current domestic production of the products totals 18.1 million metric tons (MMT) of ammonia and 12.4 MMT of urea a year (Nutrien 2022). Production is also relatively geographically concentrated, with Louisiana, Oklahoma, Texas, and Iowa producing 68% and 71% of ammonia and urea, respectively (Nutrien 2022). This concentration is primarily due to the large reserves of natural gas in those states. Figure 2-3 displays the production capacities of the largest U.S. companies, showing the dominance of CF Industries in the space.

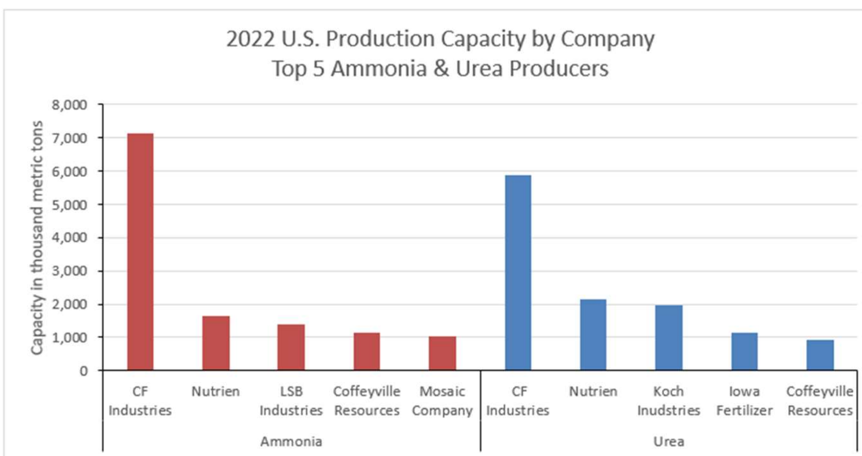

Figure 2-3. 2022 U.S. production capacity by the top five ammonia and urea producers (Nutrien 2022).

2.1.2 Demand

As discussed previously, the primary demand for both ammonia and urea is fertilizers, constituting 70 and 80% of their utilization, respectively. As such, the demand levels for these compounds are primarily determined by forces in the agricultural industry. Figure 2-4 provides a visual representation of the ammonia supply chain, showing the initial feedstocks and final products within the industry.

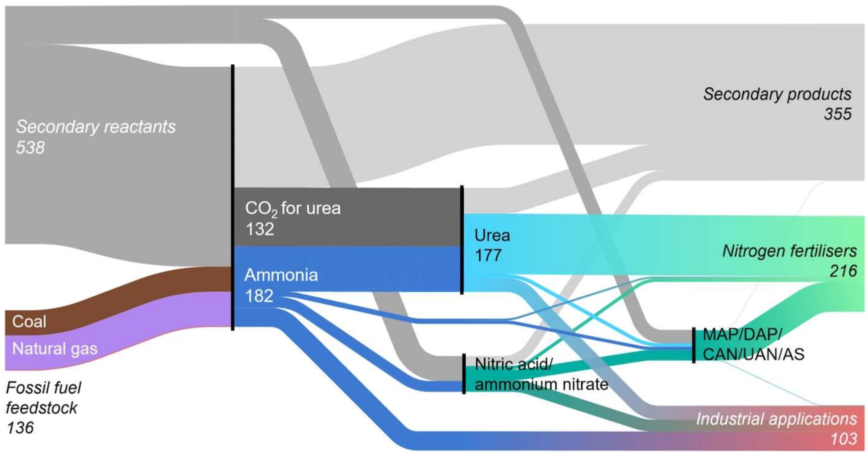

Figure 2-4. Mass flows in the ammonia supply chain: from fossil fuel feedstocks to nitrogen fertilizers and industrial products. Units are millions of tonnes per year based on data from 2019. MAP = monoammonium phosphate; DAP = diammonium phosphate; CAN = calcium ammonium nitrate; UAN = urea ammonium nitrate; AS = ammonium sulfate.

Demand for nitrogenous products, such as ammonia and urea, has increased in recent years. Since 2010, nitrogen global demand has grown roughly 1.7%. Fertilizer nitrogen[1] demand grew at an average rate of 0.9% while non-fertilizer nitrogen demand grew an average of 4% per year (International Energy Agency 2021). Within the U.S., demand growth is relatively similar. Figure 2-5 highlights the changes in demand for nitrogen fertilizer between 2000 and 2020, showing that consumption has increased overall since 2000 but has experienced significant volatility and slower recent growth.

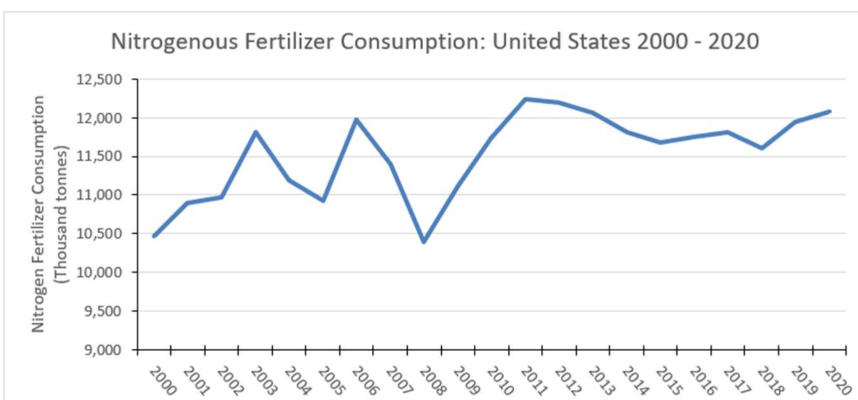

Figure 2-5. Nitrogenous fertilizer consumption in the United States 2000–2020 (International Energy Agency 2021).

---

1 Nitrogen fertilizer products encompass ammonia-based fertilizers and include ammonia, urea, ammonium nitrate, calcium ammonium nitrate, urea ammonium nitrate, diammonium phosphate, monoammonium phosphate, and ammonium sulphate.

The *Ammonia Technology Roadmap* report, produced by the International Energy Agency, projects that global fertilizer and nonfertilizer nitrogen demand will grow at a rate of 1 and 1.3% per year, respectively, between 2020 and 2050 (International Energy Agency 2021). Changes in fertilizer demand are typically driven by multiple factors, including population growth, pricing, rain levels, and shifts in crop type popularity. Unexpected shifts to any of these factors can also change future demand expectations.

2.1.3 Market Statistics

Figure 2-6 and Figure 2-7 show recent price data for ammonia and urea, respectively, which will be discussed more fully in the context of fertilizers, for which each are primary feedstock materials.

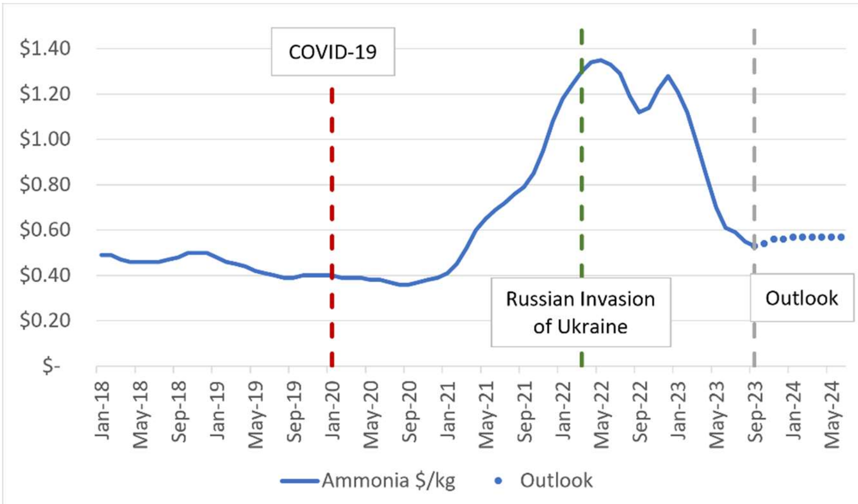

Figure 2-6. Recent ammonia price trend and outlook (Business Analytiq 2023b).

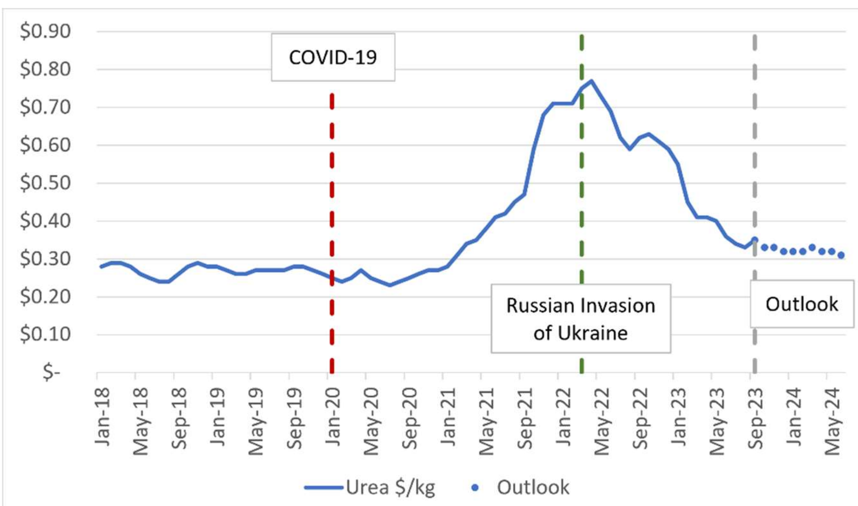

Figure 2-7. Recent urea price and outlook.

Figure 2-8 shows the changes in nitrogen fertilizer prices between 2007 and 2022. The two largest variations in price come first in 2008 during the Great Recession and second shortly after the global spread of COVID-19. Each of these disruptions caused significant spikes in fertilizer prices. Excluding the outlier events, the average global price per metric tonne (U.S. dollar [USD] per pound of nitrogen) in that period was $279 ($0.30) for urea and $383 ($0.23) for ammonia. During said period, the maximum price was $846 ($0.92) for urea and $1,076 ($0.66) for ammonia, and minimum price was $181 ($0.20) for urea and $249 ($0.15) for ammonia (Baffes and Koh 2022).

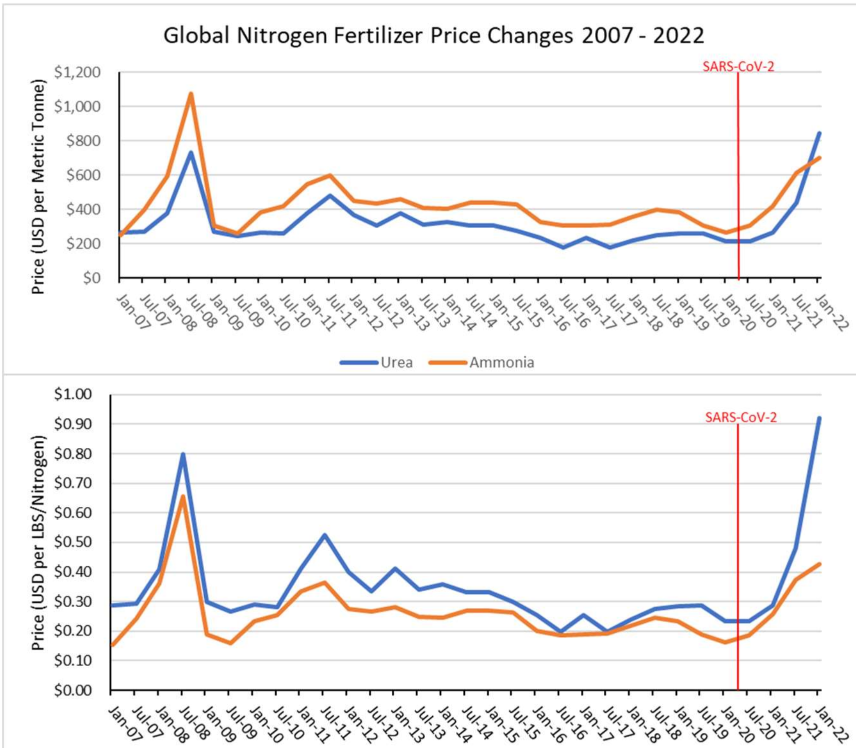

Figure 2-8. Global nitrogen fertilizer prices 2007–2022 (Baffes and Koh 2022)[2].

Currently, prices have further been impacted (on top of the effects of COVID-19) by the Russian invasion of Ukraine, which led to significant sanctions by the United States and many other countries against Russian goods, including fertilizers. Figure 2-8 shows the U.S. nitrogenous fertilizer price index between 2015 and 2023[3]. On the chart, red lines are used to denote the start of the COVID-19 pandemic as well as when sanctions on Russia begin. According to a Reuters article from 2022, prior to sanctions, Russia accounted for 22% of ammonia exports globally and 14% of urea exports (Polansek and Mano 2022). Another major contribution to ammonia and urea prices is the price of natural gas. Due to its role as a primary feedstock in the hydrogen production method, the rise and fall of natural gas will also play a significant role in price of nitrogenous fertilizers[4] (DOE 2022).

As previously noted, both ammonia and urea have additional applications apart from fertilizers. While these uses represent a minority share of consumption for each, shifts in demand in these smaller markets can still impact prices. However, price shifts driven by nonfertilizer markets will likely be minimal because usage is predominantly driven by the agricultural industry. It is also possible that demand, and thus prices, could shift if ammonia were to be used in new markets. For example, a 2021 article in

---

2 Price is represented both as USD per metric tonne (top chart) and USD per pound of nitrogen (bottom chart).

3 Nitrogenous fertilizers in this data set include synthetic ammonia, nitric acid, ammonium compounds, and urea.

4 In the United States, 95% of hydrogen is produced via natural gas steam methane reforming.

Chemical Engineering News details the potential for ammonia to be used as a fuel (Tullo 2021). The article explains that while it is hypothetically possible to use ammonia in marine engines, the technology is still far from broad application. Should such engines be developed, demand for ammonia could increase significantly. New markets would increase the incentive for existing producers to ramp up production and new producers to enter the industry.

Figure 2-9 and Figure 2-10 show the net trade flows for ammonia and urea, respectively. Russia is the largest net exporter of ammonia, at \$1.79B, while India was the largest net importer, at \$1.42B. The United States exported \$192M and imported \$1.46B in 2021, for a trade value delta of −\$1.26B (Observatory of Economic Complexity 2021b). Russia and India were also the largest exporter and importer of urea in 2021, respectively, with Russia exporting \$2.49B and India importing \$3.4B. The United States exported \$157M and imported \$2.15B for a trade value delta of −\$1.99B (Observatory of Economic Complexity 2021d).

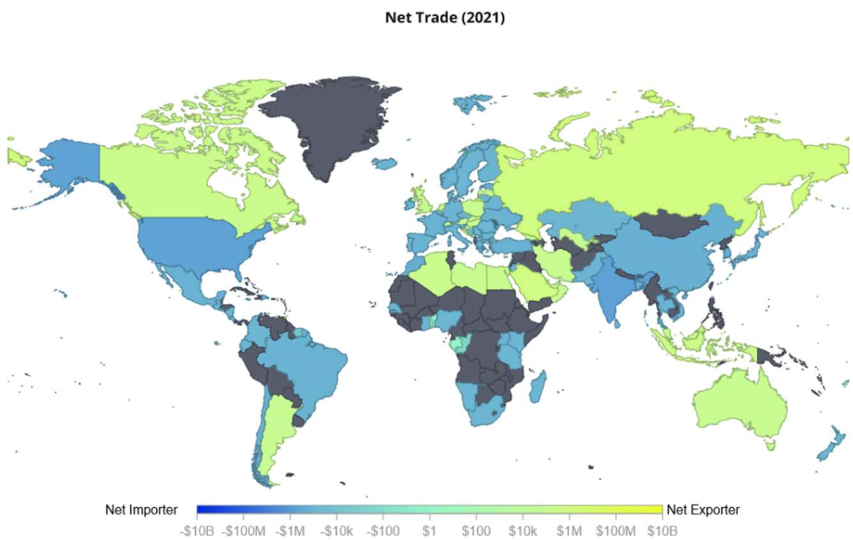

Figure 2-9. Global ammonia trade (Observatory of Economic Complexity 2021b).

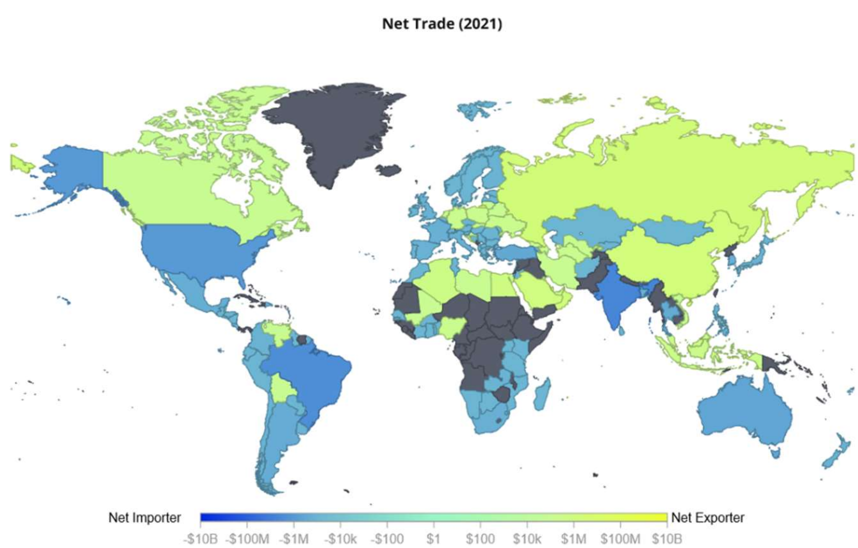

Figure 2-10. Global urea trade (Observatory of Economic Complexity 2021d).

2.1.4 Discussion

With the above analysis as context, we concluded the following about the ammonia and urea markets:

- Prices for ammonia and urea appear to be relatively stable outside of extraordinary events, such as recessions, wars, and pandemics. Thus, producers must be able to manufacture at or below historical averages to be competitive.
- Demand for both ammonia and urea are not expected to see substantial gains soon. Growth is projected to be slow and steady, and barring any technological developments that open new markets, it is not expected to see major swings in the next 25 years.
- Competition in both markets is strong. In the United States, ammonia is produced by 17 firms, with a single firm dominating the national plant capacity. Urea faces even stronger competition with only 10 producers nationally, and with one firm dominating production. Companies looking to enter one of the two industries would likely find more success entering the ammonia market due to lower monopolistic forces.

2.2 Oxygen

Oxygen (O_2) is an essential gas widely used in industrial and medical applications. These uses include steelmaking, chemical oxidation, and glass production. Different applications of oxygen require varying degrees of purity, with many industrial processes utilizing a standard 93% (N2.3) purity while some research applications require 99.999% (N5.0) purity. Isolating higher-purity oxygen is more expensive and energy intensive, increasing both the production costs and potential sale price of the product.

2.2.1 Supply

Oxygen is typically produced on an industrial scale through cryogenic distillation. This process involves cooling air to very low temperatures, around −183°C, and separating the components of the air using distillation columns. The air is compressed, dried, and then cooled to remove carbon dioxide (CO_2), water vapor, and other impurities. The remaining air is separated into its components, mainly nitrogen and oxygen, using a cryogenic distillation column. Oxygen is then further purified through adsorption or other means to remove any remaining impurities before being compressed and stored in tanks for distribution. Other methods of industrial oxygen production include water electrolysis and the partial oxidation of hydrocarbons.

The five largest producers in the United States are Matheson, Airgas, Cobham Mission Systems, Air Products Inc, and Praxiar, Inc. (Thomas Publishing 2023).[5] According to research from the National Energy Technology Laboratory, the "air separation market is dominated by a small number of highly competitive companies who are willing to offer lump-sum-turnkey systems for a project or even build and operate a plant near the client's project site and supply the needed oxygen 'over the fence' under a long-term contract" (National Energy Technology Laboratory). Total U.S. demand for oxygen is particularly difficult to determine—estimates range anywhere from 100 million normal cubic meter (Nm^3) to 500 million Nm^3 and are influenced by different measurement methods.[6] The range of this demand depends on how the post-COVID-19 slump affects market prices.

---

5 The top five producers are determined by annual revenue. These five companies cleared roughly $250 million or more in a single year.

6 This range is produced by using pre-COVID-19 demand numbers as a lower bound. The upper bound is produced by converting current market capacity in USD and dividing it by the projected price used in this paper.

In 2022, it was estimated that 110 oxygen production facilities were operating across the United States, which reduces the supply chain's vulnerability to disruptions (Environmental Protection Agency 2022). Figure 2-11 shows the locations of these manufacturing facilities.

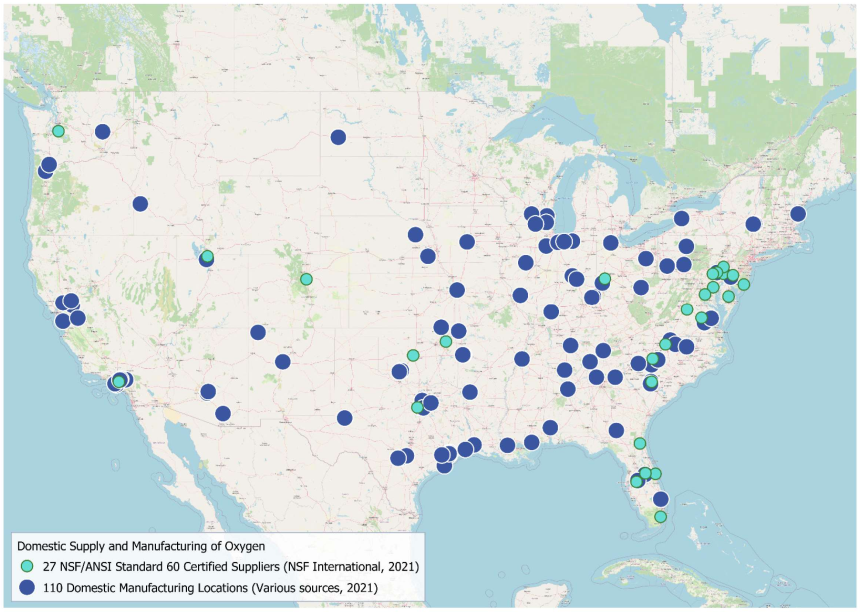

Figure 2-11. Domestic oxygen manufacturing plants (Environmental Protection Agency 2022).

2.2.2 Demand

Oxygen is primarily demanded for medical applications, pharmaceuticals, metal manufacturing, fabrication, and fuel production. The global market value for oxygen was $47.23 billion in 2022 and is expected to grow to $71.46 billion in 2028 (Statista 2023b).

While less than 5% of oxygen demand is attributable to water purification, the criticality of O_2 in some purification processes makes supply-chain disruptions a concern for the national water supply. Disruptions occurred recently due to impacts from COVID-19, which led to some water treatment plants and precursor material producers having their supply of O_2 suspended. While there is a distributed network of O_2 producers, transporting the material can be challenging given that it is classified as a hazardous material and requires labor to have additional endorsements (Environmental Protection Agency 2022).

2.2.3 Market Statistics

In January 2018, the volume weighted average transaction price for oxygen was $0.13 Nm^3 (Intratec Solutions n.d.). Figure 2-12 shows the oxygen producer price index between 2000 and August 2023, with the base set as January 2000, which shows the index saw large jumps in December 2020, April 2022, and August 2022. Much of this was driven by the massive increase in demand during the COVID-19 pandemic. In fact, a recent study focusing on shifts in demand from the pandemic estimates the total demand in the United States increased by 105% in 2020 (Bałys et al. 2021).

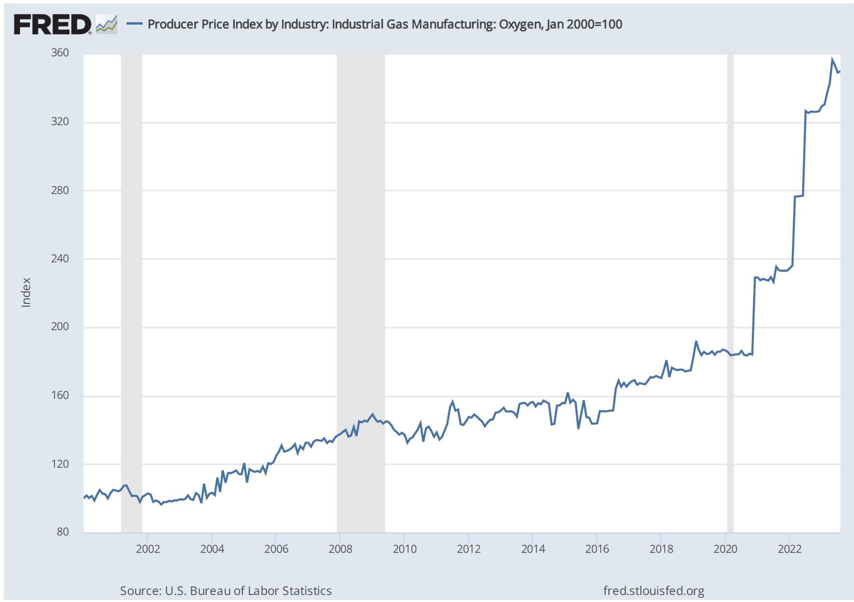

Figure 2-12. U.S. oxygen producer price index (Jan. 2000 = 100). Shaded bands represent periods of U.S. recession (Federal Reserve Bank of St. Louis 2023).

Figure 2-13 shows the global trade flows of oxygen, for which Belgium was the top exporter ($43.5 million) and Netherlands the top importer ($34 million) in 2021. The United States exported $13.4 million and imported $3.31 million worth of oxygen in 2021 for a trade value delta of $10.1 million.

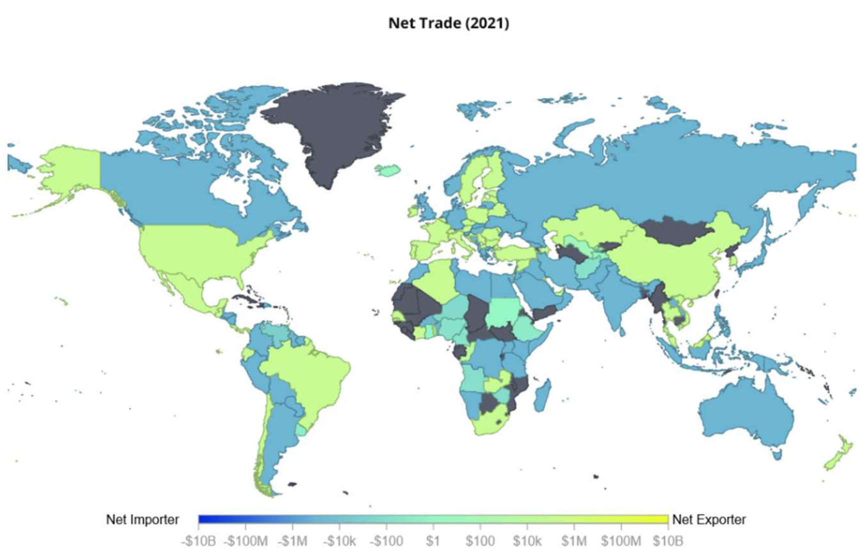

Figure 2-13. Global oxygen trade.

2.2.4 Discussion

While data availability for oxygen is limited compared to other industries, we concluded the following about the oxygen market:

- Oxygen is both widely used and produced with varying applications and production costs depending on purity.
- The industry has experienced recent supply-chain disruptions and demand fluxes due to the impacts of COVID-19 and associated shocks, which have significantly driven up the O_2 price in recent months.
- While there are many domestic production facilities, there are few production companies and startup costs are high, making the supply moderately concentrated (IBIS World 2023).

2.3 Activated Carbon

AC, also known as activated charcoal, is a highly porous material with a large surface area capable of adsorbing pollutants and impurities from liquids and gases. The product plays an important role in a variety of sectors, including water treatment, air purification, foods and beverages, and pharmaceuticals.

2.3.1 Supply

AC is produced from a variety of organic materials, including wood, coal, and coconut shells through carbonization and activation. New materials, including pecan shells, rice straw waste, and bamboo are being explored as potentially economically viable and environmentally sustainable feedstocks for the industry (Ng et al. 2003; Choy et al. 2005; Nandiyanto 2018). Carbonization is a process where an organic material is heated in the absence of air, while activation is completed through chemical or physical treatments to create a highly porous material with a large surface area. Production methods vary depending on the type of AC being produced and the intended application. Common production methods include steam activation, chemical activation, and physical activation.

AC is a unique product given its ability to be recycled. Some systems, especially large systems, regenerate used AC while adding feedstock materials to replace materials lost during operation. This can help reduce costs and help companies meet environmental regulations (Baker et al. 2000).

2.3.2 Demand

AC has a wide variety of uses, including:

- Water treatment applications to remove contaminants, such as chlorine, sediment, and organic compounds.
- Air purification applications to remove volatile organic compounds, odors, and gases.
- Food and beverage applications to remove impurities and improve taste and color in a variety of products, including sugar, beer, and fruit juices.
- Pharmaceutical applications as an adsorbent in the production of medicines and as a detoxifying agent in emergency medical treatments.

AC demand is sensitive to environmental regulations, with federal and state regulatory or legislative actions impacting the expected and actual demand over time. For example, the slate of environmental legislation enacted in 1970 (the Clean Air Act, the Clean Water Act, and the Safe Drinking Water Act) increased domestic demand (Baker et al. 2000). As such, future demand is partially dependent on changes to regulation strictness.

2.3.3 Market Statistics

Figure 2-14 shows recent AC price trends and a forecast, revealing that the product has experienced an upward trend in price since the start of the COVID-19 pandemic and continuing through the Russian invasion of Ukraine. Current prices are the highest experienced since at least 2018, though the projected outlook shows a slight reduction in price over the coming months.

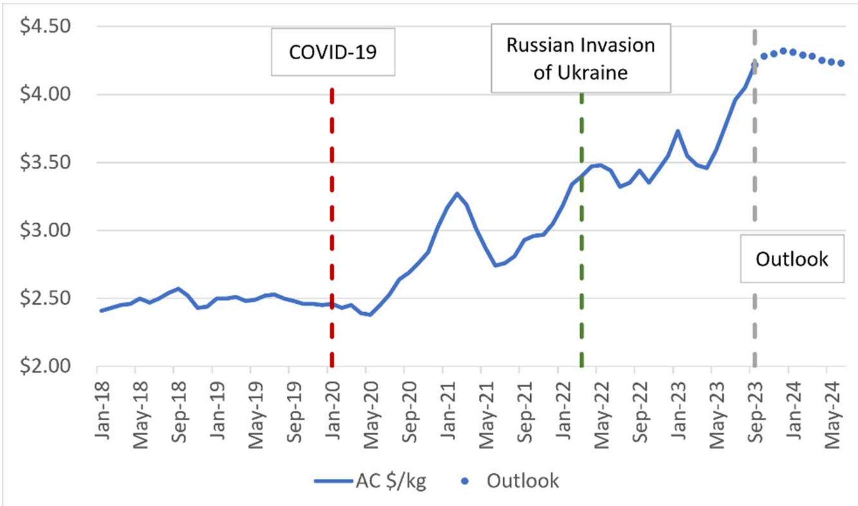

Figure 2-14. AC recent price trend and outlook (Business Analytiq 2023a).

Figure 2-15 shows global trade flows of AC by net value. In 2021, the largest exporter of AC was China, with a net export of $425 million, while South Korea was the largest net importer, at $175 million. The United States exported $404 million and imported $263 million worth of AC in 2021 for a trade value delta of $141 million (Observatory of Economic Complexity 2021a).

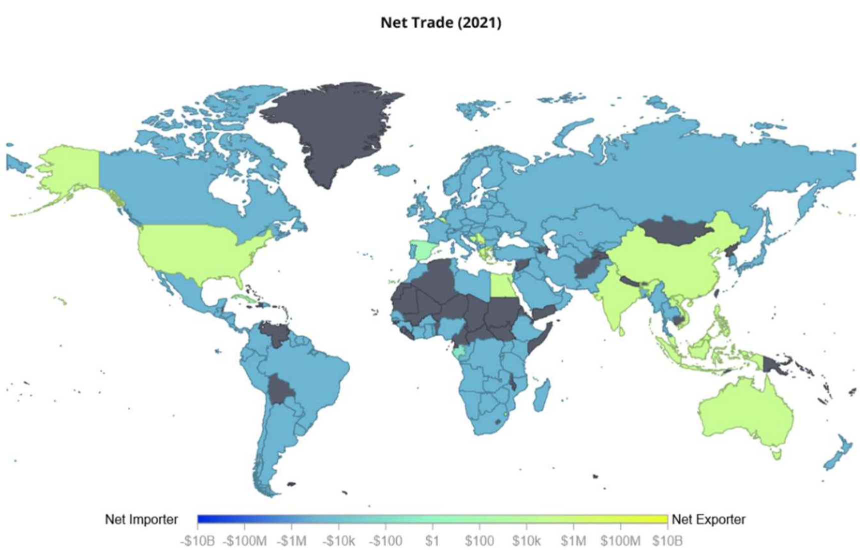

Figure 2-15. Global AC trade.

2.3.4 Discussion

With the above analysis as context, we concluded the following about the AC market:

- AC is widely used and produced but is part of multiple critical processes like water purification, meaning that supply-chain disruptions have potentially large impacts.
- Demand is impacted by the regulatory environment and could be impacted by current and future administrations.
- Recent data show the price of AC increasing, but this trend may be mitigated by introducing new production feedstocks and technologies.

2.4 Formic Acid

FA (CH_2O_2) is a colorless liquid generally produced via the BASF process described by Hietala et al. (2016) and is used in a variety of industrial and commercial applications. Its primary uses include as a preservative and antibacterial agent in livestock feed, a coagulant in rubber production, and a solvent in the manufacture of dyes and pharmaceuticals. Additionally, FA is used as a precursor in the production of other chemicals, such as formate salts and methanol. Data availability for FA metrics is limited compared to other products discussed in this report.

FA also has promising applications as an energy carrier for the transportation industry due to the material's inherent relative safety and favorable energy content. Additionally, recent studies show that pathways exist to sell FA at prices competitive with gasoline, in addition to the fact that existing fossil fuel distribution infrastructure could be upgraded at reasonable costs to instead transport FA (Eppinger and Huang 2017). Current research focus is mainly placed on using FA as a carrier to produce H_2 selectively onboard a vehicle. However, the technology currently experiences challenges with carbon monoxide (CO) production and low service distances of catalysts (Eppinger and Huang 2017).

2.4.1 Supply

As discussed above, FA is usually produced via the BASF process, which requires high pressure (4 MPa) and a relatively low temperature (80°C). FA is typically produced by oxidating methanol, which can be achieved through various methods. One common method is reacting methanol with carbon monoxide in the presence of a catalyst, such as rhodium or iridium. Another method involves reacting methanol with oxygen in the presence of a catalyst, such as silver or platinum. Additionally, FA can also be produced through the biological process of fermentation, in which microorganisms break down sugars and other organic materials and produce FA as a byproduct.

2.4.2 Market Statistics

Figure 2-16 shows the recent FA price trend, revealing that the price generally decreased between January 2018 and September 2020 and then generally increased thereafter. While it is difficult to attribute specific price phenomena to individual events, the COVID-19 pandemic and Russian invasion of Ukraine likely increased the volatility of prices and led to price increases due to supply-chain disruptions.

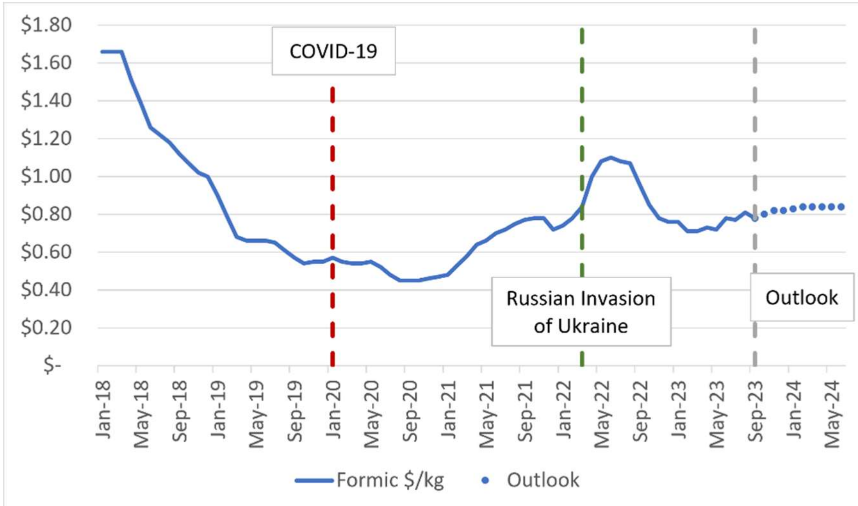

Figure 2-16. FA recent price trend and outlook (Business Analytiq 2023c).

Figure 2-17 shows the global trade flows for FA, showing that China was the largest exporter ($145 million) and Netherlands the largest importer ($37.2 million) in 2021. The United States exported $18.6 million and imported $5.6 million of FA in 2021 for a trade value delta of $13 million (Observatory of Economic Complexity 2021c).

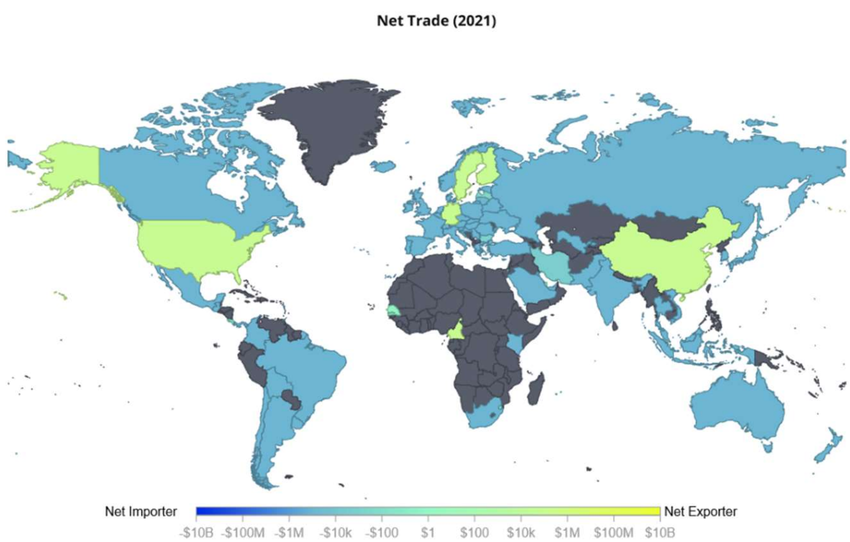

Figure 2-17. Global FA trade.

2.4.3 Discussion

A lack of data availability makes drawing conclusions about the FA market challenging—identifying and synthesizing information from reputable sources is an opportunity for future research.

3. PROCESS MODELING AND VALIDATION

This section details the progress on the current modeling efforts for the proposed coal conversion refinery. The models described in this section will be uploaded to the HYBRID library to be available as an open source for future case studies.

3.1 Coal Properties and Drying

3.1.1 Pittsburgh #8 Coal Properties

Pittsburgh #8 coal is a famous coal seam in the upper Appalachian Mountains and is broadly used as a coal sample. There are three types of component attributes for coal well defined in the American Society of Testing and Materials (ASTM) terminology document ASTM D121-15 2016 (ASTM International 2016). Proximate analysis measures the relative amount of moisture, ash, volatile matter (VM), and fixed carbon (FC) under pyrolysis. VM contains all components that leave the coal during pyrolysis, including noncondensable light gas, such as CO, CO_2, H_2, CH_4, and NH_3, as well as the aliphatic gas, oil, and aromatic tar, and steam. FC is the combustible residue after the VM is driven off. Ash remains after off-gassing of the VM and the complete combustion of the FC. The amount of ash, on a whole coal weight percent basis, is correctly referred to as the weight percent ash yield. The amount of moisture, ash, and VM is measured, and FC is calculated by subtracting these values from 100%. Ash consists of mostly inorganic leftover materials after complete combustion, such as SiO_2 and Al_2O_3. Note that ash is not same as mineral matter because clay minerals lose water, calcite loses CO_2, and pyrite loses sulfur. The Parr formula, shown in Equation 6, is a correlation to estimate the amount of mineral matter.

$$mineral\ matter\ (wt\%) = 1.08 \times ash\ (wt\%) + 0.55 \times total\ sulfur\ (wt\%) \tag{6}$$

The ultimate analysis measures the C, H, N, S, and O contents by fully burning the sample. The amount of oxygen is determined by the difference, in other words, subtracting the total percentages of carbon, hydrogen, nitrogen, and sulfur from 100%. Sulfur analysis distinguishes the type of sulfur embedded in the sample between pyritic, sulfate, and organic. Proximate, ultimate, sulfur, and element information of Pittsburgh #8 coal mined at different locations and years are summarized in Appendix D-1. One of the main distinct characteristics of bituminous coal compared to the other petroleum and bio-oils is its low atomic hydrogen-to-carbon ratio of 0.8.

The saturation vapor pressure of water in air at 25°C and atmospheric pressure is 3.1690 kPa. This model assumes ambient air relative humidity of 20%. The mole fraction of the N_2, O_2, and H_2O of air in this condition is 0.7851, 0.2087, and 0.0063, respectively. Specific humidity information for the Appalachian Mountain region was not included but could make the calculation more precise. As moisture data are often written in as-air-dried or as-determined (air-dried at a specific condition determined in ASTM D2013), extra moisture over the value of the reference was not considered at this time.

3.1.2 Model Description

In the Aspen Plus model, coal is a nonconventional (NC) solid that cannot be characterized by a molecular formula. Instead, an NC solid is expressed by its component attributes: PROXANL, ULTANAL, and SURFANAL. To employ an NC solid in Aspen Plus, the general coal enthalpy model (HCOALGEN) and Institute of Gas Technology coal density model (DCOALIGT) are selected to calculate enthalpy and density of coal particles, respectively. HCALGEN has four options to select: heat of combustion, standard heat of formation, heat capacity, and enthalpy basis. Each option code is selected as a value of one in this study, meaning the Boie correlation, heat of combust correlation, Kirov correlation, and elements in standard states are selected, respectively.

The PROXANAL, ULTANAL, and SULFANAL component attributes for NC solid coal are specified as tabulated in Table 3. The proximate and ultimate coal properties are basically specified to be consistent with Reference Case 5 from Appendix D-1, except for water, chlorine, and corresponding oxygen.

The as-received condition of coal may have a high-moisture content due to coal type, weathering, or other factors. This water must be removed to raise the coal's heating value. Introducing dry heated air can bring out water from the coal. Zero heat duty is specified on the dryer unit adiabatic condition, meaning heat transfer occurs only between the coal, air, and moisture in the air and coal. There are four references included with the moisture content for Pittsburgh #8 coal in Appendix D-1, and their average of 2.52% is specified for this model. The amount of chlorine is assumed to be 0.1 weight percent (wt%) similar to Cases 1, 2, and 4 in Appendix D-1, and the amount of oxygen is also reduced to 0.1 wt%. Sulfur properties are divided into organic and pyritic sulfur 1:1.6 as Pittsburgh #8 coal (HVAB) has organic and pyritic sulfur, approximately 1:1.55 and 1:7 in Cases 1 and 2 in Appendix D-1, respectively, and sulfate sulfur is less than 0.01% (Vorres 1998; Miller and Tillman 1998). PROXANAL, ULTANAL, and SULFANAL are the component attributes of the proximate, ultimate, and sulfur analysis, respectively, that need to be specified for each NC solid introduced to the system or produced during the reaction.

Table 3. Properties of Pittsburgh #8 coal used in this model.

PROXANAL				ULTANAL						SULFANAL		
Most	FC	VM	Ash	C	H	N	Cl	O	S	Pyritic	Sulfate	Organic
Before Drying												
2.52	53.34	36.01	10.65	72.85	5.47	2.92	0.10	5.57	2.44	1.50	0	0.94
After Drying												
1	53.34	36.01	10.65	72.85	5.47	2.92	0.10	5.57	2.44	1.50	0	0.94

Aspen Plus V11 can determine which specific materials are a moisture component of the solid material. H_2O is set as the moisture component. The "dryer" unit can control moisture in PROXANAL based on the air condition injected or a set target. Continuous shortcut type model is selected. The target of the air-dried coal's moisture is specified at 1 wt% of air because some of the inherent moisture can remain on the coal's pores, referred to as residual moisture. The size of pulverized coal is specified as 300 µm. Air with 20% saturated vaper at 25°C is introduced at 600 tonne/day and heated to 300°C, enough for vapor to be evaporated from the coal and not liquefied by the wet-air stream.

3.1.3 Model Results

Figure 3-1 shows the process diagram for coal drying. Drying up 1,000 tonne/day of Pittsburgh #8 coal requires 600 tonne/day of air, accompanied by 1.98 MW of heat flow to increase the temperature to 93°C. Coal composition after the drying process is tabulated in Table 3. High-volatile A bituminous coal does not have as much moisture as other ranks of coal; therefore, coal drying is not an energy-intensive process.

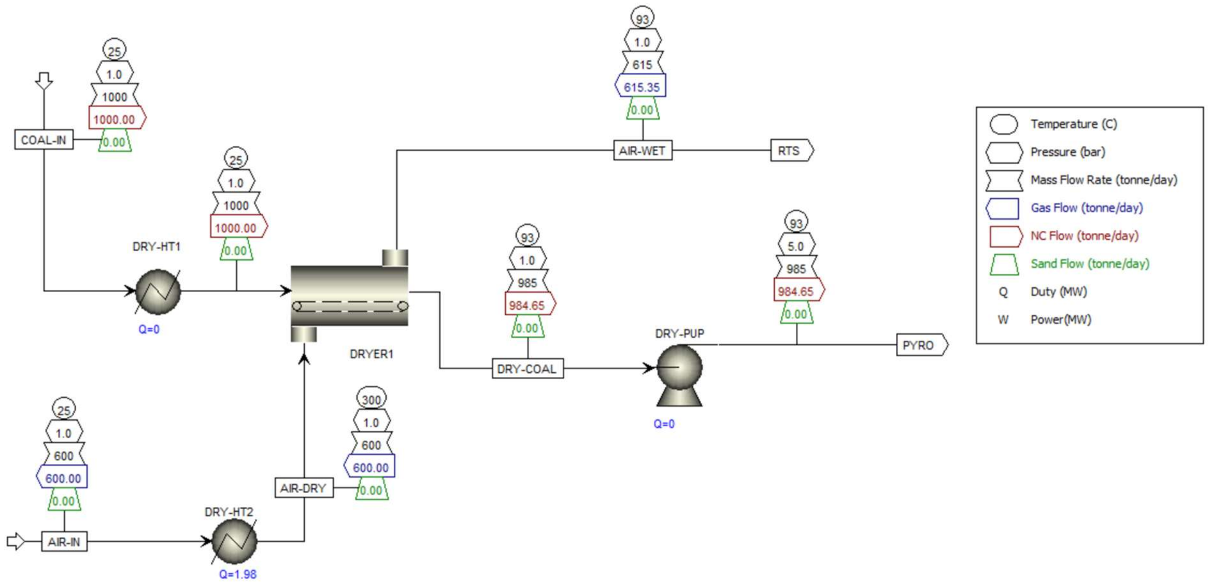

Figure 3-1. Coal drying process and result.

3.2 Pyrolysis and Sand Circulation

Coal pyrolysis converts coal to different products, which can be categorized into three materials based on their phase: solid char, liquid tar and oil, and light gas. The pyrolysis results are dependent on pressure, temperature (final temperature, heating rate, and heating holdup time), coal type, and particle size.

Char is a carbonaceous solid material that remains after the volatile gas, including noncondensable gas and liquid tar and oil, are released through pyrolysis. The atomic composition and chemical structure are changed from coal because gas molecules captured within the coal, functional group, and bridge attached to the coal are driven off during pyrolysis, referred to as devolatilization. The H/C and O/C ratio of char decreases throughout the pyrolysis process, causing char swelling (Fletcher 2013).

Tar and oil are a mixture of a high molecular weight material produced as the bridge between coal clusters is broken during the pyrolysis and thus is easily condensed to liquid as temperatures decrease. Most tar and oil exist in the gas phase when produced due to high temperature. Tar has a ring-like aromatic structure while oil has a chain-like aliphatic structure. Aromatic tar is likely to be formed after bituminous coal pyrolysis rather than aliphatic oil due to the chemical structure of the coal. Benzene, toluene, and naphthalene are common aromatic components of tar.

CO, CO_2, H_2, CH_4, and steam (H_2O) are the common noncondensable gaseous products produced during pyrolysis. Most of H_2O is chemically produced, rather than inherently contained within the coal. Nitrogen- and sulfur-containing gases, though the amount produced during pyrolysis is much smaller than other materials, are not negligible due to their critical environmental effect.

Sulfur compounds reported in gas form after pyrolysis are H_2S, COS, SO_2, COS, etc., and in coal tar, for example, it is thiophane, benzothiophene, and dibenzothiophene (Calkins 1987). H_2S is one of the common products after pyrolysis. The pyrolysis result with Pittsburgh #8 coal produced at the R&F Industries mines (Belmont, Ohio) shows that the yields of H_2S are 0.66%, 1%, 1.1%, 0.9%, and 0.5% at temperatures of 600°C, 700°C, 800°C, 900°C, and 1000°C, respectively. CS_2 starts to come out after 800°C and 0.3% yields at 1000°C (Calkins 1987). The production rate of H_2S is maximized at 434°C and 575°C, shaped as a camel with twin humps, as shown in Figure 3-2 (Oh, Burnham, and Crawford 1988). NH_3 and HCN are the common nitrogen-related material produced during pyrolysis.

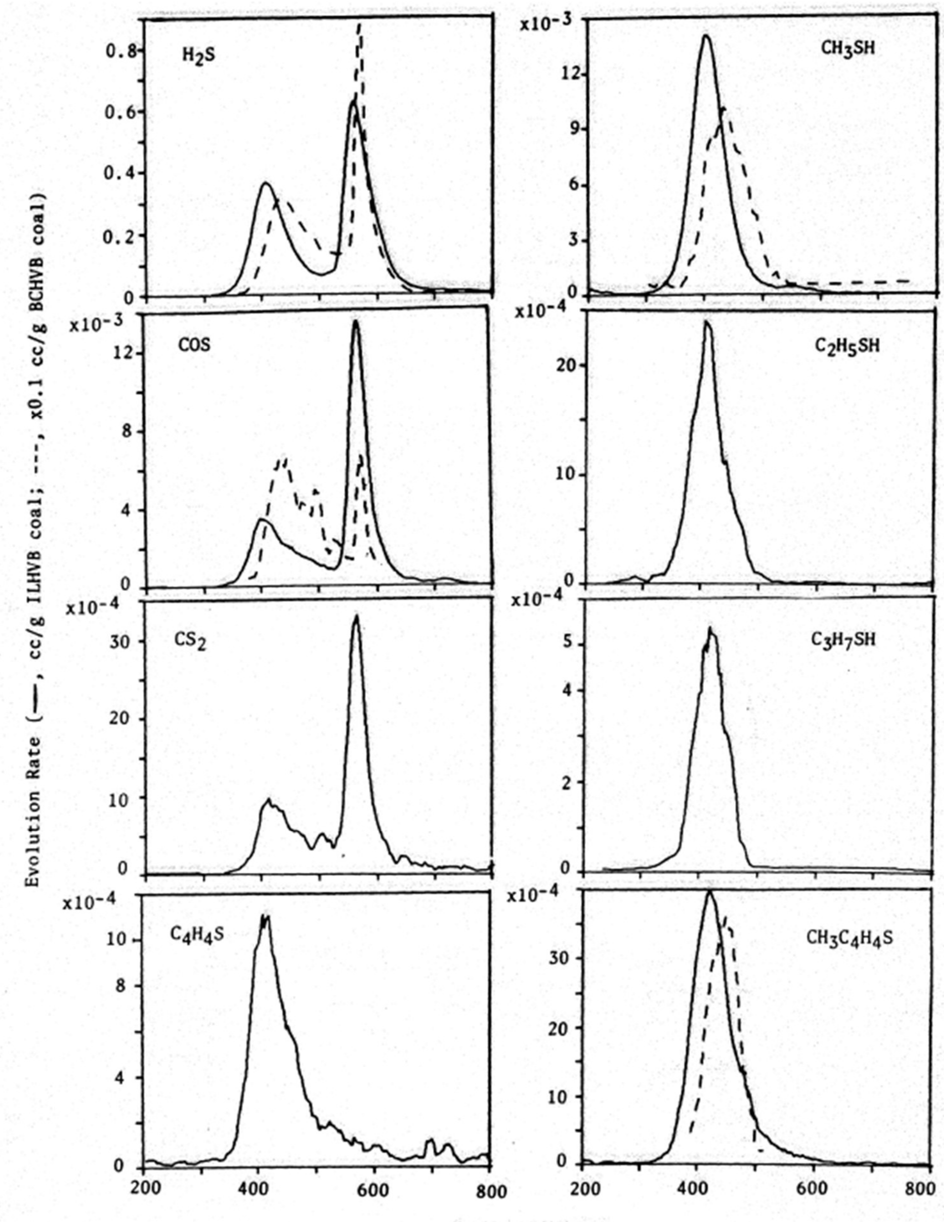

Figure 3-2. Evolution profiles of eight sulfur gases.

Sand needs to be separated from the char after pyrolysis to recycle sand and further process char. Air classifier is a method to separate particles based on separation velocity that is a function of particle density and size, expressed in Equation 7 for sphere particles. Particles with a higher settling velocity are less willing to follow the flow stream. Figure 3-3 shows a schematic drawing air classifier.

$$v_{settling} = \rho_p g d_p^2 / 18\mu \tag{7}$$

where

$v_{settling}$	=	settling velocity
ρ_p	=	density of particles
g	=	gravitational acceleration
d_p	=	particle diameter
μ	=	dynamic viscosity of fluid.

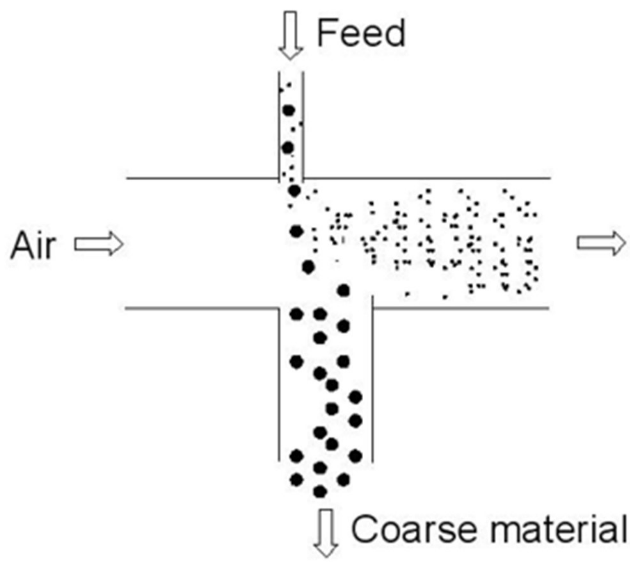

Figure 3-3. Schematic drawing of a crossflow sifter type air classifier, reprinted from an Aspen Plus V11 help document (Aspen Tech 2019).

3.2.1 Model Description

The pyrolysis process is expressed as an RStoic reactor in Aspen Plus, which requires the model to estimate product yields for char, tar, and light gas; the composition of light gas; and component attributes of char. Heat is supplied via hot sand heated by a nuclear-driven heat source. The sand is circulated and separated from char.

3.2.1.1 Chemical Percolation Devolatilization Model and Product Yields Estimation

The chemical percolation devolatilization (CPD) model suggested by Fletcher (1992) can estimate the product yields after pyrolysis. This model explains how in pyrolysis pyrolysis, labile bridges attached to the coal are activated and turned into reactive bridges, followed by the reactions in which reactive bridges ($£^*$) can be converted into either a side bridge (δ) or a char bridge (c) and gas molecule (g). Sidechain (δ) can also be solely detached as a gas molecule (g). Getting the result requires the proximate and ultimate coal properties in a dry ash-free basis, pyrolysis condition (pressure, final temperature, heating rate, and holdup time), coal reaction parameters, and chemical structure information, which can be measured via 13-C nuclear magnetic resonance parameters: the average molecular weight per aromatic cluster (M_{cl}), the average molecular weight per sidechain (M_{δ}), the average number of attachments (side chains and bridges) per cluster, referred to as the coordination number ($\sigma + 1$), and the initial fraction of intact bridges (p_0) and char bridges (c_0). As nuclear magnetic resonance cannot measure c_0 variables, it was estimated by the correlation as a function of ultimate properties.

The latest CPD model written in MABTLAB code, *CPD_Heat_MATLAB* (Fletcher and Pugmire 2020), is employed in this study using Pittsburgh #8, high-volatile bituminous coal. The coal is heated at 1,000 K/sec to a target temperature and held there for 30 seconds. Chemical structure properties used for the CPD simulation for Pittsburgh #8 is written in Table 4, and their CPD simulation results for 500°C and 700°C and 1 and 5 atm are tabulated in Table 5. Figure 3-4 shows product yields of char, tar, and light gas estimated from the CPD model as a function of temperature and pressure. Yields of tar and light gas increase as temperature increases up to 700°C. The labile bridge between coal aromatic clusters is dissociated, and the detached small cluster becomes tar. The unstable functional group attached on the coal cluster is devolatilized, turning into light gas. However, product yields become independent from temperature at 700°C or higher.

Pressure also affects the product yields of tar and light gas. Solid, dashed, dash-dot, and dotted lines in Figure 3-4 represent pressures of 1, 10, 20, and 30 atm, respectively. Product yields of char and light gas increase as pressure increases while tar yields decreases. As pressure changes, product yields of tar are changed dramatically around 500°C. In this system, the CPD model also estimates the product yields of the most common four noncondensable light gases, CO, CO_2, CH_4, and H_2O, shown in Figure 3-5. The most common gaseous yield from coal pyrolysis is steam. Note that the high amount of steam observed after pyrolysis is mostly produced through chemical reactions and not from moisture inherent in the coal.

After the above parameter study, the operation condition of this model's pyrolysis vessel is determined as 500°C and 5 bar. To stick to our goal to avoid high temperatures, 500°C is the minimal temperature that can produce at least 20% of light gas. The amount of tar produced can be controlled by changing the operating pressure.

Other resulting gases might include hydrogen (H_2), aliphatic hydrocarbon (C2H4), hydrogen cyanide (HCN), ammonia (NH3), hydrogen sulfide (H_2S), hydrogen chloride (HCL), and vaporized small size tar. In this simulation, product yields for NH3, HCL, and H_2S are specified as 0.00294, 6.17e-5, and 0.00255, respectively, which is the same as in the report (O'Brien, B. H. 2014) for Wyoming subbituminous B coal at 500°C. Hydrogen gas is reportedly not produced at 500°C. The product yields of other gases subtracted by the amount of minor gases (NH3, HCL, and H_2S) is 0.0423, and it is assumed to be benzene. All the tar is assumed to be benzene in this study, thus CPD estimates the total yield of benzene at 0.2066. The RStoic reactor model is used for the pyrolysis model. Product yields and the stoichiometric coefficient specified for RStoic reactor are tabulated in

Table 6. As the molar mass of the NC solid is defined as 1 g/mol, the stoichiometric coefficient for the products is the inverse of the product material's molecular weight.

Table 4. Chemical structure parameters of Pittsburgh #8 coal used in CPD model.

	p_0 [intact bridge/total bridge]	c_0 [char bridge/total bridge]	σ+1 [the number of attachments /clusters]	M_{cl} [MW/aromatic cluster]	M_δ [MW/side chain]
Value	0.48	0	4.8	323	32

Table 5. Product yields estimated by CPD model in mass basis.

		Yield [wt. product /wt. coal]						
Temp	Press	Char	Tar	H_2O	CO_2	CH_4	CO	Other
500°C	1 atm	0.600211	0.208797	0.040434	0.018174	0.034442	0.052627	0.045315
700°C	1 atm	0.442439	0.303419	0.049944	0.017934	0.053272	0.072707	0.060285
500°C	5 atm	0.633956	0.164313	0.042708	0.019196	0.036378	0.055586	0.047863
700°C	5 atm	0.475193	0.251849	0.053642	0.019261	0.057216	0.078090	0.064749

Table 6. Product yields determined in this model at 500°C and 5 atm.

	Yields at 500°C, 5 atm [wt. product /wt. coal]	Stoichiometric Coefficient [1/molecular weight]
Char	0.633956	1
Benzene (as Tar)	0.164313	0.0128025
H_2O	0.042708	0.0555084
CO	0.055586	0.0357143
CO_2	0.019196	0.0227273
CH_4	0.036378	0.0623441
Benzene (as other gas)	0.0423	0.0128025
NH_3	0.00294	0.0587165
HCL	6.17e-5	0.0247429
H_2S	0.00255	0.0293255

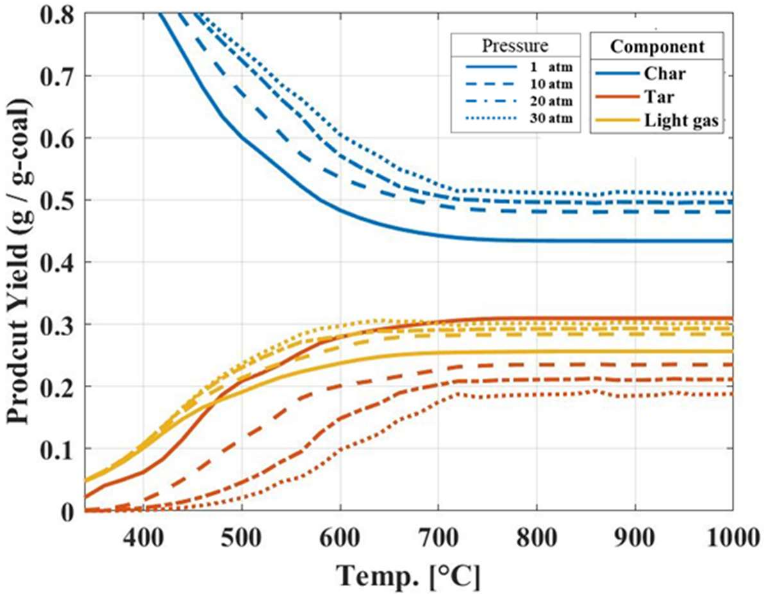

Figure 3-4. Product yields as a function of temperature estimated by CPD model for Pittsburgh #8 coal. Pressures of 1, 10, 20, and 30 atm correspond to solid, dashed, dashed dot, and dotted lines, respectively.

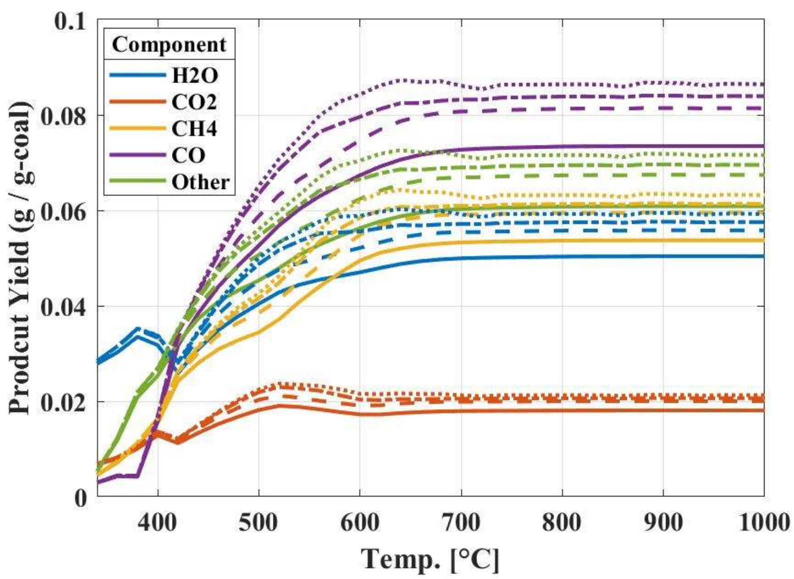

Figure 3-5. Light gas component yields as a function of temperature estimated by CPD model for Pittsburgh #8. Pressures of 1, 10, 20, and 30 atm correspond to solid, dashed, dashed dot, and dotted lines, respectively.

3.2.1.2 Component Attributes of Char

Composition attributes of char change as light gas and tar are released during the devolatilization. Several studies measure the component attributes of char compared to its parent coal, and the ultimate analysis for each is tabulated in Table 7. Char composition is typically higher in carbon and lower in oxygen and hydrogen than its parent coal. The reason for this trend is that H and O atoms easily form light gases while the C atom remains. Fletcher and Hardesty (1992) show that the H/C atom ratio of the char produced is decreased as residence time of the particle during pyrolysis increases. The amount of ash increases as the residence time of the particle increases because ash materials does not escape from the coal in the low temperature of 500°C. Ash does not start to melt down until around 1200°C, Rowan et al. (2014) performed the low-temperature pyrolysis for Eastern bituminous coal (Pittsburgh #8) obtained from Consol Energy's Blacksville, West Virginia, mine. That study measured the char and tar yields and char component attribute produced for two different sizes of pulverized coal. The current study follows the data of the 300–500 µm case from Rowan et al. (2014). It assumed that all chlorine is driven off from the coal, and therefore char does not have a chlorine component, and the sulfur composition of char is the same as coal.

Table 7. Component attribute of Pittsburgh #8 coal and char produced used in this model.

PROXANAL				ULTANAL						SULFANAL		
Most	FC	VM	Ash	C	H	N	Cl	O	S	Pyritic	Sulfate	Organic
Coal Before Pyrolysis												
1	53.34	36.01	10.65	72.85	5.47	2.92	0.10	5.57	2.44	1.50	0	0.94
Value Used in This Model												
0	69.25	14.36	16.39	72.33	3.3	3.15	0	1.516	3.31	2.03		1.28

All values are dry-based, format used in Aspen Plus.

3.2.1.3 Sand Circulation System for Energy Transport

Sand particles deliver the heat required to increase coal's temperature during pyrolysis similar to the method in INL report TEV-2132 (O'Brien 2014). Sand is heated by steam or gas from a nuclear reactor heat source and interacts with dried, pluralized coal within the pyrolysis vessel, increasing the coal's temperature.

The sand recycle flow determined in PNNL-18284 (Jones et al. 2009) and TEV-2132 (O'Brien 2014) was 15 kg sand per kg dry hybrid poplar/coal. Bridgwater mentions that the typical sand-to-feed ratio for pyrolysis is closer to 20:1 (Bridgwater 2012). In this study, however, the sand-to-dry-coal ratio is set to approximately 3:2, since we only considered energy conservation. Limitations of heat transport through conduction, convection, or radiation are not considered. Extra sand might be required if considering the limits of heat transfer between solid-solid, solid-gas, or solid-wall.

After the pyrolysis, it is assumed that most coal is converted into char without a size change and that most ash remains embedded in the char, thus no special separation unit is considered for ash. An ESP might be considered to capture fly ash.

The air classifier is selected for particle separation between char and sand. The Rogers model is selected as a classification function to determine particle separation. Cut size, separation sharpness, and the fraction of fluid in the feed to fines outlet, which are the parameters of the ROGERS model, are specified as 120 µm, 0.94, and 0.7, respectively. Then, coal and char particles with an average diameter of 300 µm move against the flow stream and exit the cycle, whereas sand particles with an average diameter of 75 µm will remain in the cycle. The amount of sand lost during the pyrolysis and screening is supplemented.

The solid material will not be transported through the pipe if the fluid velocity drops below a critical velocity, referred to as saltation velocity. The pipe unit is employed to check the fluid, solid, and saltation velocities. The radius of the pipe is specified as 0.3048 m. The Muschelknautz model is used for dilute phase conveyance during this process.

3.2.2 Model Results

Figure 3-6 shows the flow diagram of the model for the pyrolysis reactor and sand circulation. Dried coal with a diameter of 300 µm, inert CO_2 gas captured from the Rectisol process, heated sand with a diameter of 75 µm, and refluxed light gas are mixed at the mixer (PY-MX1) and introduced to the RStoic reactor (PYRO) as a pyrolysis vessel. Coal conversion in the pyrolysis vessel is calculated based on the CPD model and

Table 6. Coal is converted to char, tar (assumed as benzene), and light gases. A coal feed of 984.65 tonne/day and CO_2 gas of 240 tonne/day as the transport gas are introduced to the pyrolysis cycle and mixed with heated sand of 597 tonne/day. After pyrolysis, char of 624.22 tonne/day, tar (benzene) of 203.44 tonne/day, H_2O of 42.05 tonne/day, CH_4 of 35.83 tonne/day, CO of 54.75 tonne/day, and CO_2 of 258.91 tonne/day exit the cycle at the stream (PYR-CHAR). Small amounts of NH_3, H_2S, and HCl are also produced. Table C-2 in Appendix C shows the mass flow rate for each component, labeled blue for gas and tar, green for sand, and red for NC solid (coal and char).

Fluid velocity is estimated as 18.11 m/s in a pipe with diameter of 2 feet, which is larger than the saltation velocity of 14.66 m/s, meaning there is no issue with particle transportation. The most energy-consuming unit is the heater for sand flow (NUC-HT), which has a heat demand of 10.2 MW. As coal of 984.65 tonne/day is introduced, approximately 0.893 GJ/tonne coal of energy is required for pyrolysis.

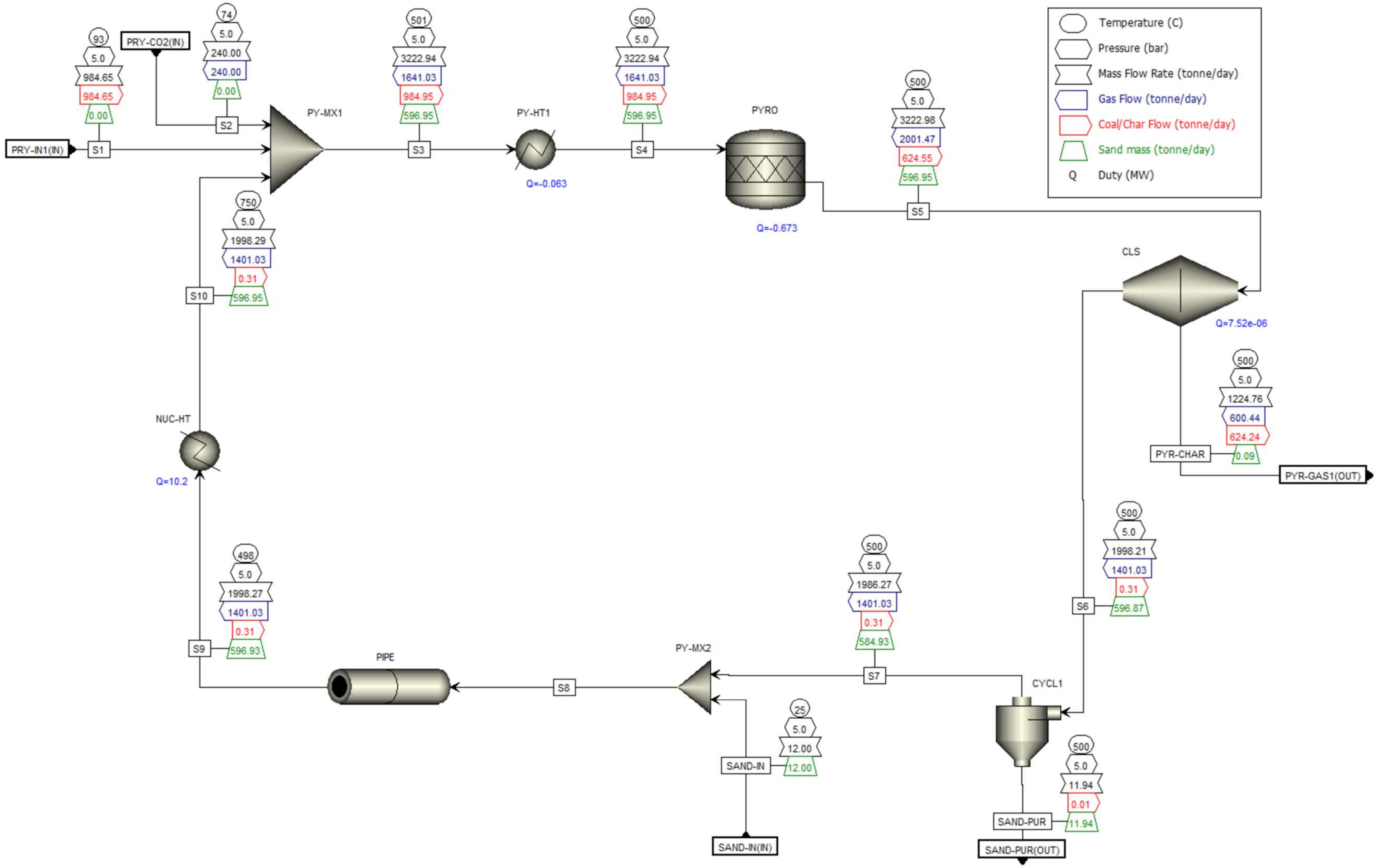

Figure 3-6. Process diagram for pyrolysis and sand circulation.

3.3 Hydrothermal Gasification of Coal Tar and Pyrolysis Gases

Hydrothermal gasification, also referred to as supercritical water (SW) gasification is the process in which raw material reacts within a pressurized high-temperature water solution. In this reaction, water participates as both a solvent and reactant. SW, which has a temperature of 375℃ or higher and a pressure of 22 MPa or higher, is preferred for gasification purposes as it has characteristics not observed in ordinary water. SW conditions are necessary for tar gasification because most organic compounds can become soluble, organic salts that were soluble in the ambient water are no longer soluble and therefore deposited, and a homogenous catalyst can be employed. In this model, hydrothermal gasification is designed to convert tar (assumed as benzene in this study) into light gas. Besides tar, there are many studies that employ hydrothermal gasification for biomass, organic sludge, or low-quality coal. However, this model excluded the hydrothermal gasification of solid char because solid char is used for producing activating carbon. According to Yang et al. (2020), the amount of raw material requires up to 20 wt% of SW input to perform gasification. In this model, the amount of water is determined to match the amount of raw material, lower than 5 wt% of the SW solution. The predictive Soave-Redlich-Kwong model, developed for supercritical flow, is employed as the equation of state.

Figure 3-7 represents the model for the hydrothermal gasification of tar. The left-hand side of the dashed line of the flow diagram is the process to separate tar from the gas and liquid product produced from pyrolysis, and the right-hand side is the hydrothermal gasification process to convert to tar into light gas. As the boiling points of water and tar are lower than light gas, tar and water are easily separated in two series of flash tanks. Separated light gas is directly transported to the autothermal reforming unit (HTG-GAS1) whereas extracted tar passes through the hydrothermal gasification and is then converted to light gas and transported to the autothermal reforming unit (HTG-GAS2). Based on the result of the simulation, 200 tonne/day of tar (benzene) is separated and introduced to the hydrothermal gasification process. The tar accounts for 2.75 wt% of the total solution when water is added at a rate of 7,200 tonne/day. The heat extracted from the gas and liquid product from pyrolysis is used for heating the water, which is used as a solvent for hydrothermal gasification. To make SW, a pump (PP1) pressurizes water to 250 bar, and a heater and heat exchanger increase the reactor operating temperature to 600℃. Salt dissolved in the solution might be deposited as fluid comes to a supercritical flow in the heat exchanger (HX5) where the temperature exceeds the critical temperature, but this phenomenon is not considered in this model.

The RGibbs reactor model is employed for the hydrothermal gasification reactor (RXT1). A heat of reaction of 8.17 MW is supplied to the reactor for the endothermic reaction that occurs during the hydrothermal gasification. As a result of hydrothermal gasification, all tar is converted into 475.7 tonne/day of light gas (H_2, CO, CO_2) and 82.88 tonne/day of CH_4. CH_4 must be removed in further steps. To separate the light gas from SW, the gas is cooled down (HT8) and depressurized (NZ1). Net water consumption during hydrothermal gasification is 314.66 tonne/day.

A high energy input is required in a hydrothermal gasification process because the liquid water must be elevated to supercritical conditions. To match the temperature requirements, heat recuperation through heat exchanger (HX5) of 192 MW, 2 heaters, (HT3) of 26.9 MW and (HT6) of 57.8 MW, and a heat of reaction of 8.17 MW at the reactor (RXT1) and cooler (HT8) of −81.8 MW are required. Therefore, the net cooling requirement for tar separation is −1.82 MW, the net heating requirement for hydrothermal gasification is 11.07 MW, and the work requirement for running the pump is 3.96 MW.

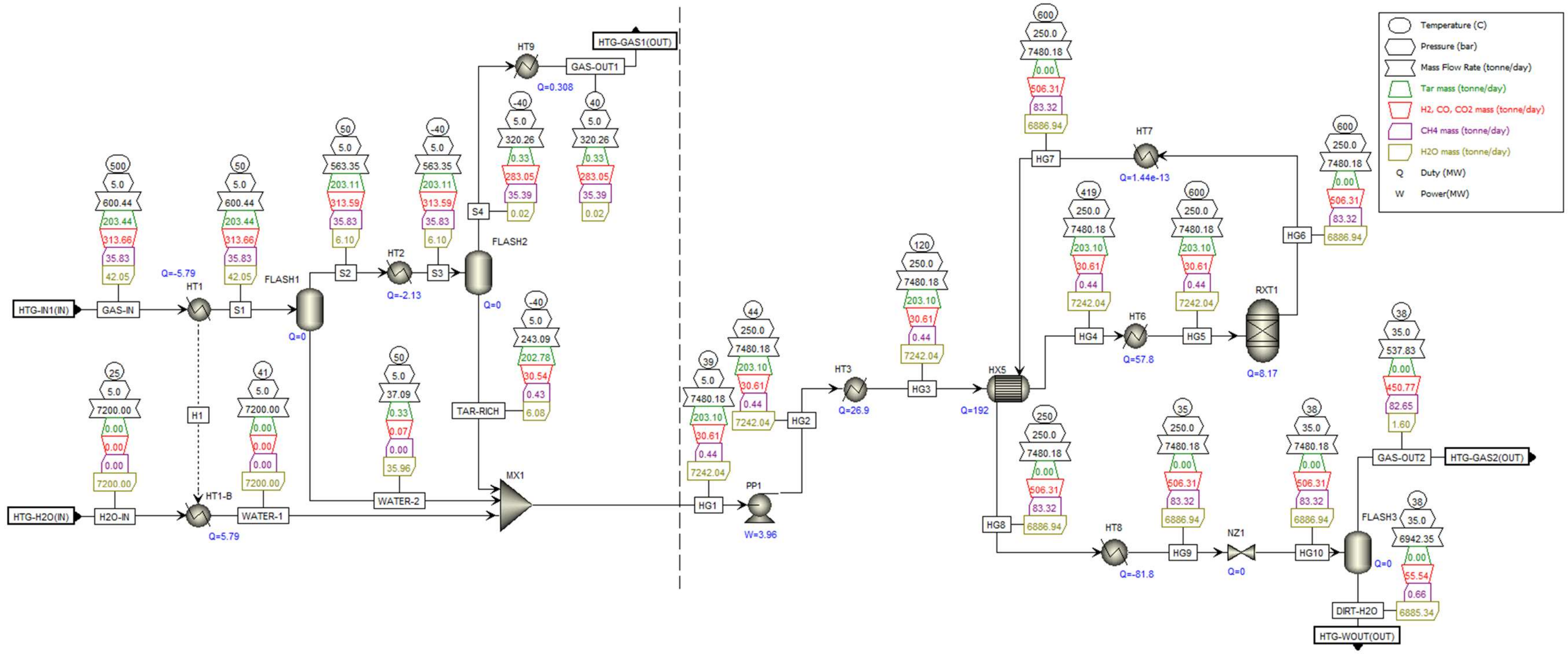

Figure 3-7. Hydrothermal gasification unit.

3.4 Autothermal Reforming

The autothermal reforming process is designed to remove CH_4 produced during pyrolysis and hydrothermal gasification. CH_4 is converted by steam methane reforming, and most of energy required for the SMR is supplied from the heat of combustion of CH_4 with oxygen. Figure 3-8 shows the flow diagram of the autothermal reforming unit. Forming methane as a byproduct is unavoidable due to the low operating temperature of the pyrolysis and hydrothermal gasification unit. Thus, the inlet flow of this unit stream (ATR-IN1) contains approximately 14 wt% methane, as described in Figure 3-8.

Water and oxygen at flow rates of 5,000 kg/h and 5,000 kg/h, respectively, (ATR-AUTO) are heated and mixed with the light gas produced from pyrolysis and hydrothermal gasification (ATR-IN1). Autothermal reforming is performed using the Gibbs reactor (B9), minimizing the heat required for the reactor. Light gas is depressurized to 1 bar (B6) to increase the methane conversion yield in the Gibbs reactor (B9). In the case of Figure 3-8 , 93.7% of methane is converted to light gas by reforming. At the outlet of the reforming process, the pressure is increased to 35 bar by a multistage compressor (B1) and liquid (mostly water) is separated from the light gas at flash drum (B12).

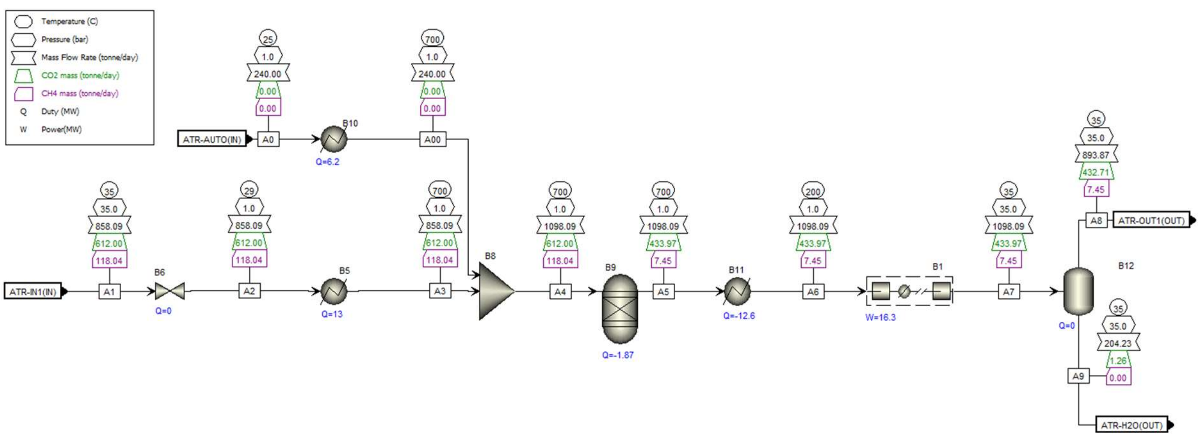

Figure 3-8. Flow diagram of autothermal reforming unit.

3.5 Mercury Removal

The importance of mercury removal is driven by the need to protect the environment, safeguard human health, comply with regulations, support global agreements, respond to public concerns, take advantage of technological advances, and realize economic advantages. Effective mercury removal from flue gas can be achieved through several methods, including adsorption, precipitation, membrane filtration, ESP, and AC injection. The choice depends on factors like the concentration of mercury in the flue gas, the specific composition of the flue gas, and the regulatory requirements in place. Often, a combination of methods may be used to ensure efficient and effective mercury removal from flue gases.

In the context of air pollutant emissions from coal-fired power plants (CFPPs) and the coal pyrolysis process for syngas production, the significance of mercury content in flue gas cannot be understated. Mercury, as an elemental pollutant, has garnered significant attention due to its volatile characteristics and persistent toxic nature. It poses environmental concerns as it can accumulate within the atmosphere, affecting both human health and the environment (Travis and Blaylock 1995; Lindberg and Stratton 1998; He et al. 2021).

Mercury in coal combustion- or pyrolysis-derived flue gas can be present in three forms: elemental mercury (Hg^0), oxidized mercury (Hg^{2+}), and particulate-bound mercury (Hg^p) (Senior et al. 2000). Hg^{2+} is water-soluble and thus can be effectively removed by a wet flue gas desulfurization (WFGD) system. In contrast, Hg^0 is more difficult to remove from flue gas due to its high equilibrium vapor pressure and low solubility in water. For example, a WFGD system can remove 90% of the oxidized mercury but not any Hg^0 (Sinha and Walker Jr. 1972; Zhuang et al. 2004).

In coal combustion and the pyrolysis process, coal particles first begin their pyrolysis and ignition. With the volatile compounds releasing, the char starts to burn and break into smaller particles (Zhao et al. 2017a). At the high combustion flame temperature, almost all the mercury contained in coal decomposes into Hg^0 based on the mercury forms mentioned above in coal. As the flue gas cools down, Hg^0 can react with flue gas components, such as halogens (Cl_2, Br_2), acid gas (HCl, HBr, NO_2), and O_2, to transform into Hg^{2+} through homogeneous reactions (Hall et al. 1991; Pavlish et al. 2003; Niksa et al. 2009). Also, part of the Hg^0 will be catalytically oxidized to Hg^{2+} or absorbed onto fly ash acting as Hg^p through heterogeneous oxidation (Galbreath and Zygarlicke 2000; Norton et al. 2003; Yang et al. 2017). Additionally, some Hg^{2+} can be adsorbed on the fly ash surface as Hg^p while some Hg^0 keeps its form without transformation in the cooling process. Hence, the general mercury transformation process previously described is shown in Figure 3-9. A more detailed description of this process fundamentals, reactions and kinetics is in Appendix B-3.

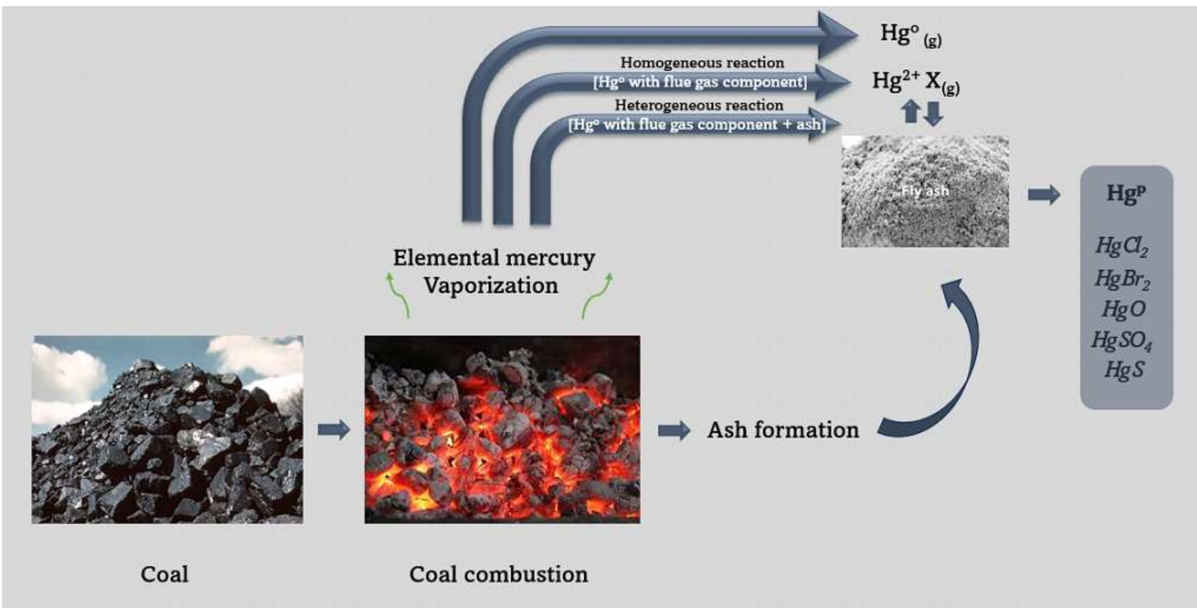

Figure 3-9. General mercury transformation process during coal combustion and pyrolysis.

Thus, understanding the transformation mechanism of mercury in coal combustion or pyrolysis is very important for the selection or development of its removal method. Many factors can influence mercury transformation, such as coal types, flue gas components, flue gas temperature, combustion atmosphere, and coal ash properties.

With more stringent emission limits on air pollutants from coal combustion, the use of air pollution control devices (APCDs) for removing NOx, particulate matter, SO_2, and fine PM has increased in CFPPs and coal pyrolysis. There are many APCD technologies, including SCR, ESP, fabric filter (FF), WFGD, and wet electrostatic precipitator (WESP) (Hu and Cheng 2016). In situ test data and statistical analysis have supported the co-beneficial control of mercury in SCR, ESP, and WFGD configurations. Here, elemental mercury (Hg^0) can be effectively oxidized by SCR catalysts to improve mercury capture. Particulate mercury (Hg^p) is effectively collected on ESPs, and the water-soluble oxidized mercury (Hg^{2+}) can be retained in WFGD scrubbers. These ultra-low emission technologies improve mercury removal efficiency around 88–89.6% and are becoming the most efficient and economical way to reduce mercury emission effects of ultra-low-emission retrofitting on mercury (Zhao et al. 2017b; Liu et al. 2020; Li et al. 2022).

3.5.1 Model Description

Based on whether fly ash participates or not, the mercury reaction can be divided into homogeneous (without fly ash) and heterogeneous (with fly ash) reactions, where both types of reactions are considered for process modeling. However, the formation of halogenated compounds reacting with elemental mercury was not considered due to the lack of halogen ions composition or inductive coupled plasma results of the specific type of coal used for this work. Therefore, results presented in this block are based on the overall generation of Hg^p and Hg^{2+} upstream in the process, calculated from the composition of combined flue gases from the pyrolysis and hydrothermal gasification processes. This stream is known as S21 in the integrated system model (see Figure 3-10), and the composition of this stream is presented in Table 8.

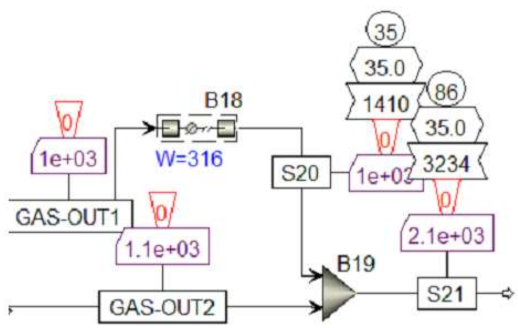

Figure 3-10. Feed stream (S21) to the mercury removal block, combination of flue gases coming out of coal pyrolysis and hydrothermal gasification blocks.

Table 8. Feed stream (FLUEGAS) molar composition.

	Mole Flows (kmol/hr)	Mole Fractions
N_2	0.090953711	0.000787603
SAND	0	0
H_2O	3.318814714	0.028738874
CO	9.168136363	0.079390365
CO_2	48.08589672	0.416393991
H_2	6.274526581	0.054333502
CH_4	47.70834519	0.413124629
H_2S	0.289101155	0.002503436
C_2H_4	2.77E-05	2.39E-07
NH_3	0.521966265	0.004519904
HCL	0.006802347	5.89E-05
BENZENE	0.017145907	0.000148473
FURFURAL	0	0
1-METHYL	0	0
O_2	0	0

	Mole Flows (kmol/hr)	Mole Fractions
MEOH	9.21E-06	7.98E-08
$C_{19}H_{36}O_2$	0	0
C	0	0
S	0	0
Total	115.4817258	1

Aspen Plus software is used to simulate the mercury removal process. In this model, the SCR, ESP, and WFGD units are built using previous core studies and investigations as reference points and are modeled using REquil (Rplug), ESP, and RadFrac models, respectively (Xiong et al. 2011; Hanak et al. 2015; Wu et al. 2023). The mercury transformations are developed based on the model proposed by Senior et al. (2000) for this model. The NO reduction is not considered due to its absence in the process feed stream, see Table 8.

The SCR unit improves elemental mercury oxidation. The mercury oxidation reaction is presented in Table 9. In this process, the fraction of Hg^0 oxidized to $HgCl_2$ in the SCR unit is calculated by a kinetic model. Theoretically, the fundamentals of this process are believed to be driven by the Langmuir-Hinshelwood and Eley-Rideal mechanisms, which have been considered in this model to reveal the elemental mercury oxidation reaction mechanisms over SCR catalysts.

In the Langmuir-Hinshelwood mechanism, HCl adsorbs on the catalyst active sites (WO_3) and reacts with gaseous elemental mercury. An Eley-Rideal/Langmuir-Hinshelwood kinetic model over the commercial $V_2O_5(WO_3)/TiO_2$ SCR catalyst is embedded into the RPlug block to effectively predict Hg^0 oxidation rates. The kinetic model is shown in Equation 8:

$$-r_{NO} = -K_{Hg^0} \frac{C_{Hg^0}\ K_{HCl}\, C_{HCl}}{1 + K_{HCl}\, C_{HCl} + K_{NH_3}\, C_{NH_3}} \qquad \text{Equation 8}$$

where k_{Hg0} is the rate constants of Hg^0 oxidation, which is 3.57×10^9 mol/s m^{-3} (Wu et al. 2023), K_{NH3} and K_{HCl} are the equilibrium constants for NH_3 and HCl adsorption, 5.10×10^5 and 9.42×10^2 m^3 mol^{-1}, respectively (Wu et al. 2023), and C_{NO}, C_{NH3}, C_{Hg0}, and C_{HCl} are the concentrations of NH_3, Hg^0, and HCl in the inlet stream, respectively.

Table 9. Specification of reaction in SCR and WFGD.

Unit	Stoichiometry	Type of Reaction
SCR	$2Hg + 4HCl + O_2 \leftrightarrow 2HgCl_2$	Kinetic
WFGD	$Hg^{2+} + Hg^0 \leftrightarrow {Hg_2}^{2+}$	Equilibrium
WFGD	${Hg_2}^{2+} + 2OH^- \leftrightarrow H_2O + HgO + Hg^0$	Equilibrium

Downstream in the process, once Hg^{2+} and Hg^p are formed, these solid particles are separated from the flue gas (after oxidation in the SCR unit) using the ESP block. The ESP is assumed to have a collection efficiency of 99%, based on plant operation data. The Hg^p collection was split into two ESP units to accommodate the volume of stream flow (Wu et al. 2023).

The WFGD unit can eliminate SO_2 and absorb Hg^{2+} into the limestone-water scrubber solution. The absorption process takes place in the RadFrac block. The electrolytic reactions in the scrubber are also described in Table 9, and the fraction of Hg^{2+} absorbed in WFGD reveals a complete removal of it, taking this portion over the wastewater stream. A process diagram for the entire flue gas treatment process is shown in Figure 3-11, and mercury transformations and distributions over the removal process are depicted in Figure 3-12.

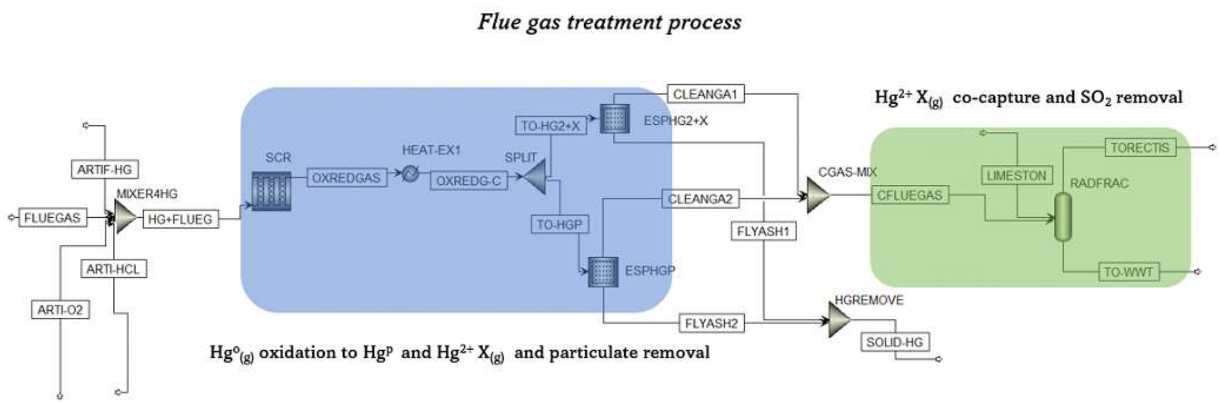

Figure 3-11. Flue gas treatment block for mercury removal.

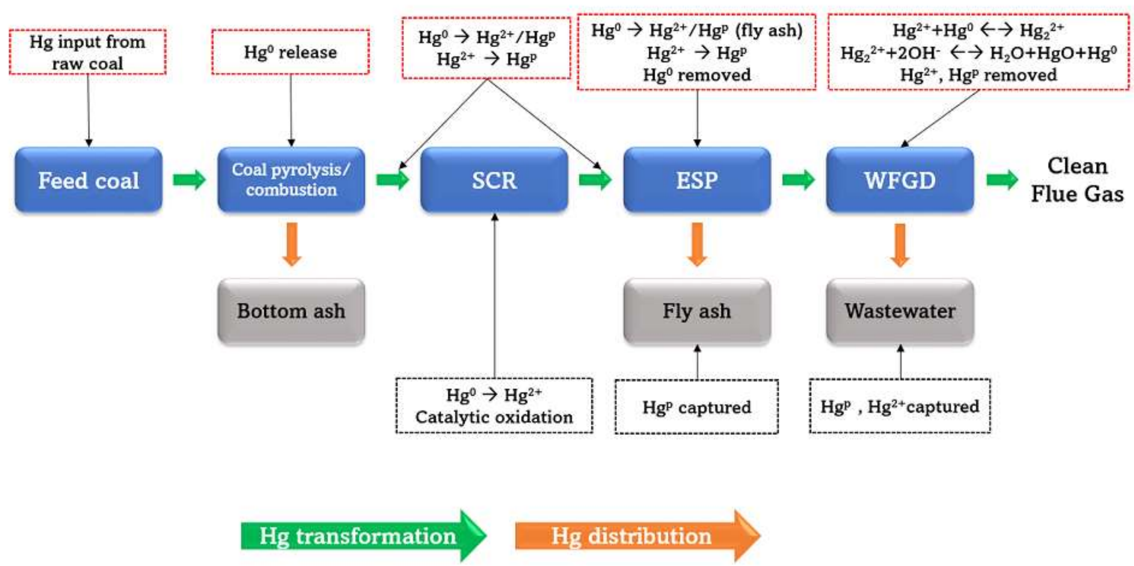

Figure 3-12. Transformation and distribution of mercury along the SCR, ESP, and WFGD configurations.

3.5.2 Model Validation

For the proposed APCDs, a worldwide field data set of mercury co-removal across 45 APCDs installed in various CFPPs using different coal types was collected from Zhao et al.'s review (2019) and presented in Table 10. To assess the efficiency of the mercury removal configuration used in this work with some other similar studies done in the past, we made a quantitative comparison with them to validate the model. As shown in Table 10, similar APCDs can achieve overall mercury removal rates ranged from 43.8% to 94.9% with SRC, ESP, and WFGD configurations using bituminous coals. In the model case scenario, about 99.99% of mercury was removed, improving the maximum removal rate achieved in the field test data by about5.09%. In addition, for the SCR modeling using the Langmuir-Hinshelwood, the Eley-Rideal mechanisms, and the kinetic equilibrium constant gathered in the literature, this catalytic reactor was able to oxidize all mercury (100 wt%) contained in the flue gas. The ESP block was set to be able to remove 99.8% of the oxidized mercury as mercury chloride, and the WFGD unit removed the unreacted mercury (elemental Hg) in the scrubber. The main differences observed between the modeled and real case ESP and WFGD blocks are related to the high ESP costs and amount of energy spent in ESP (particle charge) in industry. In real operation, it is better to save expenditures in energy and further carry out the physical separation of the solids collected in the scrubber by filtration.

Table 10. Mercury removal model versus similar configuration and coal comparison.

Boiler Type & Capacity (MW)	APCDs	Hg^0 Oxi. Rate by SCR (%)	Mercury Removal Rate (%)				Countries
			ESP (or ESP+FF)	WFGD	WESP	APCDs (Hg^t)	
300–500 µm	SCR+ESP+WFGD	100	99.8	0.19	Not used	99.99	Base case model
PC-500,600	SCR+ESP+WFGD	6.5–73.8	28.3–64.7 (ESP)	7.9–42.3 (Hgt)	—	43.8–71.4	South Korea
PC-190	SCR+ESP+WFGD	71	—	89.5-98.0(Hg2+) 54.9- 90.2 (Hg0)	—	—	Not specified
PC-800	SCR+ESP+WFGD	45.4	68.5–77 (ESP)	45.4–55.5 (Hg0)	—	87–89.5	South Korea
PC	SCR+ESP+WFGD	—	—	—	—	69	South Korea
PC-200	SCR+ESP+WFGD	—	—	—	—	87.6	China
PC-500, 600	SCR+ESP+WFGD	7.3–79.9	71.3–90.4 (ESP)	26.3–66.2 (Hg0)	—	89.5–94.9	South Korea

3.5.3 Model Results

For the proposed flue gas treatment focused on the mercury removal model, some necessary assumptions were made to closely match the real composition of industrial flue gas contaminated with elemental mercury after coal pyrolysis and combustion. Initially, the mercury content in this block was artificially added (ARTIF-HG) based on typical mercury concentrations (Tewalt et al. 2010; Wang et al. 2010). The range of typical mercury concentrations is 1.92–27.15 µg/m^3, with over 18 µg/m^3 considered high toxic levels. This work used a reference mercury concentration of 27 µg/m^3 in the resulting flue gas (HG+FLUEGAS) to verify and validate the model. As seen in Table 8, the initial concentration of hydrogen chloride (HCL) coming upstream in the process (FLUEGAS) was too low to reach model convergence. Therefore, artificial HCL (ARTI-HCL) and oxygen (ARTI-O2) were added due to the inexistence of the latter in the initial feed stream molar composition. These additional amounts were estimated through model iterations to achieve a total oxidation of the molar concentration of mercury in HG+FLUEGAS carried out in the catalytic SCR reactor block. There are no sulfur oxides (SOx) considered upstream in the process (FLUEGAS). Thus, there is no sulfur dioxide in the feed stream of this simulation block. The absence of sulfur dioxide reduces the reactions with limestone in WFGD such that only H^{2+} capture takes place due to its high-water solubility (TORECTIS). An initial flue-gas-to-water ratio of 5.5 was assumed to reach a complete removal of the remaining Hg^{2+} ($HgCl_2$ in TO-WWT), since previous studies have shown the mercury concentration in the WFGD unit decreases with an increased liquid-to-gas ratio in the scrubber unit (Wang et al. 2010). The converged molar and mass streams compositions are shown in Appendix C-6.

A comprehensive study on mercury removal in a coal pyrolysis and combustion plant has been performed, reaching a complete removal of elemental mercury after conversion and migration to solid or liquid phases. The results include detailed results for mercury distribution, removal, and emission behavior across the SCR, ESP, and WFGD configuration, demonstrating the feasibility and high performance of this technology toward flue gas decontamination. This shows the ability to catalytically oxidize mercury in SCR units, where about half of the mercury is retained in the fly ash and removed as solid particulate and the remaining mercury in the gas phase is adsorbed in the liquid outlet of the WFGD unit block. The influence of flue gas components and the wide reaction temperature range of mercury oxidation or adsorption by fly ash is rarely studied systematically, which needs further attention for model improvements.

3.6 Rectisol Process

The Rectisol process is the most widely used physical solvent gas treating process for acid gas removal using an organic solvent at low temperatures. In general, methanol is used for removing hydrogen sulfide, carbonyl sulfide, and carbon dioxide as well as organic and inorganic impurities (Sun and Smith 2013; Gatti et al. 2014).

Raw syngas is produced through pyrolysis and gasification to produce a gas consisting primarily of H_2, CO, water, and CO_2 with small amounts of H_2S and CH_4. Impurities are removed through the Rectisol process to meet the gas composition required for methanol production.

3.6.1 Model Description, Validation, and Results

The Rectisol model developed here is based on Linde's patent proposed by Ranke et al. (1982) and a review paper written by Gatti et al. (2014). The model was able to reproduce the result of Gatti's reference model and modify it for the current study. The Perturbed Chain Statistical Associating Fluid Theory model is used as the equation of state. It is usually used for carbon capture and storage, therefore some of parameters used in the model are modified based on Gatti at al. (2014). Figure 3-13 represents the flow diagram of the Rectisol model that this report used and the result. The green and red-colored boxes show the amount of CO_2 and H_2S in each stream.

Four methanol scrubbing towers are installed in the model. Methanol solvents or a methanol-dominant solution are introduced at the top of Tower 1, 2 and 3, dissolving CO_2 and H_2S materials as they fall down each stage of the tower. A specification of each tower is in Table 11. The first stage represents the top stage of the scrubbing tower, including the condenser stage. The first stripping tower (TW1) is designed to dissolve CO_2 and H_2S in the methanol solvent and separate light syngas from the mixture. This design consists of two different parts. Stages 1–8 are designed to dissolve CO_2, whereas Stages 8–18 are designed to dissolve H_2S. An internal cooler of −33°C is installed between Stages 4 and 5. Light syngas that does not dissolve in methanol exits from the top of the tower and is used for methanol synthesis. The CO_2-dominant methanol solvent is extracted at Stage 8 of the tower and is introduced at the top of Tower 2, whereas the H_2S-dominant methanol solvent is collected at the bottom of the tower and is introduced at the middle of Tower 2. Table 11 represents the temperature and mole fraction of the CO_2 profile and the H_2S profile in the liquid phase as a function of the stages. The first stage is the top of the tower where the methanol solvent is introduced. It shows the temperature ranges from −46°C to −10°C within Tower 1. The mole fraction of CO_2 in the liquid phase increases from Stage 1 to 8 and does not change much after Stage 8, thus it is extracted at this point. The side draw amount of CO_2-dominant methanol solvent is determined as 0.412 to fulfill the H_2S mole purity of 0.0001 at the top exit of the tower. The maximum mole fraction of H_2S in its liquid phase is observed at the bottom of the tower. Towers 2 and 3 are designed to separate CO_2 from the methanol solvent. Most of the methanol is separated at the top of Tower 2. Tower 3 is designed to maximize CO_2 recovery. This distillation tower uses the reboiler, and its reflux ratio is specified as 10. A design specification analysis has not been performed for Tower 3. It might be needed later to improve the carbon capture and storage performance. Tower 4 is a distillation tower with a reboiler and partial condenser that recuperate the methanol used as a solvent in the system. The collected mixture of CO_2 and H_2S at the top of Tower 4 is sent to the Claus process to separate H_2S from the CO_2. The design specification is set as a H_2S mole purity of 1e-7 at the methanol reflux outlet and methanol mole purity of 0.001 at the H_2S dominant outlet. To match the design specification, the reflux ratio was specified as a mass of 0.00127 and distillate-to-feed ratio of 0.076526. Table 12 shows the result of the Rectisol process to capture the CO_2 and H_2S. CO_2 recovery can be obtained up to 97.7% in total through the process. Light gas only contains 2% of CO_2 at its original source and seldom contains H_2S. H_2S purity at CO_2-OUT1 and CO_2-OUT2 can be limited to below 200 ppm. Table 13 represents the comparison of CO_2 and H_2S recovery in the Rectisol process with other simulation result from Gatti et al. (2014), showing similar results.

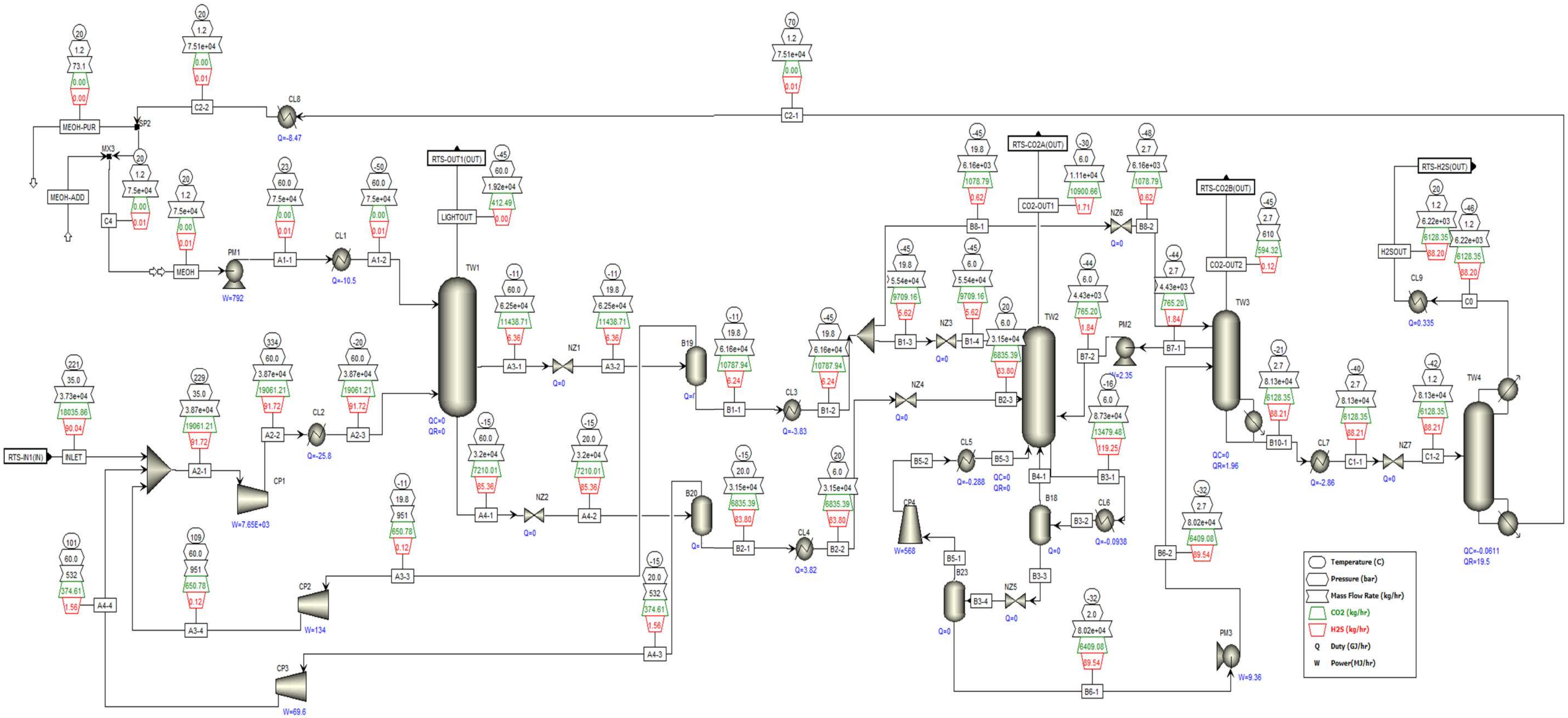

Figure 3-13. Flow diagram of Rectisol process.

Table 11. Specification of scrubbing towers used in Rectisol process.

	TW1	TW2	TW3	TW4
Model Type	RadFrac	RadFrac	RadFrac	RadFrac
Stages	18	20	16	10
Boiler/condenser	None/none	None/none	None/kettle	Partial vapor /kettle
Pressure [bar]	60	6	2.7	1.2
Feed stream	A1-2: 1 (above) A2-3: 18 (on)	B2-3: 12 (on) B4-1: 20 (on) B1-4: 1 (above) B5-3: 20 (on) B7-2: 19 (on)	B8-2: 1 (above) B6-2: 6 (on)	C1-2: 5 (on)
Product stream	LightOUT: 1 (*v*) A3-1: 8 (*l*, 0.4128 mass fraction) A4-1: 18 (*l*)	CO_2-OUT1: 1 (*v*) B3-1: 20 (*l*)	CO_2-OUT2: 1 (*v*) B7-1: 5 (*l*, 0.05 mass fraction) B10-1: 16 (*l*)	C0: 1 (*v*) C2-1: 10 (*l*)
Internal stream	Pump-arounds at Stage 4→5 with a cooler of −33°C	—	—	—
Design specification	H_2S mole purity of 0.0001 at the top outlet	—	—	H_2S mole purity of 1e-7 at the methanol reflux flow Methanol mole purity of 0.001 at the H_2S dominant outlet
Operating specification	Side-draw-to-feed ratio: 0.412809	—	Reflux ratio in mass: 10	Reflux ratio in mass: 0.00127232 Distillate-to-feed ratio: 0.076526

Table 12. Inlet and outlet composition of CO_2 and H_2S after Rectisol process.

		INLET	LIGHT-OUT	CO_2-OUT1	CO_2-OUT2	H2S-OUT
CO_2 mass flow rate	kg/h	18,036	412.5	10,900	594	6128
H_2S mass flow rate	kg/h	90.04	0	1.71	0.12	88.2
CO_2 mass fraction	%	0.484	2.1	97.9	97.4	98.5
H_2S mass fraction	ppm	2,417	0	154	193	14,178

Table 13. Percentage of the recovery in Rectisol process model

Component	User case model [wt% recovered to the feed]	Result from Gatti et al. (2014) [wt% recovered to the feed]
CO_2	97.7	97.6
H_2S	98.0	99.0

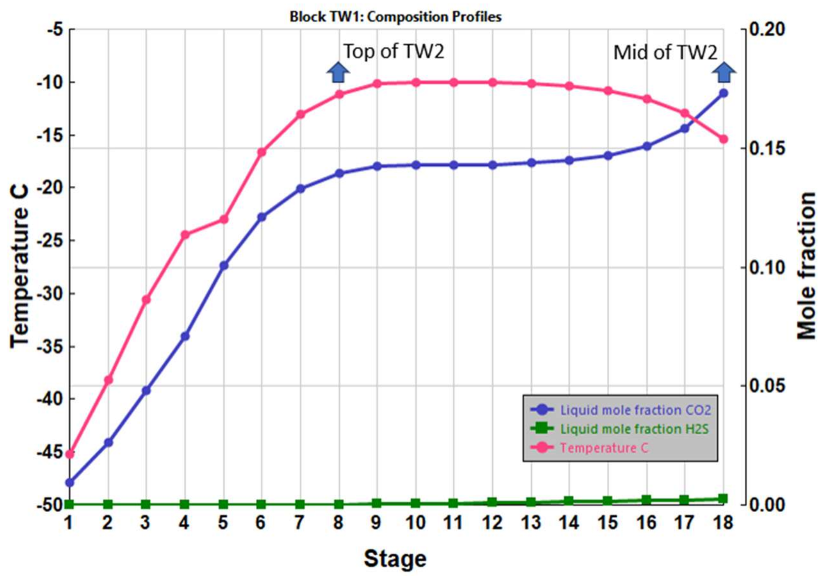

Figure 3-14. Temperature and mole fraction of CO_2 and H_2S in liquid phase at each stage of Tower 1.

3.7 Claus Process

The Claus process is a well-established chemical process used for removing hydrogen sulfide (H_2S) and sulfur-containing compounds from natural gas, refinery gas, and other industrial gas streams. Hydrogen sulfide is a highly toxic and corrosive gas often found in natural gas and crude oil. It poses health and safety risks to humans, as well as environmental concerns when released into the atmosphere. Therefore, its removal is essential in various industrial processes. The primary purpose of the Claus process is to recover sulfur from H_2S-containing gas streams. The recovered sulfur can be used in various industrial applications, such as the production of sulfuric acid, fertilizers, and other chemicals. The Claus process is highly efficient and can recover up to 98% of the sulfur from H_2S-containing gas streams (Clark et al. 2015). This high sulfur recovery efficiency has made it an environmentally friendly option, as it reduces sulfur emissions, which can lead to acid rain and other environmental issues. In summary, the Claus process is a critical and efficient method for removing hydrogen sulfide and recovering sulfur from industrial gas streams, playing a significant role in ensuring both safety and environmental compliance in various industrial sectors.

3.7.1 Model Description

The split-flow-type variant of the Claus process is under consideration for this research. This process involves a furnace reactor and two consecutive adiabatic reactors. The feed is bifurcated into two streams. The first stream is mixed with air and introduced into the furnace. Simultaneously, the second stream is injected into the middle section of the furnace.

Within the furnace, a portion of the hydrogen sulfide converts into sulfur and sulfur dioxide. To prevent sulfur condensation within the pipelines and facilitate heat recovery from the furnace effluent, the effluent stream from the furnace is cooled in a boiler. This cooling process allows for the condensation and separation of elemental sulfur from the furnace effluent. Additionally, because hydrogen sulfide conversion involves a significant number of radical reactions, it is imperative to maintain the reactive conditions in a controlled manner to prevent recombination reactions.

Typically, 60–70% of the total elemental sulfur production occurs within the thermal section. Subsequently, the stream is heated and directed to the first catalytic reactor. The effluent from the first reactor is cooled in the boiler to facilitate the separation of elemental sulfur. Afterward, it is reheated and sent to the second reactor. Generally, the catalytic sulfur recovery process encompasses three distinct stages, including heating, catalytic reaction, and subsequent cooling and condensation.

The output from the second reactor is routed to the boiler to separate elemental sulfur, while the uncondensed portion is directed to the separation section.

The Claus process typically involves multiple stages or reactor beds to facilitate the two chemical reactions. The number of reactor beds may vary depending on the specific feed gas composition and the desired sulfur recovery efficiency.

This process operates based on the following chemical reactions:

- Partial Oxidation: H_2S is partially oxidized to sulfur dioxide (SO_2) in the presence of air or oxygen.
- Sulfur Formation: The produced SO_2 is then reacted with additional H_2S to form elemental sulfur (S_8).
- Tail Gas Treatment: Any unreacted H_2S and SO_2, known as "tail gas," is typically treated further to recover additional sulfur or converted to less harmful compounds like sulfuric acid.

In this model, Aspen seems to be lacking some thermodynamic properties for S2 and S8 related to vapor pressure that are necessary to perform a flash calculation. For this reason, Blocks "PH-1," "PH-2," and "PH-3" are used to convert all these compounds to S prior to the flash blocks. Note that there is some enthalpy change associated with this simplification, which is neglected in this simulation. This assumption was based on a previous INL model presented in the reports TEV-667 (Idaho National Laboratory 2010), TEV-672, and TEV-139. The general process flow is presented in Figure 3-15.

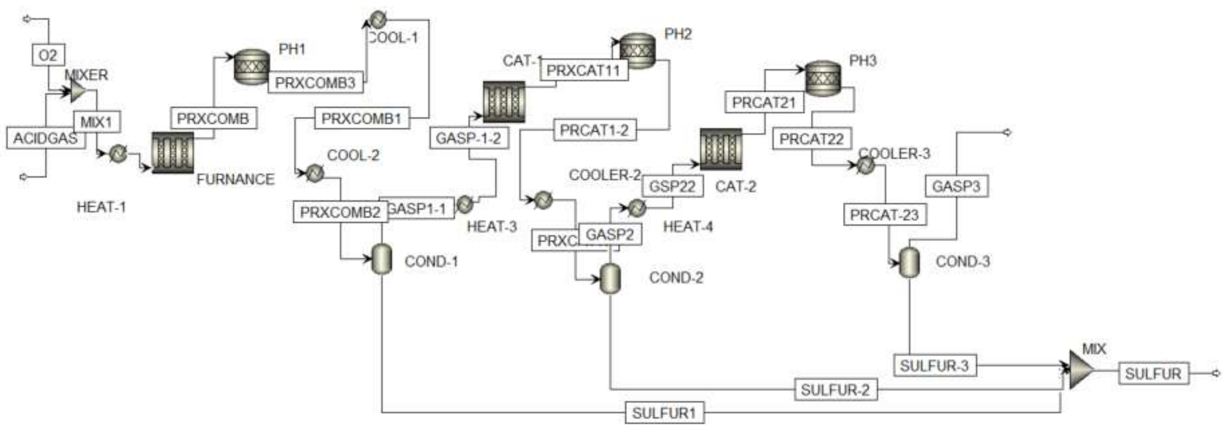

Figure 3-15. Claus process diagram.

3.7.2 Model Results

Enhancing sulfur recovery to approximately 98.5% requires operational modifications. Additionally, to adhere to flare specifications, it is imperative to ensure that the concentration of sulfur-containing compounds in the tail gas remains in a specific concentration. These enhancements, specifically the improvement in the sulfur recovery percentage, can be implemented without any alterations to the equipment. This can be achieved by introducing an adjustment block to regulate the converter temperature and incorporating an air demand analyzer to fine-tune the air-to-fuel ratio.

Figure illustrates the relationship between H_2S/SO_2 ratios (expressed as air demand percentages) and their impact on sulfur recovery. According to the Claus reaction, when the H2S/SO2 ratio closely approximates two, it results in improved performance and greater sulfur recovery efficiency within the catalytic section. Notably, at a minimal air demand of zero percent (indicating a H_2S-to-CO_2 ratio of 2:1), the cumulative percent recovery of sulfur reaches its peak.

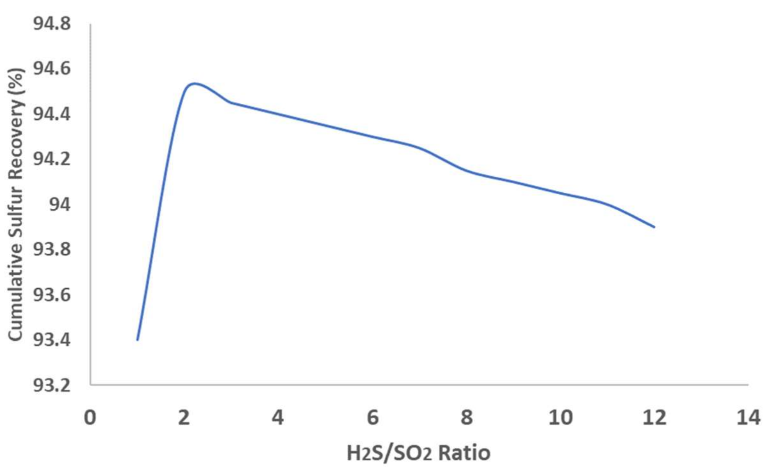

Figure 3-16. Variation of cumulative sulfur recovery percent with H_2S/SO_2 ratio.

Achieving optimal performance for the entire Claus process hinges on understanding the percent conversion and percent recovery of sulfur at each stage of the process. To gauge these effects, the variations in percent sulfur conversion at each unit operation and the cumulative percent sulfur recovery at each unit operation are depicted in Figure 3-17. According to this, major conversion occurs in the second catalytic reaction.

During the combustion of acid gas in the reaction furnace, undesirable byproducts like COS and CS_2 are formed because of secondary reactions involving CO_2, hydrocarbons, and H_2S. These sulfur compounds have an adverse effect on the overall sulfur recovery percentage and need to be minimized. To address this issue, COS and CS_2 are reduced through hydrolysis reactions, primarily occurring at the initial catalytic converter. Hydrolysis involves the interaction between COS and H_2O or CS_2 and H_2O, effectively converting these compounds back into H_2S. This H_2S can then participate in the Claus reaction, which is the desired primary reaction within the sulfur reactor.

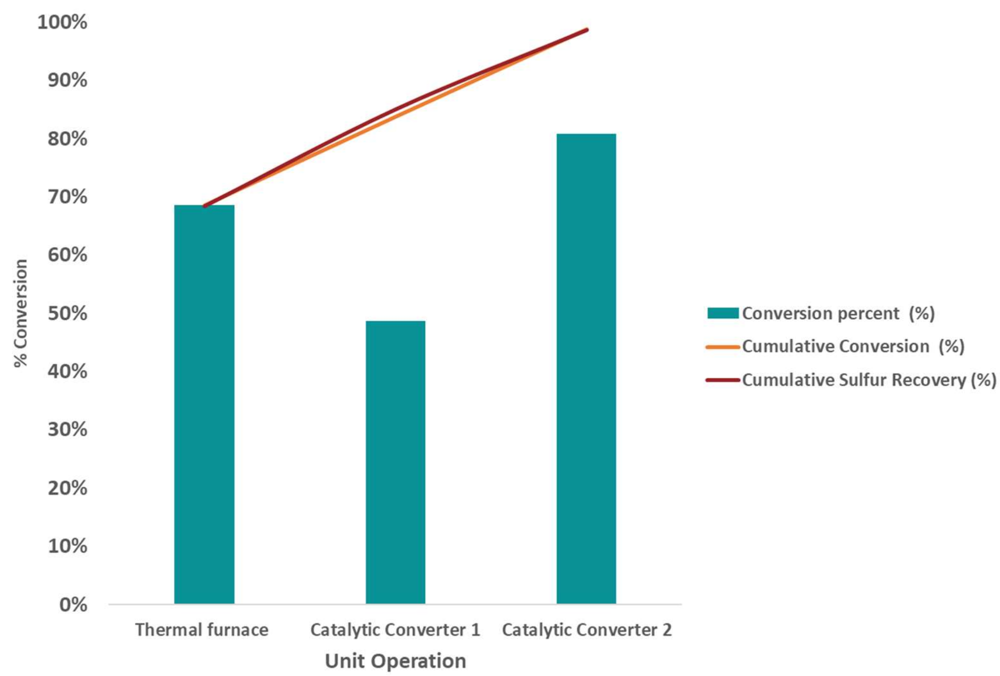

Figure 3-17. Sulfur recovery efficiency summary for base case process.

3.8 Char Conversion to Activated Carbon

The global market for AC has grown steadily and was valued at USD 5.7 billion in 2021 (GACM 2018, ACMT 2021). Demands for AC are projected to reach USD 8.9 billion by 2026 according to a recently published AC market report (GACM 2018). One major driver for this growth is the enormous usage of AC for removing organic and inorganic pollutants for both gaseous stream packed filters and wastewater treatment. To date, AC has been mainly utilized in industrial and municipal wastewater plants, which account for 45% of the AC usage (Zheng et al. 2018). However, in North America, demands for AC are projected to constantly increase due to population growth, additional needs for oil and gas production, and the food and pharmaceutical industries (GACM 2018).

AC is defined as a carbonaceous material (Cuhadaroglu and Uygun 2008) with a high surface area (Ho et al. 2009; Idris et al. 2012), well-developed structural porosity, high adsorptive capacity (Hayashi et al. 2000; Yegaheh et al. 2006; Yacob et al. 2008), and physicochemical stability (Hu and Srinivasan 2001; Zhu et al. 2008). Resources to produce AC can vary widely and include coal-char, lignite, biowaste material, agricultural residues, and forestry biomass. To produce AC from different resources, each resource requires different activation conditions, and the resulting AC has characteristic performances and different cost parameters (Hu and Srinivasan 2001).

Thermal treatment (physical activation) consists of two stages, where both stages take place separately. The carbonization stage occurs first to convert the raw material into a carbon-rich substrate. Typically, this carbonization is conducted under an inert atmosphere using N_2- or CO_2-rich gas between 400°C and 700°C, followed by char activation between 600°C and 900°C (Cuhadaroglu and Uygun 2008). The aim of the carbonization is to remove the oxygenated and volatile compounds and generate some initial porosity in the resulting carbonized material. After subsequent reactions in the presence of activating agents, such as steam, CO_2, air, or some combination of these oxidizing agents (Sudaryanto et al. 2006), the activation step induces reactions of the remaining oxygen components present in the carbonized material. During the activation, both carbon monoxide and carbon dioxide are generated, resulting in the creation of new pores and an increase in surface area (McDougall 1991 and Porado et al. 2017). The development of physical pores during the activation process can be classified into three phases: creating channels that connect previously inaccessible pores, developing new pores, and widening existing pores (Li et al. 2008). The characteristics of pores created during the activation can be varied by the types of precursors, reaction temperature, time, and inert gas employed for the activation.

Chemical activation, also known as wet oxidation, differs from physical activation. This is because the process can conduct carbonization and activation simultaneously. During the chemical activation, the precursor is subjected to thermal treatment and activation at the same time (Al-Qodah and Shawabkah 2017; Sutcu 2021; Thongpat et al. 2021; Banivaheb 2017). As the name implies, chemical activation requires a reactant impregnated with the raw material (by soaking) to help generate the AC porous network (Abdullah et al. 2001; Thongpat et al. 2021; Sultana and Reza 2022). Chemical activation generally requires lower reaction temperatures compared to physical activation. Commonly, the temperature ranges for chemical activation are between 300–700°C versus 600–900°C for physical activation (Girgis et al. 2002; Alhamed 2006; Giraldo and Moreno-Pirajan 2012). The properties of AC produced by chemical activation are determined by the chosen activating reactants and their ability to create the desired functional groups on the surface of the AC during the activation process. Typically, reactants such as H_3PO_4, $ZnCl_2$, H_2SO_4, KBr, NH_4Br, KCNS, H_2O_2, $KMnO_4$, KOH, and NaOH can be employed for chemical activation. Figure 3-18 summarizes the differences between both production pathways.

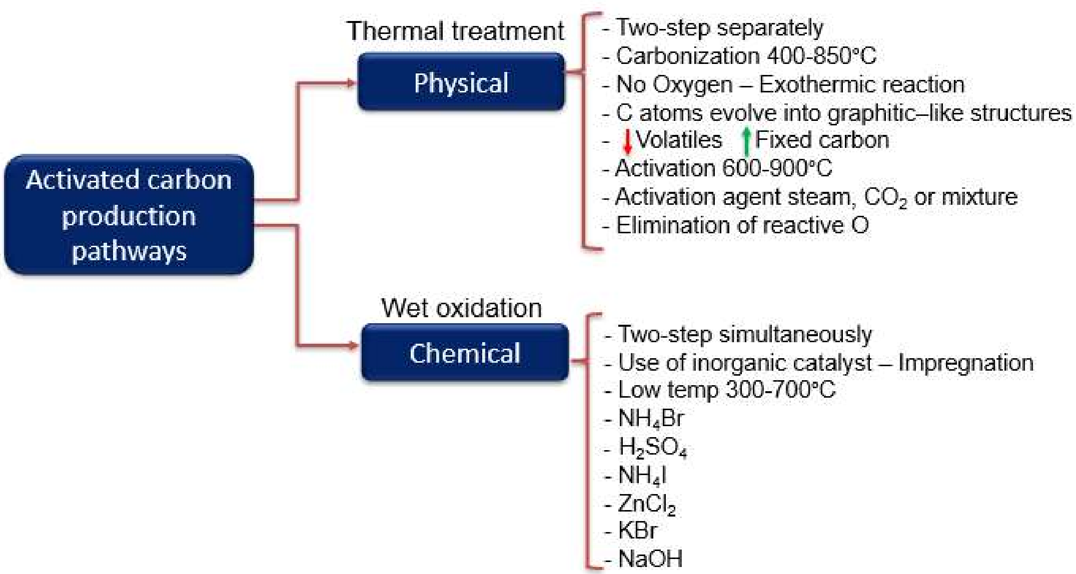

Figure 3-18. AC production pathways.

3.8.1 Model Description

According to the physical AC production process, a two-staged model is developed using the process simulation software package Aspen Plus. The model is mainly composed of two parts: carbonization and steam activation. Here, it is assumed that coal carbonization takes place in the pyrolysis block, and the coal-char solids are later used as precursors in the AC production block. The NC coal feed components are first dried and decomposed in the coal pyrolysis block, which can be used to model the carbonization stage. The proximate and ultimate analyses of coal-char used in this block are shown in Table 14.

Table 14. Proximate and ultimate analysis of dry coal and char from pluralized coal used in the AC simulation block.

Parameter	Dry Coal (Pittsburgh #8)	Char from Pluralized Coal in 300–550 µm
Moisture	—	—
Ash	10.65 (0.94)	16.39 (1.35)
FC	53.34 (0.94)	69.25 (1.35)
VM	36.01 (0.89)	14.36 (1.83)
C	72.85 (1.23)	72.33 (0.24)
H	5.47 (1.23)	3.3 (0.02)
N	2.92 (0.15)	3.15 (0.04)
S	2.44 (0.12)	3.31 (0.21)
O*	5.67	1.52

The value in parentheses represents the standard deviation calculated from three replicates, and * indicates that oxygen was estimated by difference.

Details of the carbonization (pyrolysis and CPD model) have been previously provided in Sections 3.2 and 3.2.1.1. For the activation process, it is important to mention that ash is assumed to be retained in coal-char and further retained in AC. Since coal-char is considered an NC compound and could not be easily dealt with by Aspen Plus, coal-char was initially decomposed into carbon, hydrogen, oxygen, sulfur, and ash in an RStoic block; in addition, a calculator block was used to correlate the proximate and ultimate analysis to its decomposition. Subsequently, part of the carbon (~75 wt%) contained in a CHAR-4SG stream and all ash are separated in a separation (SEP) block as AC, and the rest of the elemental compounds are then sent into the activation reactor. A Gibbs Reactor (RGIBBS) block is used to model the char-steam reactions carried out in the activation reactor. For Gibbs model calculation, equilibrium was restricted by nine main chemical reactions for a more accurate evaluation performance; these reactions are shown in Table 15. The AC production block is shown in Figure 3-19.

Table 15. Main char-steam activation reactions during the AC production model.

Reaction No.	Reaction [w-w]	Enthalpy (kJ/mol)
R1	$C + H_2O \longrightarrow CO + H_2$	$\Delta H = -135.0$
R2	$C + CO_2 \longrightarrow 2CO$	$\Delta H = -173.3$
R3	$CO + H_2O \longleftrightarrow CO_2 + H_2$	$\Delta H = 41.0$
R4	$C + 2H_2 \longrightarrow CH_4$	$\Delta H = 84.3$
R5	$CH_4 + H_2O \longleftrightarrow CO + 3H_2$	$\Delta H = -21.9$

Reaction No.	Reaction [w-w]	Enthalpy (kJ/mol)
R6	$C + 0.5O_2 \longrightarrow CO$	ΔH = −110.0
R7	$C + O_2 \longrightarrow CO_2$	ΔH = −392.5
R8	$CO + 0.5O_2 \longrightarrow CO_2$	ΔH = −283.0
R9	$H_2 + 0.5O_2 \longleftrightarrow H_2O$	ΔH = −242.0

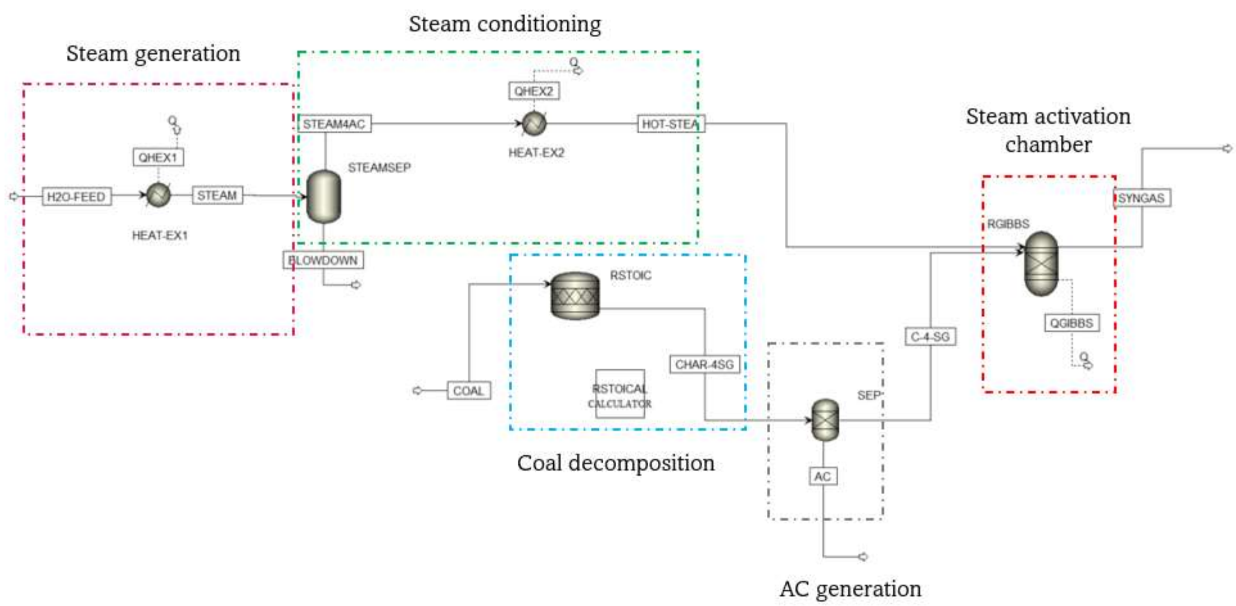

Figure 3-19. AC production model through physical (steam only) activation.

3.8.2 Model Validation and Results

For the proposed AC production model through physical activation, two different initial conditions were assumed, where 150 kg/h of coal and 300 kg/h of steam were chosen as the first route to assess the implications in the gas composition. Here, it is important to note that, industrially, the coal-to-steam ratio is 2:1 for enhancing the porous network development and the oxygenation of the most reactive carbon sites of the carbon solid. Then, a second route was proposed by using 300 kg/h of coal and 150 kg/h of steam to provide insights into the impact of the gas composition by limiting the steam flow in the char-steam reactions shown in Table 15. The summary of both initial conditions is shown in Appendix C-4; in both cases, AC yields were controlled at 37.8%. Later, a sensitivity analysis was developed to evaluate the implications on syngas stream composition as a function of different steam loads up to 400 hg/h. A similar test assessed the activation temperature impact in the RGIBBS block in the composition of the syngas stream. Both analyses were carried out to evaluate further engineering improvements and variations by using or recirculating these compounds onto the HTG block to maximize methanol and olefines (for polymer production) and improve the overall process economics.

The main assumptions considered are:

1. Coal can be decomposed in C, H, N, O, and S using a stoichiometric (STOIC) reactor.
2. All ash is retained in AC after the SEP block.
3. AC yields are assumed to be between 35 and 40 wt%.
4. The 60–65 wt% of the carbon content on coal-char react on steam char activation.
5. AC is composed of carbon and ash.
6. Heat loss is not considered.
7. The hydrodynamic effect is not considered.

Considering the variations in steam load for both cases, Figure 3-20 and Figure 3-21 clearly show that the increasing amount of steam up to certain feed loads significantly affects the equilibrium reaction state and benefits the reaction toward CO_2 and H_2O production. In addition, an important increment on CH_4 and H_2 consumption is noticed at the steam feeds up to 160 and 320 kg/h, respectively. Figure 3-20 and Figure 3-22 suggest that CO_2 production grew rapidly since Reaction 3 led the process kinetics. Similarly, Reaction 5 entirely describes the fast decomposition of CH_4 toward H_2 and CO production. The reaction extent on Reaction 5 is believed to be smaller than the one in Reaction 3, which cannot meet the CO produced, and therefore, most of this compound is immediately converted to CO_2. This correlates to its noticeable rate of production in the presence of steam excess; due to the reversibility on both reactions and their low enthalpy of formation, these two reactions clearly drive the syngas composition. As expected in both cases, the composition of H_2O must increase as more steam is used in the system and will rapidly increase right after 160 and 320 kg/h, respectively.

The assumed Gibbs equilibrium model can accurately predict the composition of syngas in the coal-char activation process, except for methane. In this case, the yield and molar fraction of methane predicted by the Gibbs model is close to zero; since as seen on Reaction 5, most of it is converted to CO, and the H_2 produced in the reaction is not enough to meet the need of 2 moles per carbon mole to produce one molecule of methane. This also can explain the decrease in H_2 production after 160 and 320 kg/h, respectively. However, the relative concentration of methane is much lower than other gaseous compounds. Therefore, this behavior does not have a major impact on the prediction of the thermal and stoichiometry balance generated by this model. It is important to note that, for process improvement and economics, a desirable H_2-to-CO ratio of two is desired which, due to the kinetics of the system, cannot be achieved without an external source of H_2.

For the sensitivity test, variating the reaction temperature shown in Figure 3-21 and Figure 3-23 in the first-case scenario for temperatures above 890°C, this H_2-to-CO mole ratio cannot be achieved. This led to a more detailed analysis of the reaction kinetics and process conditions dependence to achieve this ratio if the syngas stream is recirculated to the HTG block. While for the second case scenario, it seems that the mole fraction almost reaches the desired H_2-to-CO mole ratio. Nevertheless, in the latter case, the coal needed must be twice the amount of steam, which is not a practical or realistic condition since there is a steam-limited environment leading to a poor porous network and lower surface functionalization of oxygenated compounds.

The effect of the following operating conditions on the reactivity and adsorption characteristics of the steam ACs are the key parameters to consider on their engineering performance: carbonization conditions (one- and two-step activation), activation temperature (800°C–850°C), and steam gas velocity (1.5–3× the minimum fluidization velocity). Carbonization conditions considerably affect the reactivity of the chars obtained—the faster the carbonization process, the higher the reactivity. In both cases, the carbonization is assumed constant, occurring at 700°C since, according to the CPD model described in Section 3.2.1.1, temperatures above this level do not impact coal-char yields. On the other hand, both temperature and steam flow rate (affecting the reaction rate) have a marked effect on the development of porosity and, therefore based on the literature found (see Table 18), seems to fall within 750°C–850°C (Gullon et al. 1996; Chen et al. 2015). While steam gas velocity has not been considered in this base case, the rate of steam to coal is suggested as two for surface characteristic improvement.

As seen in Table 16, the model validation results show a highest burn-off percentage at lower temperatures under the steam environment compared with the highest activation temperatures and CO_2 environment. This trend is expected due to the nature of the activating agent, within CO_2 conditions, the majority of oxygen molecules react with the most active carbon sites and the CO in a vapor phase to evolve to CO_2, thus leaving less O_2 to react in vapor phase. While under steam conditions because of the thermal decomposition of H_2O, the reaction with the carbon substrate produces CO, CO_2, and CH_4, reducing the solid yield and increasing the gas production (burn-off). While, under similar temperature conditions and using a steam-to-coal ratio in bench-scale experiments, the results from process modeling fall within the same values obtained by Teng et al. (1997) or Gullon et al. (1996). It is important to mention that the small extent of discrepancies could be due to the lab-scale equipment used, as well as the model assumptions (Teng et al. 1997). Around this model validation, lower temperatures and a coal-to-steam ratio of two led to burn-off values close to the theoretical gas decomposition mechanisms and therefore provided similar yields.

Table 16. Impact of processing conditions in bituminous coals: bench scale versus model outputs.

Bituminous Coal	Origin	Act. Temp (°C)	Activating Agent	CO_2 or Steam:Coal	Burn-Off (%)	BET (m^2/g)	Reference
Black Water	Australia	800	CO_2	1	36	360	Gullon et al. 1996
Gregory	Australia	800	CO_2	1	40	345	Gullon et al. 1996
Mt. Thorley	Australia	800	CO_2	1	41	545	Gullon et al. 1996
Maria Isabel Mine	Spain	850	Steam	1.5	65	Not available	Teng et al. 1997
Maria Isabel Mine	Spain	800	Steam	1.5	58	Not available	Teng et al. 1997
Pittsburg #8	USA	700	Steam	2	62.2	Not determined	Aspen model
Pittsburg #8	USA	700	Steam	0.5	62.2	A poor porous network and lower surface functionalization extend	Aspen model

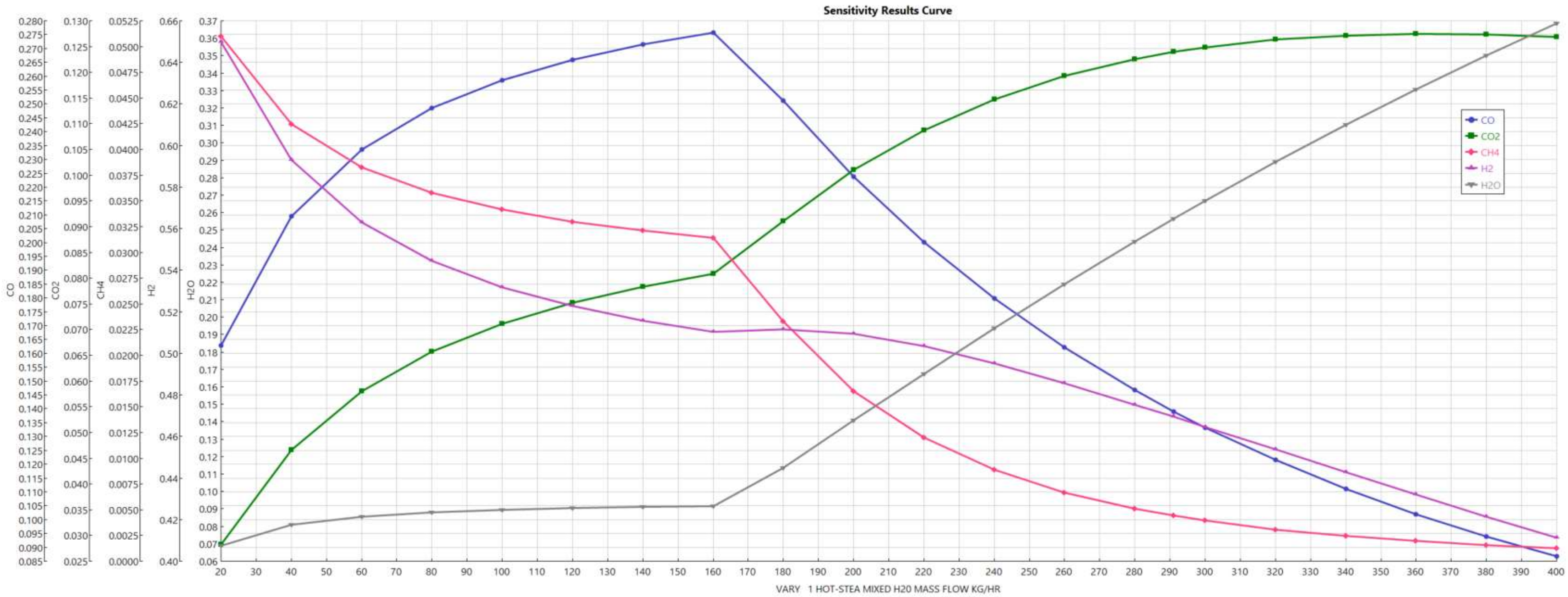

Figure 3-20. Sensitivity analysis on syngas composition by variating steam loads for 150 kg/h of coal and 300 kg/h of steam.

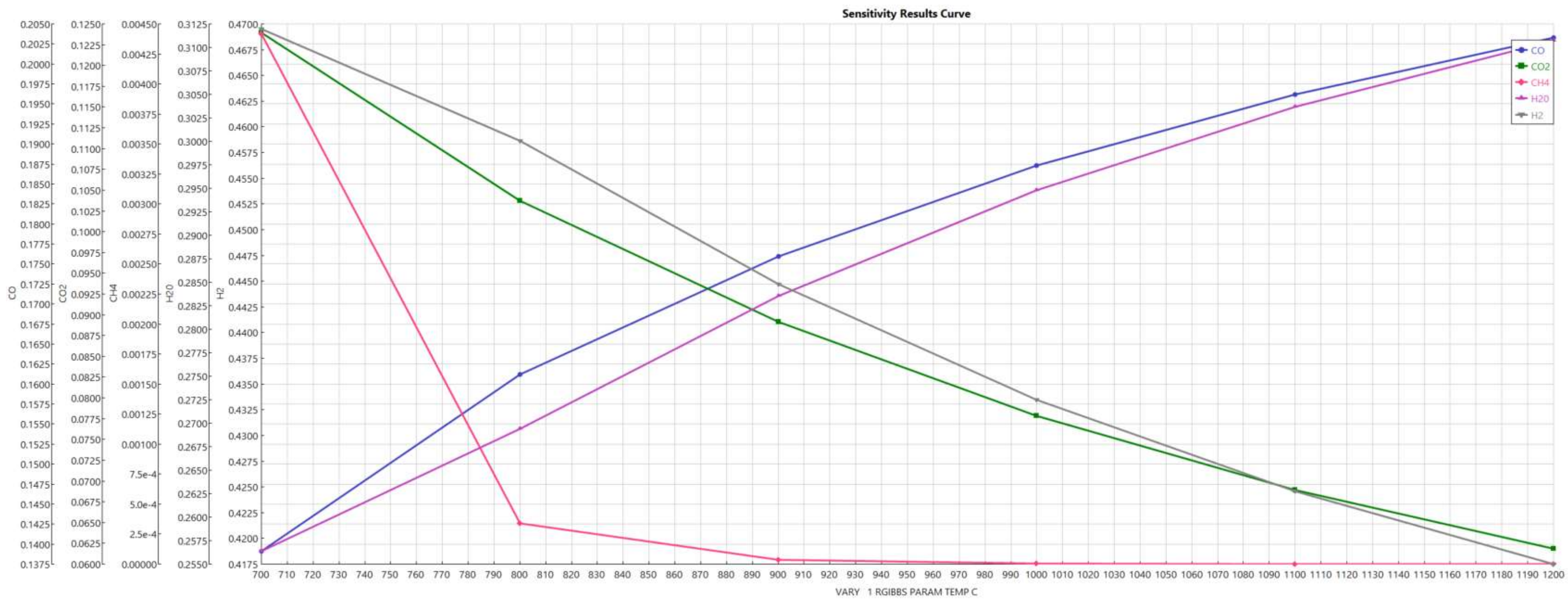

Figure 3-21. Sensitivity analysis on syngas composition by variating RGIBBS temperature for 150 kg/h of coal and 300 kg/h of steam.

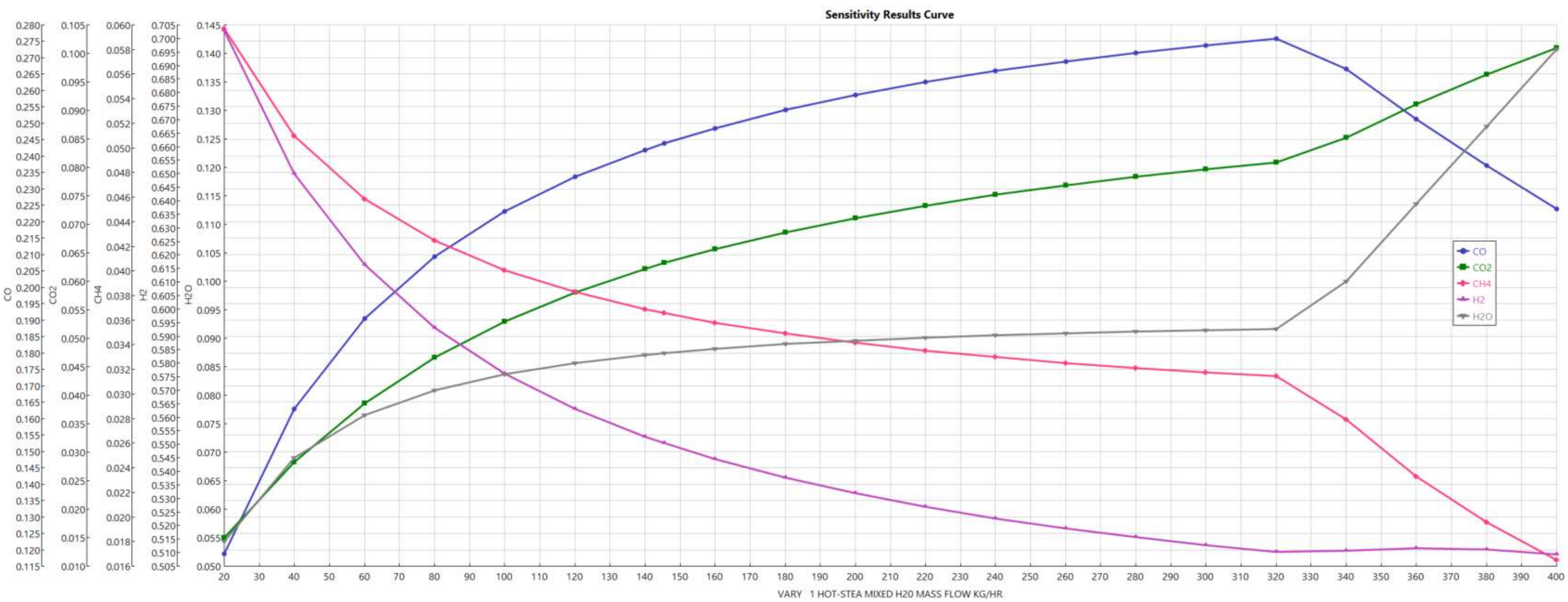

Figure 3-22. Sensitivity analysis on syngas composition by variating steam loads for 300 kg/h of coal and 150 kg/h of steam.

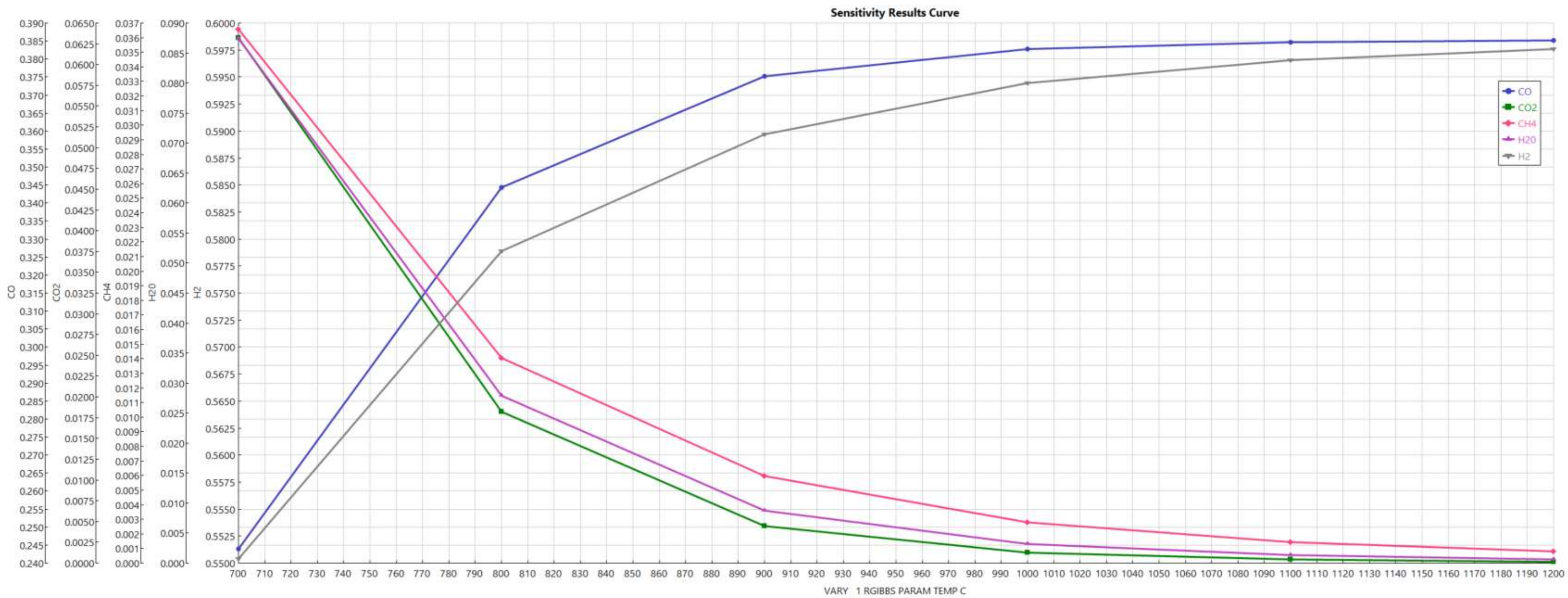

Figure 3-23. Sensitivity analysis on syngas composition by variating RGIBBS temperature for 300 kg/h of coal and 150 kg/h of steam.

3.9 Methanol Synthesis

One of the conventional methanol synthesis methods is converting a gas mixture consisting of CO, CO_2, and H_2 using a Cu-Zn-Al catalyst. In the synthesis reactor, each hole is filled with catalyst pallets and the gas mixtures are introduced under operating conditions of about 250°C and 100 atm. Temperature is controlled by cooling water flowing over the reactor. Figure 3-24 shows the example of a tubular flow reactor used for methanol synthesis.

Figure 3-24. Tubular flow reactor.

The diffusion step to the catalyst surface occurs quickly, and the chemical reaction on the surface is a reaction-determining step. Both CO and CO_2 can directly be converted into methanol; however, if either is introduced without the other, the carbon conversion to methanol is quite low (~10%). The carbon-to-methanol conversion rate can be enhanced up to 70% by using a mixture of CO and CO_2. Figure 3-25 shows the conversion of carbon as a function of a CO/CO_2 mole fraction. CO and CO_2 can be converted back and forth via the steam gas shift reaction. It is expected that the reverse gas shift reaction is dominant according to the Gibbs free energy, but the direction of the reaction is determined by the reactant and products' concentration. There are many studies to explain why maximum conversion is obtained with CO/CO_2 mixture, but the reaction mechanism is still in debate:

- (Reaction A) CO hydrogenation: $CO + 2H_2 \rightleftarrows CH_3OH$
- (Reaction B) Reverse water gas shift reaction: $CO_2 + H_2 \rightleftarrows CO + H_2O$
- (Reaction C) CO_2 hydrogenation: $CO_2 + 3H_2 \rightleftarrows CH_3OH + H_2O$.

The Langmuir-Hinshelwood-Hougen-Hatson model is usually employed as the reaction rate model for methanol synthesis with a Cu-Zn-Al catalyst. This model assumed that the adsorption and desorption rate is faster than the reaction rate, and thus the time-derivative of site concentration of the catalysis can be considered zero. Some of the suggested Langmuir-Hinshelwood-Hougen-Hatson (LHHW) model is tabulated in Table 17. Each model has different assumptions on deposition and reactions. Graaf et al. (1986, 1988, and 1990) insist that carbon-related material (CO/CO_2) is attached on the copper of the catalysis and that hydrogen-related material (H_2 and H_2O) are attached on the Zn site of the catalysis.

Hydrogen and carbon-containing gases are dissociated on the catalyst surface, and methanol (CH_3OH) is synthesized when the dissociated species react with each other.

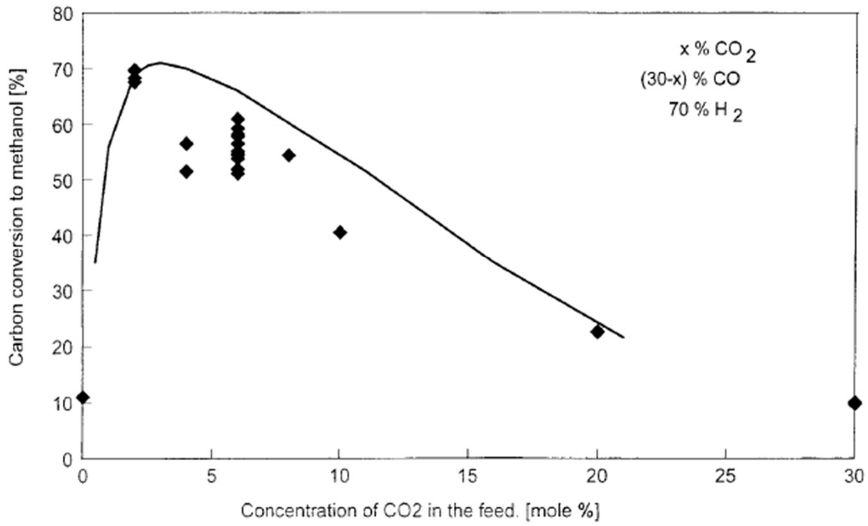

Figure 3-25. Carbon conversion to methanol as a function of concentration of CO/CO_2. Data from model prediction (Bussche and Froment 1996) in line and experimental data (Klier et al. 1982) in dots.

Table 17. References of kinetics model for methanol synthesis.

References	Catalyst	Reactants	Range of Temperature and Pressure	Reactions Considered	Feed Composition (mol %)
Graaf et al. 1986, 1988, and 1990	$Cu/Zn/Al_2O_3$ (Haldor Topsoe MK-101)	$CO/CO_2/H_2$	210°C–275°C, 15–50 bar	A, B, C	CO, 0–22; CO_2, 2–26; H2, 67.4–90
Van den Bussche and Froment 1996	$Cu/ZnO/Al_2O_3$ (Imperial Chemical Industries, ICI 51–2)	$CO/CO_2/H_2$	180°C–280°C, 15–51 bar	B, C	CO, 0–30; CO_2, 0–30; H_2: 70
Park et al. 2014	$Cu/ZnO/Al_2O_3$ (MegaMax 700, Süd-Chemie)	$CO/CO_2/H_2$	220°C–340°C, 50–90 bar	A, B, C	CO, 0–32; CO_2, 0–24; H_2, 50–83
Skrzypek et al. 1991	$CuO/ZnO/Al_2O_3$ (Blasiak)	$CO/CO_2/H_2$	187°C–277°C, 30–90 bar	B, C	CO, 0–20; CO_2, 5–35; H_2, 10–80
Villa et al. 1985	$Cu/ZnO/Al_2O_3$	$CO/CO_2/H_2$	473°C–543°C	A, B	—

3.9.1 Model Description

The methanol synthesis process model is built based on INL report TEV-667 (Idaho National Laboratory 2010) and INL report TEV-1567 (Idaho National Laboratory 2018), and exemplary case model included in Aspen Plus V11, represented in Figure 3-27. A $CO/CO_2/H_2$ gas mixture is introduced into a plug flow tubular reactor consisting of 4,000 cylindrical tubes with lengths of 12.2 m and diameters of 0.0762 m, filled with the catalyst. The reaction model suggested by Van den Bussche and Fremont (1996) is used for the reaction kinetics, and the Soave-Redlick-Kwong model is used for the equation of state. The catalysis information is specified as: bed voidage of 0.5 and particle density of 2,000 kg/m^3. The reaction is exothermal, so the temperature is controlled by coolant fluid. The reactor is assumed to be isothermal with the inlet temperature. The products produced (a mixture of methanol, water, and unreacted reactant) are cooled downstream the reactor, and only methanol and water is condensed. Unreacted reactant (or light gas) are separated from liquified methanol and water solution (crude methanol) at the flash drum (ME-FLASH). Then 80% of gas phase stream from the flash drum is refluxed back to the reactor to improve the product yields while the remaining gases are purged. The liquid phase stream containing methanol from the flash drum goes forward to two series of distillation towers. The first distillation tower separates the methanol-water from the mixture after the reactor. The second distillation tower purifies the methanol from the methanol-water mixture. The RadFrac distillation tower unit is employed in Aspen Plus. The amount of reflux ratio and distillate-to-feed ratio is controlled by the specified mole purity for each outlet stream from the distillation columns. The first distillation tower separates light gas from methanol, and water is limited to 0.5 wt%. In the second distillation tower, methanol purity of the upper stream and water purity of the second distillation tower are limited to 0.5 wt% and 0.5 wt% or lower, respectively.

3.9.2 Model Validation

The $CO/CO_2/H_2$ gas mixture is introduced into the plug flow reactor at a mass flow rate of 10 tonne/day at 280°C and 50 bar. The mole fraction is specified as 15:5:70, which is the ratio expected to maximize methanol yields. The reactor condition is isothermal at 280°C. The first distillation tower has 10 stages, and feed is introduced in the second stage from the top. The second distillation tower has 50 stages, where the feed is introduced at Stage 20. The result of the synthesis model is that 72.28% of CO/CO_2 feeds are converted to methanol in high purity of 99 wt%.

If the plug flow reactor is large and filled with enough catalyst, the reaction will proceed to reach chemical equilibrium. Thus, the result of Gibbs energy-based equilibrium reactor (RGibbs) is supposed to be similar to that of a large plug flow reactor with ambient catalysis. Figure 3-26 represents the Aspen Plus model used for validating the kinetic-based chemical reaction. Two different reactor models are compared: a kinetic-based reactor model and a Gibbs reactor model. Table 18 represents the mole fraction downstream of each reactor, and their results looks similar, concluding that the reaction kinetics model is acceptable.

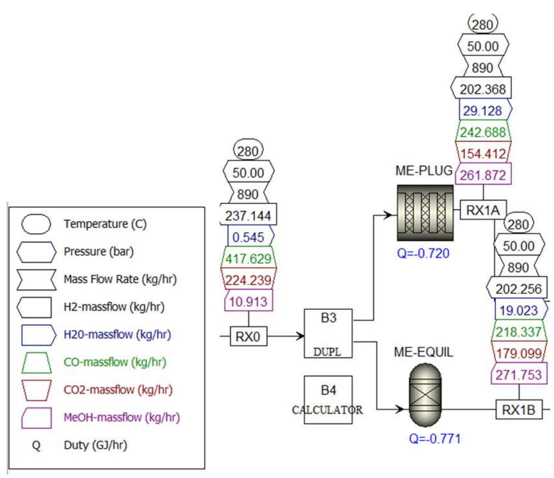

Figure 3-26. Result of methanol synthesis by two different model for chemically equilibrium condition.

Table 18. Mass fractions after the kinetic-based plug flow reactor and equilibrium-based Gibbs reactor reactors.

Component	Feed	Mole Fraction Downstream Plug Flow Reactor	Mole Fraction Downstream Gibbs Reactor
H_2	0.266314	0.22726	0.227134
H_2O	0.000612	0.032711	0.021363
CO	0.468998	0.272539	0.245194
CO_2	0.251821	0.173406	0.201129
MEOH	0.012255	0.294083	0.305180

3.9.3 Model Results

The real-scale model for methanol synthesis is performed using the preliminary model tested in the previous section with some modification. Figure 3-27 shows the flow diagram of the Rectisol process and its simulation result. The amount of light gas introduced to the methanol synthesis is 19,200 kg/h, and its composition is shown in Table 19. The conventional way to adjust the ratio of CO, CO_2, and H_2 in the inlet gas stream is to use a water gas shift reactor prior to the synthesis reactor. In TEV-667 (Idaho National Laboratory 2010), the authors compared the results of adjusting the ratio with a water gas shift reactor and adjusting the ratio by injecting hydrogen produced from HTSE. This did not affect the methanol conversion rate but reduced the capital costs by eliminating the reactor equipment. In this study, hydrogen from HTSE is introduced similarly to increase the MEOH conversion rate. If an extra 1,000 kg/h of hydrogen is introduced to the inlet gas stream, the conversion of carbon to purified methanol (MEOH) is 85.2% with a purity of 99.8%. Without the additional hydrogen added to adjust the ratio, the conversion rate of carbon to methanol is 60.6%.

Table 19. Mass composition of inlet gas for methanol synthesis.

	CO	CO_2	CH_4	C_2H_4	N_2	H_2	H_2S	MEOH
Mass flow [kg/h]	16,214	412	284	0.0002	83.3	2,218	0.0009	1.718
Mass fraction [-]	0.844	0.021	0.015	1.35E-8	0.004	0.115	4.99E-8	8.94E-5

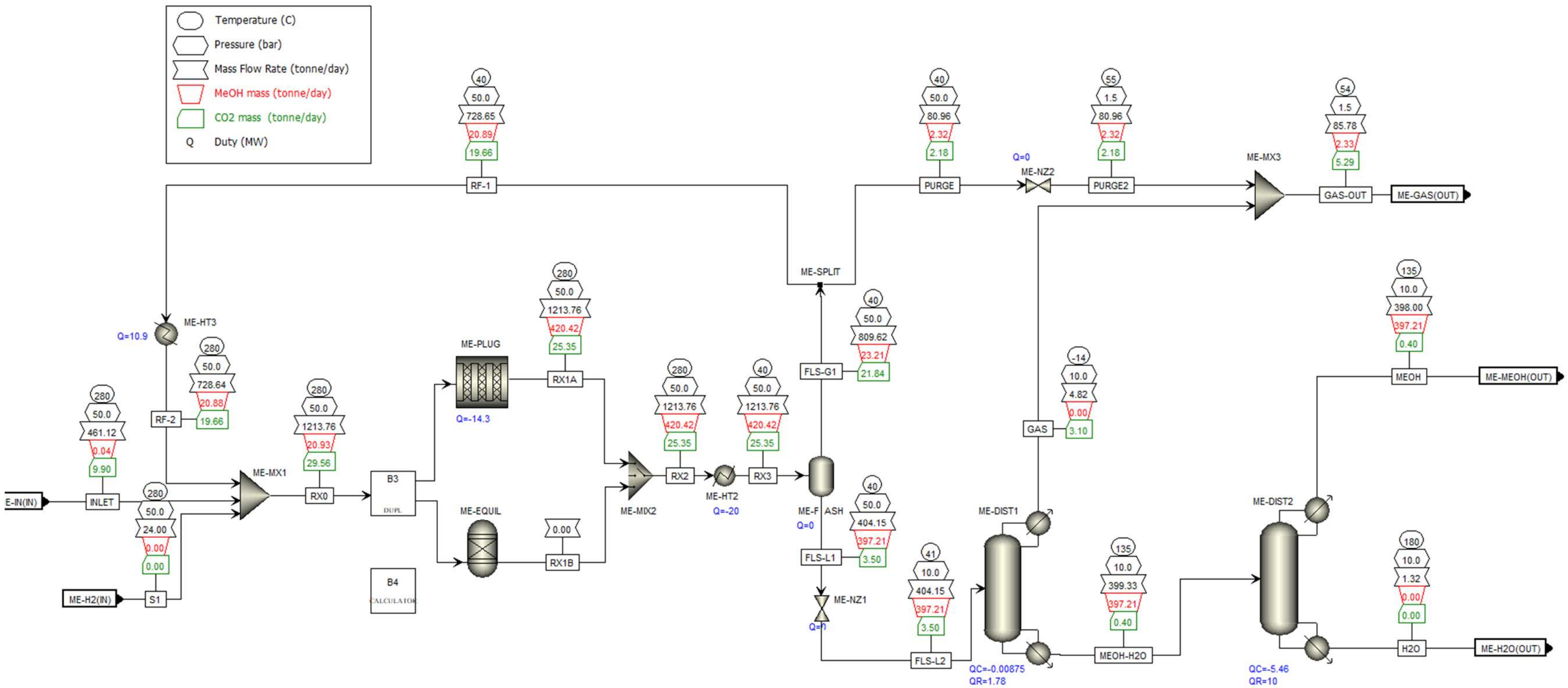

Figure 3-27. Flow diagram of methanol synthesis with extra hydrogen supply.

3.10 Combined Model Results

The component balance for each unit of the entire coal refining process is calculated and tabulated in Table 20. From an incoming coal feed of 1,000 tonne/day, the products produced are AC at 338.6 tonne/day, methanol at 398 tonne/day, carbon dioxide at 190.32 tonne/day, and sulfur at 2 tonne/day through the entire coal refining process. The current results are shown without considering the processing of syngas produced by the AC, which would increase the total methanol yield and CO_2 capture. The light gas produced after the AC process is not recycled and employed in this model.

Since methanol is the only feed source of carbon atoms in this process, how many carbon atoms from coal are distributed into each output can be a criterion to quantify how much coal is usefully employed. Table 21 represents the mass flowrate of carbon atoms at each output stream. The amount of carbon atom to target products (AC, methanol and high purity CO_2) are 47.7, 15.6 and 7.4 wt% respectively, concluding that 70.7 wt% of coal is usefully employed. Approximately two thirds of usually used coal is converted into AC. As the light gas produced as a byproduct of AC, mostly comprised of CO_2 and syngas, is release into the atmosphere without any regeneration and reflux back to the process, the carbon atoms lost in the AC process accounts for 21 wt% of entire carbon atom feed into the system. Furthermore, some CO and CO_2 is not captured and is released into the atmosphere during AC process. Coal usage efficiency can be enhanced if we are able to reuse this wasted light gas into the Rectisol process and methanol synthesis. Further development of the process model is necessary in future work.

The energy balance for each unit of the entire coal refining process is calculated and shown in Table 21. The pyrolysis unit requires the largest heat input of any process. Most of the heat energy is consumed to increase the sand temperature, which is used for heating and transporting pulverized coal. The steam reforming unit requires the highest electric duty because it requires a compressor to produce a large pressure change. On the other hand, heat is released in the AC process and methanol synthesis units where exothermic reactions are dominant. It might be necessary to recuperate the heat generated from the unit to improve the efficiency of the process in future study. If considering the energy requirement portion for methanol synthesis and CO_2 capture as listed in Table 21, a minimal energy of 0.7 GJ is required to produce a tonne of methanol and minimal energy of 0.926 GJ is necessary to capture a tonne of CO_2 in high purities, respectively. Note that this amount of energy calculated here does not include inherent energy from the feed and product. Table 23 provides a summary of the mass and energy balances at the plant.

Table 20. Mass balance of each component at each unit.

Unit [tonne/day]	IN	OUT
Coal		
Pyrolysis	1,000	—
AC		
AC Production	—	338.6
Ash		
AC Production	—	102.3
CO_2		
Pyrolysis	240	—
Rectisol 1	—	266.4
Rectisol 2	—	14.64
Claus Unit	—	146.92

Unit [tonne/day]	IN	OUT
H_2O		
AC Production	312	406
Hydrothermal Gasification	7,200	6,936
Autothermal Reforming	120	203
Methanol Synthesis	—	1.32
O_2		
AC Production	357	—
Autothermal Reforming	120	—
Claus Unit	1	—
H_2		
Methanol Synthesis	24	—
Light Gas		
AC Production	—	446.40
Methanol Synthesis	—	85.68
MEOH		
Methanol Synthesis	—	398
Sulfur		
Claus Unit	—	~2
$HgCl_2$		
Mercury Removal	—	<0.01

Table 21. Carbon atom balance.

	Mass of Carbon Atom in Each Stream [tonne/day]	Yield to Carbon in Coal Feed [%]	Characteristics of Stream
Coal	710.1	—	Feed
Activated carbon	338.6	47.7	Target product
Methanol	149.0	15.6	Target product
CO_2 captured at Rectisol process*	52.6	7.4	Target product
Light gas from activated carbon	110.5	21.0	Flue gas
HTG dirty water	15.6	2.2	Effluent
ATR dirty water	0.4	0.1	Effluent
Light gas from MEOH synthesis	25.7	3.6	Flue gas
Other	17.7	2.5	—

*Amount of C in CO_2 recycled (65.5 tonne/day) is subtracted from the total amount C in CO_2 captured (118.13 tonne/day)

Table 22. Energy requirement for each unit of the process.

	Heat required to the System [GJ/hour]	Electricity [GJ/hour]	Energy Requirement [GJ/tonne Coal]	Portion for Methanol [%]	Portion for CO_2 [%]
Drying	7.10	—	0.170	22.1	10.5
Pyrolysis	34.00	—	0.815	22.1	10.5
AC Production	−226.28	—	−5.431	0	0
Hydrothermal Gasification	12.47	19.79	0.774	67.8	32.2
Autothermal reformer	17.03	58.80	1.820	67.8	32.2
Mercury Removal	13.42	—	0.322	67.8	32.2
Rectisol Unit	−9.81	9.22	−0.014	67.8	32.2
Claus Unit	−0.99	—	−0.024	67.8	32.2
Methanol Synthesis	−61.26	—	−1.470	100	0

Table 23. Mass and energy balance Summary.

Unit [tonne/day]	IN	OUT
Coal	1,000	—
AC	—	339
Ash	—	102
CO_2	—	428
Water	7,632	7,546
Oxygen	478	—
Hydrogen	24	—
Light Gas	—	532
Methanol	—	398
Sulfur	—	~2
$HgCl_2$	—	Small
Unit [MW]	IN	OUT
Heat	23	83
Electricity	24	—

3.10.1 Hydrogen Production

The total of refinery processes requires 24 tpd H_2, which would be generated from an HTSE unit supplied by the nuclear power plant (NPP). According to Wendt et al. (2022), an HTSE requires 36.8 kWh-e and 6.4 kWh-t per kg H_2. At a demand of 24 tpd H_2, the refinery requires 35.3 MW-e and 6.1 MW-t solely for hydrogen production if it operates at 100% capacity.

3.10.2 Formic Acid Production

FA can be generated by combining H_2 and CO_2 in a reactor to produce HCOOH. 428 tons/day CO_2 is produced by the carbon refinery, which can be converted to FA. Pérez-Fortes et al. (2016) published a model of FA production through the direct hydrogenation of CO_2. Table 24 gives the resulting mass and energy balance for the process. Approximately 1 ton of FA is generated from 0.834 tons CO_2 and 0.06 tons hydrogen. The equilibrium equation requires 1 mol H_2 and 1 mol CO_2, but the mass of CO_2 required is much larger than that of hydrogen because CO_2 is a heavier molecule.

Table 24. Material inputs and outputs for a proposed FA model.

Material	**Inlet**	**Outlet**
CO_2 (kg)	0.834	0.166
H_2 (kg)	0.060	0
H_2O (kg)	0 (electrolyzer not considered)	0.60
Make-ups (catalyst, solvent, amines) (kg)	0.266	0
FA (kg)	0	1
Electricity consumption (without electrolyzer) (MWh/tFA)	0.296	—
Heating needs (MWh/tFA)	2.783	—
Cooling needs (MWh/tFA)	2.962	—

At a ratio of 1 ton FA to 0.834 tons CO_2, the carbon refinery has the potential to produce over 500 tons FA per day, per Table 25. If the global annual market for FA is 750,000 tons per year, the refinery alone would generate 25% of the market every year. This is an unfeasible result at this refinery capacity. If the refinery was much smaller, FA could be used as the total share of the products generated from CO_2. Alternatively, FA could be one of several CO_2 products generated at the refinery.

Table 25. Potential for FA production at the carbon refinery

Material	Inlet (tpd)	Outlet (tpd)
CO_2	428	85
H_2	31	—
FA	—	513
Electricity (MWh)	152	—

FA is also a small market compared to some other products that can be made through CO_2 utilization pathways. Other product pathways, like urea, or a local market for compressed CO_2 could enhance the market viability of the refinery.

Adding FA production would require an additional 31 tpd hydrogen from the electrolysis unit, for a total of 55 tpd. This would increase the required NPP capacity to 80.9 MWe and 13.9 MWt. FA production also requires electricity for compression processes, which would increase the NPP capacity requirement by 6.3 MWe.

4. CONCLUSION

The purpose of this work is to explore the possibilities of using coal as a carbon resource in a "coal refinery" by converting the coal to fuels and chemicals using energy provided by an NPP. For a 1000, tpd bituminous "coal refinery," there are 339 tons of AC produced and 398 tons of methanol produced per day. The methanol yield could be increased by processing the syngas created from the activated carbon production unit. There is a possibility to utilize the captured CO_2 from the process to produce 513 tons per day of formic acid. This would require at least 24 MWe and 23 MWt from a NPP to power the refinery from the coal drying stage to methanol synthesis. This requirement could be lowered with heat recovery from the methanol synthesis and activated carbon process. An additional 80.9 MWe and 13.9 MWt from a NPP would be dedicated to produce hydrogen through HTSE for the methanol synthesis process and formic acid production. Finally, 6.3 MWe capacity would be required for formic acid compression. The total NPP capacity required would be about 111 MWe and 37 MWt. This capacity requirement could be satisfied by a typical SMR size of 300 MWe.

This user case is intended to explore methods of converting coal into valuable chemical products: AC, methanol, CO_2, etc. This exploration includes new ideas about how to deal with char, the solid output of coal pyrolysis, and tar, the liquid output of coal pyrolysis. Instead of ordinary coal gasification operated at a very high temperature with combustion, we suggested pyrolysis followed by alternative SW gasification (or hydrothermal gasification) processes operated in relatively low temperature. AC can be obtained and retrieved through the new process. In addition, tar has long been considered a harmful byproduct of coal, but by breaking down tar in hydrothermal gasification, it was able to be eliminated and transformed into syngas. If necessary, char can also be turned into extra syngas through the HTG process, instead of producing AC. The combination of processes employed in the carbon refinery resulted in multiple product pathways and minimal greenhouse-gas emissions, capturing or eliminating harmful substances from coal, mercury, and tar. The modeling work for this case is complete, and the results are presented in this report.

The pyrolysis model is developed using the Aspen Plus model. Component attributes of target coal (Pittsburgh #8 bituminous coal) and its char are investigated and summarized. We used the CPD model to calculate the yields of coal pyrolysis based on temperature, pressure, and component attributes of coal selected, which estimate the selectivity of gas, liquid and solid products from coal pyrolysis, and the amount of main component of gas product. With a parametric study of the CPD model, best pyrolysis operating condition is 500°C and 5 bar. In addition, we designed and proposed a sand circulation system to deliver heat from the heat source to the coal. A recirculation of 600 tonne of sand per day is necessary with heat source of 500°C to fulfill the target temperature (500°C) of coal in the pyrolysis vessel. Sand is separated from char produced using a particle classifier and recycled to the heat delivery circulation. Gaseous products are separated from solid char using a cyclone.

We also developed the process model for hydrothermal gasification. Noncondensable gas is separated from liquid tar, and liquid tar is introduced into the water circulation. Water is heated and pressurized before the reactor. The reactor is designed to operate at 600°C and 250 bar. At least 7,200 tonne of water circulation is required to perform SW gasification to fulfill the concentration of the tar solution in 2.5 wt%

The low-temperature pyrolysis and gasification process produces unwanted methane as a byproduct, which is the weak point in the process. We introduced an autothermal reaction process to remove unwanted methane produced from previous pyrolysis and hydrothermal gasification. As the target material is methane, the vessel is depressurized for operating conditions to be favorable to methanol conversion. High temperatures to the degree that combustion gasification uses is not necessary.

We used the Rectisol process in which a methanol solvent physically absorbs and separates CO_2 from light gas to capture CO_2 as methanol is one of the target products of the process. We found the best specification of distillation towers, such as the number of stages of distillation towers, reboiler duties, and input and output stream stage, for current user case. With this design specification, the process achieves a CO_2 recovery of 97.7% in approximately 97 wt% purity of CO_2 gas output. Of the CO_2 passing through the Rectisol process, only 2.28 wt% of it is not captured and then introduced to the methanol synthesis process. This is acceptable because small amounts of CO_2 introduced to the methanol reactor enhances methanol conversion. CO_2 released to the atmosphere after the methanol synthesis accounts for 1.2 wt% of the CO_2 passed through the Rectisol process. In the end, we used 1,800 tonne/day of methanol as solvent in Rectisol process, and 99 wt% of it is regenerated and used again. All H_2S gas is separated from light gas, and 98% of captured H_2S is sent through the Claus process.

The sulfur recovery in the Claus process model demonstrated an impressive efficiency of around 98.5%. The optimization of sulfur recovery was found to be closely tied to the H_2S/SO_2 ratio, with maximum recovery occurring at approximately 2:1. However, challenges arose during the combustion of acid gas in the reaction furnace, leading to the formation of undesirable byproducts such as COS and CS_2. These secondary reactions involving CO_2, hydrocarbons, and H_2S had a detrimental impact on overall sulfur recovery. To mitigate this issue, we implemented a strategic approach involving hydrolysis reactions, primarily at the initial catalytic converter. Through the interaction of COS and CS_2 with H_2O, these compounds were effectively converted back into H_2S. This process not only minimized the adverse effects of undesirable byproducts but also facilitated the participation of H_2S in the Claus reaction, thereby enhancing the overall efficiency of sulfur recovery in the system.

The study on mercury removal in a coal pyrolysis and combustion plant demonstrated remarkable success, achieving complete elemental mercury removal through conversion and migration either to solid or liquid phases. A detailed analysis of mercury distribution, removal, and emission across the SCR/ESP/WFGD configuration underscored the technology's feasibility and high performance in flue gas decontamination. The ability to catalytically oxidize mercury in SCR units, coupled with efficient removal mechanisms in fly ash and WFGD liquid outlets, showcased the system's efficacy. However, the influence of flue gas components and the wide temperature range of mercury reactions warrant further systematic study for model improvements in the future.

The proposed model for AC production through physical activation showcased versatility by considering different initial conditions with varying steam:coal ratios. The analyses aimed at assessing engineering enhancements, particularly the recirculation of gaseous compounds onto the HTG block, to maximize methanol and olefins for polymer production and enhance overall process economics. Key parameters impacting the reactivity and adsorption characteristics of steam-ACs were identified, including carbonization conditions, activation temperature, and steam gas velocity. Theoretically the speed of the carbonization process significantly influenced char reactivity, with faster carbonization leading to higher reactivity. Temperature and steam flow rate markedly affect porosity development within 750–850°C. While steam gas velocity was not considered in the base case, a suggested rate of two for the steam:coal ratio was proposed for improved surface characteristics. This comprehensive analysis provides valuable insights for future engineering improvements and variations in the AC production process. The light gas produced from the AC process, mostly CO_2, is not recycled back to the main stream and is released into the atmosphere, which is main source of CO_2 emission. Methanol synthesis can be assisted by nuclear heat and steam through HTSE. Providing hydrogen through HTSE eliminates the need for a water gas shift reaction. Hydrogen can also be used in other parts of the refinery for carbon utilization, and the resulting oxygen from electrolysis can be used in the AC production and hydrothermal gasification process.

Coal is the only source of carbon atom in this process. According to the simulation result, 70% of the carbon atom from coal is converted into target product: AC, methanol, and high purity CO_2, and their selectivity are 67.5%, 22.1%, and 10.4%, respectively. Remaining carbon atoms are either released into the atmosphere downstream AC production process in the form of CO and CO_2 or dissolved CO_2 in dirty water. The energy requirement for methanol and high purity CO_2 is 0.7 GJ/tonne methanol and

0.926 GJ/tonne high-purity CO_2, respectively. Overall, the results present a feasible pathway for converting coal to chemical products.

An HTSE process providing hydrogen for syngas conditioning and FA production at the plant would require 80.9 MWe and 13.9 MWt of additional NPP capacity. This is a small capacity compared to a typical SMR capacity size of 300 MW. This indicates that a carbon utilization or methanol conversion project could be a good candidate to share capacity with other nuclear applications or a grid-connected NPP. However, the plant would generate 25% of the global FA market if all the CO_2 output was used for FA production. In future work, the plant capacity should be adjusted to present a more feasible hydrogen requirement. Because FA is such a small market, larger markets like urea should be explored for CO_2 utilization in a future analysis. From these results, carbon conversion through this refinery method would not be sufficient to replace the current coal use in the region. Rather, coal conversion to products should be one of several solutions considered to replace coal-fired power plants. Between West Virginia and Pennsylvania, two of the largest coal producers in the Appalachian region, there is 19.3 GW of coal- fired power plant capacity (Statsita 2023c). The coal requirement to produce electricity is about 173,700 tons of coal per day (Chuang 2020). The coal refinery studied here processes 1,000 tons per day but shows limitations on the potential for CO_2 utilization at this size.

A future analysis of this user case would include a technoeconomic analysis of the various process units required and utilize efficient heat recycling to minimize reactor sizing. The market analysis also showed potential for CO_2 use to increase revenue by converting CO_2 to FA or urea. By demonstrating methanol pathways in this model, a variety of potential markets are available. These results are expected to add to the business case for the coal to nuclear transition, focusing on the mining industry rather than electric infrastructure.

5. REFERENCES

Abdullah, A. H., A. Kasim, Z. Zainal, M. Z. Hussien, D. Kuang, F. Ahmad, O. S. Wooi. 2001. "Preparation and characterization of activated carbon from Gelam Wood Bark (Melaleuca cajuputi)." *Malaysian Journal of Analytical Science* 7(1):65–68.

ACMT. 2021. "Global Activated Carbon Market by Type, Application Liquid Phase (Water Treatment, Foods & Beverages, Pharmaceutical & Medical), Gas Phase (Industrial, Automotive), and Region (APAC, North America, Europe, Middle East, South America) - Global Forecast to 2026." https://www.researchandmarkets.com/reports/4040498/global-activated-carbon-market-by-type.

Alhamed, Y. A. 2006. "Activated Carbon from Date Stone by ZnCl2 Activation." *Journal of King Aabululaziz University: Engineering Sciences* 17(2):7–100. https://www.researchgate.net/publication/237660856_Activated_Carbon_from_Date_Stone_by_ZnCl2_Activation.

Al-Qodah, Z. and R. Shawabkah. 2009. "Production and characterization of granular activated carbon from activated sludge." *Brazilian Journal of Chemical Engineering* 26(1):127–136. https://doi.org/10.1590/S0104-66322009000100012.

Aspentech. 2019. "Aspen Plus V11 Help." Aspen Plus V11.

Aspentech. 2018. "Aspen Plus Methanol Synthesis Model." Aspen Plus V11.

ASTM International. 2016. Standard Terminology of Coal and Coke.

Baffes, J. and W. C. Koh. 2022. "Fertilizer prices expected to remain higher for longer." *World Bank*. Last modified on May 11, 2022. Available from: https://blogs.worldbank.org/opendata/fertilizer-prices-expected-remain-higher-longer.

Bałys, M., E. Brodawka, A Korzeniewska, J. Szczurowski, and K. Zarębska. 2021. "LCA and economic study on the local oxygen supply in Central Europe during the COVID-19 pandemic." *Science of The Total Environment* 786:147401. https://doi.org/10.1016/j.scitotenv.2021.147401.

Banivaheb S., H. Hashemipour. 2017. "Investigation on effects of operating conditions in combined activation of char to develop the pore structure." *Research on Chemical Intermediates* 43(3):1513–1527. https://link.springer.com/article/10.1007/s11164-016-2712-7.

Business Analytiq. 2023a. *Activated carbon prices* [Online]. Available: https://businessanalytiq.com/procurementanalytics/index/activated-carbon-prices/.

Business Analytiq. 2023b. *Ammonia price index* [Online]. Available: https://businessanalytiq.com/procurementanalytics/index/ammonia-price-index/.

Business Analytiq. 2023c. *Formic acid price index* [Online]. Available: https://businessanalytiq.com/procurementanalytics/index/formic-acid-price-index/.

Business Analytiq. 2023d. *Urea price index* Online. Available: https://businessanalytiq.com/procurementanalytics/index/urea-price-index/ChemAnalyst. Decode the Future of Formic Acid.

Baker, F. S., C. E. Miller, A. J. Repik, and E. D. Tolles. 2000. "Activated Carbon." in *Kirk-Othmer Encyclopedia of Chemical Technology*.

Bałys, M., E. Brodawka, A. Korzeniewska, J. Szczurowski, and K. Zarębska. 2021. "LCA and economic study on the local oxygen supply in Central Europe during the COVID-19 pandemic." *Science of the Total Environment* 786:147401.

Benson, S. A., J. D. Laumb, C. R. Crocker, and J. H. Pavlish. 2005. "SCR catalyst performance in flue gases derived from subbituminous and lignite coals." *Fuel processing technology* 86(5):577–613.

Bock, J., M. Hocquel, S. Unterberger, and K. Hein. 2003. "Mercury oxidation across SCR catalysts of flue gas with varying HCl concentrations," presented in *US Environmental Protection Agency-Department of Energy-EPRI Combined Power Plant Air Pollutant Control Symposium* 19–20.

Calkins, W. H. 1986. "Investigation of organic sulfur-containing structures in coal by flash pyrolysis experiments." *Energy & Fuels* 1:59–64. https://pubs.acs.org/doi/pdf/10.1021/ef00001a011.

ChemAnalyst. n.d. "Formic Acid Price Trend and Forecast." *ChemAnalyst.* Accessed March 31, 2023. https://www.chemanalyst.com/Pricing-data/formic-acid-1242#:~:text=In%20USA%2C%20the%20price%20of%20Formic%20Acid%20in%20March%20was,USD%20878%2Fton%20Del%20Texas.&text=In%20Q1%202022%2C%20the%20price,the%20quarter%20in%20Asian%20market.

Chen, X., X. Ge, X. Zhang, and C. Qian. 2015. "Preparation of Activated Carbon from the Residue of Plasma Pyrolysis of Coal by Steam Activation." *Energy Sources, Part A: Recovery, Utilization, and Environmental Effects* 37(4). https://doi.org/10.1080/15567036.2011.586979.

Choy, K. K., J. P. Barford, and G. McKay. 2005. “Production of activated carbon from bamboo scaffolding waste—process design, evaluation and sensitivity analysis.” *Chemical Engineering Journal* 109(1–3):147–165.

Chuang, C. 2020. “Moving the Coal Through a Coal-Fired Power Plant.” *Thermofisher Scientific*. Accessed December 14, 2024. https://www.thermofisher.com/blog/mining/moving-the-coal-through-a-coal-fired-power-plant/.

Clark, P., M. Shields, M. Huang, N. Dowling, and D. Cicerone. 2015. “Liquid sulphur degassing: fundamentals and new technology development in sulphur recovery.” *Brimstone STS Limited* 1–20.

Cuhadaroglu D. and O. A. Uygun. 2008. “Production and characterization of activated carbon from a bituminous coal by chemical activation.” *African Journal Biotechnology* 7(20):3703–3710. DOI: 10.5897/AJB08.588.

Dalai, A. K. and R. Azargohar. 2007. “Production of Activated Carbon from Biochar Using Chemical and Physical Activation: Mechanism and Modeling.” ACS Symposium series. Washington DC, 2007. Chapter 29. https://doi.org/10.1021/bk-2007-0954.ch029.

Environmental Protection Agency. 2022. “Oxygen Supply Chain – Executive Summary.”

Eppinger, J. R., and K.-W. Huang. 2017. “Formic acid as a hydrogen energy carrier.” *ACS Energy Letters* 2(1):188–195.

Eswaran, S., and H. G. Stenger. 2005. “Understanding mercury conversion in selective catalytic reduction (SCR) catalysts.” *Energy & Fuels* 19(6):2328–2334.

Fact.MR. 2023. “Activated Carbon Market Analysis.” Accessed March 31, 2023. https://www.factmr.com/report/5342/activated-carbon-market#:~:text=What%20is%20the%20Global%20Activated,US%24%203.3%20billion%20in%202023.

Federal Reserve Bank of St. Louis. 2023. “Producer Price Index by Industry: Industrial Gas Manufacturing: Oxygen.” [Online]. Available: https://fred.stlouisfed.org/series/PCU325120325120A#0

Fletcher, T. H. 1993. “Swelling properties of coal chars during rapid pyrolysis and combustion.” *Fuel* 72(11)”1485–1495. https://doi.org/10.1016/0016-2361(93)90005-M.

Fletcher, T. H. and D. R. Hardesty. 1992. “Compilation of Sandia coal devolatilization data: milestone report.” Sandia National Laboratory. https://www.osti.gov/biblio/10156500.

Fletcher, T. H. and R. J. Pugmire. 2020. “Chemical Percolation for Coal Devolatilization.” *CPD Model Fortran Codes.* Accessed March 31, 2023. https://www.et.byu.edu/~tom/cpd/cpd.html.

Future Market Insights. 2022. Industrial Oxygen Market Outlook from 2023 to 2033. [Online]. Available: https://www.futuremarketinsights.com/reports/industrial-oxygen-market.

Galbreath, K. C. and C. J. Zygarlicke. 2000. “Mercury transformations in coal combustion flue gas.” *Fuel Processing Technology* 65:289–310.

Gatti et al. 2014. "Review, modeling, Heat Integration, and improved schemes of Rectisol-based processes for CO_2 capture." *Applied Thermal Engineering* 70(2)"1123–1140. https://doi.org/10.1016/j.applthermaleng.2014.05.001.

Ghahraloud, H., M. Farsi, and M. Rahimpour. 2017. "Modeling and optimization of an industrial Claus process: Thermal and catalytic section." *Journal of the Taiwan Institute of Chemical Engineers* 76:1–9.

Giraldo, L. and J. C. Moreno-Pirajan. 2012. "Synthesis of Activated Carbon Mesoporous from Coffee Waste and Its Application in Adsorption Zinc and Mercury Ions from Aqueous Solution." *Journal of Chemistry* 9(2):938–948. https://doi.org/10.1155/2012/120763.

Girgis B. S., S. S. Yunis, and A. M. Soliman. 2002. "Characteristics of activated carbon from peanut hulls in relation to conditions of preparation." *Materials Letters* 57(1):164–172. https://doi.org/10.1016/S0167-577X(02)00724-3.

Global Activated Carbon Market (GACM). 2023. "Activated Carbon Market - Growth, Trends, COVID-19 Impact, and Forecasts (2023-2028)." Report ID#4520008, Mordor Intelligence. https://www.researchandmarkets.com/research/mphk28/global_activated?w=4.

GlobeNewswire. 2019. "Global Demand for Industrial Oxygen Likely to Rise at 6% CAGR through 2029 – Future Market Insights" [Online]. Available: https://www.globenewswire.com/news-release/2019/08/22/1905632/0/en/Global-Demand-for-Industrial-Oxygen-Likely-to-Rise-%20at-6-CAGR-through-2029-Future-Market-Insights.html.

Gutberlet, H., A. Schlueter, and A. Licata. 2000. "SCR Impacts on Mercury Emissions from Coal-Fired Boilers In Electric Power Research Institute SCR Workshop." *Memphis, TN.*

Graaf, G. H., E. J. Stamhuis, and A. A. C. M. Beenackers. 1988. "Knetics of low-pressure methanol synthesis." *Chemical Engineering Science* 43(12):3185–3195. https://doi.org/10.1016/0009-2509(88)85127-3.

Graaf, G. H., H. Scholtens, E. J. Atamhuis, and A. A. C. M. Beenackers. 1990. "Intra-particle diffusion limitations in low-pressure methanol synthesis." *Chemical Engineering Science* 45(4):773–783. https://doi.org/10.1016/0009-2509(90)85001-T.

Graaf, G. H., P. J. J. M. Sijtsema, E. J. Stamhuis, and G. E. H. Joosten. 1986. "Chemical equilibrium in methanol synthesis." *Chemical Engineering Science* 41(11)"2883–2890. https://doi.org/10.1016/0009-2509(86)80019-7.

Hall, B., P. Schager, and O. Lindqvist. 1991. "Chemical reactions of mercury in combustion flue gases." *Water Air & Soil Pollution* 56:3–14.

Hambly, E. M. 1998. "The Chemical Structure of Coal Tar and Char During Devolatilization, Thesis." https://www.et.byu.edu/~tom/Papers/Hambly_Thesis.pdf.

Hanak, D. P., C. Biliyok, and V. Manovic. 2015. "Evaluation and modeling of part-load performance of coal-fired power plant with postcombustion CO_2 capture." *Energy & Fuels* 29(6):3833–3844.

Hayashi J., A. Kazehaya, K. Muroyama, and A. P. Watkinson. 2000. “Preparation of activated carbon from lignin by chemical activation.” *Carbon* 38(13):1873–1878. https://doi.org/10.1016/S0008-6223(00)00027-0.

He, S., J. Zhou, Y. Zhu, Z. Luo, M. Ni, and K. Cen. 2009. “Mercury oxidation over a vanadia-based selective catalytic reduction catalyst.” *Energy & Fuels* 23(1):253–259.

He, X., H. Zhu, Y. Huo, and W. Wang. 2021. “Study on the formation mechanism of the pyrolysis products of lignite at different temperatures based on ReaxFF-MD.” *ACS omega* 6(51):35572–35583.

Hedström, J. 2014. “Simulation and Assessment of Carbon Capture Processes Applied to a Pulp Mill.” Master Thesis Chalmers University of Technology, Gothenburg, Sweden. https://publications.lib.chalmers.se/records/fulltext/200034/200034.pdf.

Hietala, J., A. Vuori, P. Johnsson, I. Pollari, W. Reutemann, and H. Kieczka (eds.). 2016. *Formic acid.* Hoboken, NJ: Wiley-VCH Verlag GmbH & Co.

Ho Y-S., R. Malaryvizhi, and N. Sulochana. 2009. “Equilibrium Isotherm Studies of Methylene Blue Adsorption onto Activated Carbon Prepared from Delonix Regia Pods.” *Journal of Environmental Protection Science* 3:111–6. https://aes.asia.edu.tw/Issues/JEPS2009/JEPS2009.htm.

Hocquel, M. 2004. “The behaviour and fate of mercury in coal-fired power plants with downstream air pollution control devices.”

Hu, Z. and M. P. Srinivasan. 2001. “Mesoporous high surface area activated carbon.” *Microporous and Mesoporous Materials* 43(3):267–275. https://doi.org/10.1016/S1387-1811(00)00355-3.

Hu, Y. and H. Cheng, H. 2016. “Control of mercury emissions from stationary coal combustion sources in China: Current status and recommendations.” *Environmental Pollution* 218:1209–1221.

IBISWorld. n.d. “Industry Market Research, Reports, and Statistics.” Accessed March 31, 2023. https://www.ibisworld.com/industry-statistics/market-size/activated-carbon-manufacturing-united-states.

IBIS World. 2023. “Oxygen & Hydrogen Gas Manufacturing in the US - Market Size, Industry Analysis, Trends and Forecasts (2023-2028)” [Online]. Available: https://www.ibisworld.com/united-states/market-research-reports/oxygen-hydrogen-gas-manufacturing-industry/#IndustryStatisticsAndTrends

Idaho National Laboratory. 2010. “Nuclear-Integrated Methanol-to Gasoline Production Analysis.” TEV-667, Rev 1, Idaho National Laboratory.

Idaho National Laboratory. 2012. “Nuclear-Integrated Methanol-to-Olefins Production Analysis.” TEV-1567, Rev 0, Idaho National Laboratory.

Idris S., Y. A. Iyaka, B. E. N. Dauda, M. M. Ndamitso, and M. T. Umar. 2012. “Kinetic Study of Utilizing Groundnut Shell as an Adsorbent in Removing Chromium and Nickel from Dye Effluent.” *American Chemical Science Journal* 2(1):12–24.

IndexBox Inc. 2023. “Activated Carbon Price per Ton June 2022.” IndexBox Inc. https://www.indexbox.io/blog/activated-carbon-price-per-ton-june-

2022/#:~:text=In%20June%202022%2C%20the%20activated,8.4%25%20against%20the%20previous%20month.

International Energy Agency (IEA). 2021. "Ammonia Technology Roadmap CC BY-NC 3.0 IGO." https://iea.blob.core.windows.net/assets/6ee41bb9-8e81-4b64-8701-2acc064ff6e4/AmmoniaTechnologyRoadmap.pdf.

Intratec Solutions. n.d. "Oxygen Prices - Historical & Forecast Data in Several Countries." Intratec.us. Accessed March 31, 2023. https://www.intratec.us/chemical-markets/oxygen-price.

Intratec. 2023. "Oxygen Price | Current and Forecast." [Online]. Available: https://www.intratec.us/chemical-markets/oxygen-price.

Kumar, D. and D. Kumar. 2018. *Sustainable management of coal preparation.* Woodhead Publishing.

Intratec.us., LLC. 2023. "Activated Carbon Price Monitor Activated Carbon Prices by Country." Accessed March 31, 2023. https://www.intratec.us/chemical-markets/activated-carbon-price.

Pérez-Fortes, M., Schöneberger, J., Boulamanti, A., Harrison, G., Tzimas, E. 2016. "Formic acid synthesis using CO2 as raw material: Techno-economic and environmental evaluation and market potential." *International Journal of Hydrogen Energy*. 41(37):16444–16462. https://doi.org/10.1016/j.ijhydene.2016.05.199.

Portha, J-F., K. Parkhomenko, K. Kobl, A-C. Roger, S. Arab, J-M. Commenge, and L. Falk. 2017. "Kinetics of Methanol Synthesis from Carbon Dioxide Hydrogenation over Copper–Zinc Oxide Catalysts." *Industrial & Engineering Chemistry Research* 56(45):13133–13145. https://doi.org/10.1021/acs.iecr.7b01323.

Jones, S. B., et al. 2009. "Production of Gasoline and Diesel from Bimoass via Fast Pyrolysis, Hydrotreating and Hydrocracking: A Design Case." PNNL-18284, Rev. 1, Pacific Northwest National Laboratory.

Jun T. Y., S. D. Arumugam, N. Hidayah, A. M. Abdullah, and P. A. Latif. 2010. "Effect of activation temperature and heating duration on physical characteristics of activated carbon prepared from agriculture waste." *Environment Asia* 3:143–8. http://dx.doi.org/10.14456/ea.2010.53.

Klier, K., V. Chatikavanij, R. G., Herman, and G. W. Simmons.1982. "Catalytic synthesis of methanol from COH_2: IV. The effects of carbon dioxide." *Journal of Catalysis* 74:343. https://doi.org/10.1016/0021-9517(82)90040-9.

Lee, C. W., R. K. Srivastava, S. B. Ghorishi, T. W. Hastings, and F. M. Stevens. n.d. "Study of speciation of mercury under simulated SCR NOx emission control conditions." Presented in: *Combined Power Plant Air Pollutant Control Mega Symposium, Washington, DC*.

Lee, C. W., R. K. Srivastava, S. B. Ghorishi, T. W. Hastings, and F. M. Stevens. 2004. "Investigation of selective catalytic reduction impact on mercury speciation under simulated NOx emission control conditions." *Journal of the Air & Waste Management Association* 54(12):1560–1566.

Li, W., K. Yang, J. Peng, L. Zhang. S. Guo, and H. Xia. 2008. "Effects of carbonization temperatures on characteristics of porosity in coconut shell chars and activated carbons derived from carbonized coconut shell chars." *Industrial Crops and Products* 28(2):190–198. https://doi.org/10.1016/j.indcrop.2008.02.012.

Li, Y., J. Yu, Y. Liu, R. Huang, Z. Wang, and Y. Zhao, Y. 2022. "A review on removal of mercury from flue gas utilizing existing air pollutant control devices (APCDs)." *Journal of Hazardous Materials* 427:128132.

Lindberg, S. A., W. and Stratton. 1998. "Atmospheric mercury speciation: Concentrations and behavior of reactive gaseous mercury in ambient air." *Environmental Science & Technology* 32(1):49–57.

Liu, S., H. Hao, W. Jia, Y. Cao, and C. Chen. 2020. "Effects of ultralow-emission retrofitting on mercury emission from a coal-fired power plant." *Energy & Fuels* 34(6):7502–7508.

Machalek, T., M. Ramavajjala, M. Richardson, C. Richardson, C. Dene, B. Goeckner, et al. 2003. "Pilot evaluation of flue gas mercury reactions across an SCR unit." Presented in: *Department of Energy-Electric Power Plant Research Institutes U. S. Environmental Protection Agencys Air and Waste Management Association Combined Power Plant Air Pollution Control Symposium*), 19–22.

Martin Gullon, I., M. Asensio, R. Font, and A. Marcilla. 1996. "Steam-activated carbons from a bituminous coal in a continuous multistage fluidized bed pilot plant." *Carbon* 34(12):1515–1520. https://doi.org/10.1016/S0008-6223(96)00106-6.

McDougall, G. J. 1991. "The physical nature and manufacture of activated carbon." *Journal of the Southern African Institute of Mining and Metallurgy* 91(4):109–120. https://journals.co.za/doi/pdf/10.10520/AJA0038223X_2042.

Meessen, J. H. 2012. "Urea." Ullmann's Encyclopedia of Industrial Chemistry. Weinheim: Wiley-VCH. doi:10.1002/14356007.a27_333.pub2.

Miller, B. G. and D. A. Tillman. 1998. "Coal Characteristics." *Combustion Engineering Issues for Solid Fuel Systems* 33–82. https://doi.org/10.1016/B978-0-12-373611-6.00002-1.

Mordor Intelligence. 2023. "Activated Carbon Market - Growth, Trends, Covid-19 Impact, and Forecasts (2023 - 2028)." Accessed March 31, 2023. https://www.mordorintelligence.com/industry-reports/activated-carbon-market.

Mordor Intelligence. 2023. "Activated Carbon Market Size & Share Analysis - Growth Trends & Forecasts (2023 - 2028)." [Online]. Available: https://www.mordorintelligence.com/industry-reports/activated-carbon-market.

Nandiyanto, A. B. D. 2018. "Cost analysis and economic evaluation for the fabrication of activated carbon and silica particles from rice straw waste." *Journal of Engineering Science and Technology* 13(6):1523–1539.

Morsi, B. I. et al. 1992. "Coal surface control for advanced physical fine coal cleaning technologies." (DOE contract No. DE-AC22-88C88877). https://doi.org/10.2172/10123701.

National Energy Technology Laboratory. n.d. "3.1. Commercial Technologies for Oxygen Production." [Online]. Available: https://netl.doe.gov/research/Coal/energy-systems/gasification/gasifipedia/commercial-oxygen.

Ng, C., W. E. Marshall, R. M. Rao, R. R. Bansode, and J. N. Losso. 2003. "Activated carbon from pecan shell: process description and economic analysis." *Industrial Crops and Products* 17(3):209–217.

Niksa, S. and N. Fujiwara. 2005. "A predictive mechanism for mercury oxidation on selective catalytic reduction catalysts under coal-derived flue gas." *Journal of the Air & Waste Management Association* 55(12):1866–1875.

Niksa, S., C. V. Naik, M. S. Berry, and L. Monroe. 2009. "Interpreting enhanced Hg oxidation with Br addition at Plant Miller." *Fuel Processing Technology* 90(11):1372–1377.

Norton, G. A., H. Yang, R. C. Brown, D. L. Laudal, G. E. Dunham, and J. Erjavec. 2003. "Heterogeneous oxidation of mercury in simulated post combustion conditions." *Fuel* 82(2):107–116.

Nutrien. 2022. *Fact Book*, Calgary Canada: Nutrien. https://nutrien-prod-asset.s3.us-east-2.amazonaws.com/s3fs-public/uploads/2022-06/Nutrien%202022%20Fact%20Book.pdf.

O'Brien, B. H. 2014. "Biomass/Coal to Methanol and Methanol to Gasoline Process Model." INL/LTD-14-31818, TEV-2132, Idaho National Laboratory.

Observatory of Economic Complexity. 2021a. "Activated Carbon." [Online]. Available: https://next.oec.world/en/profile/hs/activated-carbon#latest-data

Observatory of Economic Complexity. 2021b. "Ammonia." [Online]. Available: https://next.oec.world/en/profile/hs/ammonia.

Observatory of Economic Complexity. 2021c. "Formic Acid." [Online]. Available: https://oec.world/en/profile/hs/formic-acid.

Observatory of Economic Complexity. 2021d. "Urea." [Online]. Available: https://next.oec.world/en/profile/hs/urea-including-aqueous-solution-in-packs-10-kg.

Pavlish, J. H., E. A. Sondreal, M. D. Mann, E. S. Olson, K. C. Galbreath, and D. L. Laudal. 2003. "Status review of mercury control options for coal-fired power plants." *Fuel Processing Technology* 82(2–3):89–165.

Oh, M. S., A. K. Burnham, and R. W. Crawford. 1988. "Evolution of sulfur gases during coal pyrolysis." In American chemical society meeting. Toronto, Canada. https://www.osti.gov/biblio/5178960.

Park, N., M.-J. Park, Y.-J. Lee, K.-S. Ha, and K.-W. Jun. 2014. "Kinetic modeling of methanol synthesis over commercial catalysts based on three-site adsorption." *Fuel Processing Technology* 125:139–147. https://doi.org/10.1016/j.fuproc.2014.03.041.

Pauls, J. H. 2015. "Simulation of Air-Steam Gasification of Woody Biomass in Aspen Plus: A Comprehensive Model Including Pyrolysis, Hydrodynamics, and Tar Production." Master Thesis University of Calgary. https://prism.ucalgary.ca/server/api/core/bitstreams/4703ecc9-f03b-43a5-a81b-910909cd4a29/content.

Penn State College of Earth and Mineral Sciences Energy Institute. 2022. "The Penn State Coal Sample Bank." energy.psu.edu/sites/www.energy.psu.edu/files/documents/2022_psu_argonne_brochure.pdf.

Perry, S. T., E. M. Hambly, T. H. Fletcher, M. S. Solum and R. J. Pugmire. 2000. "Solid-State ^{13}C NMR characterization of matched tars and chars from rapid coal devolatilization." *Proceedings of the Combustion Institute* Volume 28(2):2313–2319. https://doi.org/10.1016/S0082-0784(00)80642-6.

Polansek, T., and A. Mano. 2022. "As sanctions bite Russia, fertilizer shortage imperils world food supply." Reuters. Thomson Reuters. https://www.reuters.com/business/sanctions-bite-russia-fertilizer-shortage-imperils-world-food-supply-2022-03-23.

Porada S., G. Czerski, P. Grzywacz, D. Makowska, and T. Dziok. 2017. "Comparison of the gasification of coals and their chars with CO_2 based on the formation kinetics of gaseous products." *Thermochimica Acta* 653:97–105. https://doi.org/10.1016/j.tca.2017.04.007.

Richardson, C., T. Machalek, S. Miller, C. Dene, and R. Chang. 2002. "Effect of NOx control processes on mercury speciation in utility flue gas." *Journal of the Air & Waste Management Association* 52(8):941–947.

Rowan, S. L., et al., 2014. "Experimental investigation of char generated from co-pyrolysis of coal and Appalachian hardwoods." *Fuel Processing Technology* 128:354–358. https://reader.elsevier.com/reader/sd/pii/S0378382014003348?token=97F64369A712A3F8F65514BEE27051889964F67A3D2E04EF275F75BA46A623F84C7FE48FCE3DC1A509BCA3A6B336955E&originRegion=us-east-1&originCreation=20230414161456.

Senior, C. L., J. J. Helble, and A. F. Sarofim. 2000. "Emissions of mercury, trace elements, and fine particles from stationary combustion sources." *Fuel Processing Technology* 65:263–288.

Sinha, R., and P. Walker Jr. 1972. "Removal of mercury by sulfurized carbons." *Carbon* 10(6):754–756.

Skrzypek, J., M. Lachowska, and H. Moroz. 1991. "Kinetics of Methanol synthesis over commercial copper/zinc oxide alumina catalysts." *Chemical Engineering Science* 46(11):2809–2813 https://doi.org/10.1016/0009-2509(91)85150-V.

Statista. 2023a. "Ammonia industries worldwide." Available: https://www.statista.com/study/140674/global-ammonia-industry/

Statista. 2023b. "Global industrial gas industry." Available: https://www.statista.com/study/57934/industrial-gases-industry-worldwide/

Statista. 2023c. "Net summer capacity of utility-scale coal-fired power plants in the United States as of 2023, by state." [Online]. Available: https://www.statista.com/statistics/1252480/us-coal-power-capacity-by-state/

Statista and AgileIntel Research. 2023. "Market volume of activated carbon worldwide from 2015 to 2022, with a forecast for 2023 to 2030 (in million metric tons)." Available: https://www.statista.com/statistics/963555/global-market-volume-activated-carbon/

Sung, J.-H., S.-K. Back, B.-M. Jung, Y.-S. Kang, C.-G. Lee, and H.-N. Jang. 2017. "Speciation and capture performance of mercury by a hybrid filter in a coal-fired power plant." *International Journal of Coal Geology* 170:35–40.

Sudaryanto, Y., S. B. Hartono, W. Irawaty, H. Hindarso, and S. Ismadji. 2006. "High surface area activated carbon prepared from cassava peel by chemical activation." *Bioresource Technology* 97(5):734–39. https://doi.org/10.1016/j.biortech.2005.04.029.

Sultana A. and M. T. Reza. 2022. "Techno-economic assessment of superactivated hydrochar production by KOH impregnation compared to direct chemical activation." *Biomass Conversion and Biorefinery* Early Access. DOI 10.1007/s13399-022-02364-w.

Sun, L and R. Smith. 2013 "Rectisol wash process simulation and analysis." *Journal of Cleaner Production* 39:321–328. https://doi.org/10.1016/j.jclepro.2012.05.049.

Sutcu, H. 2021. "Production and characterization of activated carbons from Rhododendron ponticum L. by physical and chemical activation." *Biomass Conversion and Biorefinery* 11(4):1335–1341. https://doi.org/10.1007/s13399-019-00485-3.

Teng, H., J.-A. Ho, and Y.-F. Hsu. 1997. "Preparation of activated carbons from bituminous coals with CO_2 activation—influence of coal oxidation." *Carbon* 35(2):275–283.

Tewalt, S. J., L. J. Bragg, and R. B. Finkelman. Mercury in US Coal--Abundance, Distribution, and Modes of Occurrence. https://pubs.usgs.gov/fs/fs095-01/fs095-01.html#:~:text=Because%20of%20the%20low%20concentrations,the%20coal%20is%20compacted%20(fig.

Thomas Publishing Company. 2023. "Top Manufacturers and Suppliers of Oxygen in the USA." Thomas Publishing Company. Accessed March 31, 2023. https://www.thomasnet.com/articles/top-suppliers/oxygen-suppliers-companies/.

Thongpat, W., J. Taweekun, and K. Maliwan. 2021. "Synthesis and characterization of microporous activated carbon from rubberwood by chemical activation with KOH." Carbon Letters. Vol 31, Issue 5, 1079–1088.

Travis, C. C., and B. P. Blaylock. 1995. "Municipal waste combustor emissions: Human exposure to mercury and dioxin." *Toxicological & Environmental Chemistry* 49(3):203–216.

Tullo, A. H. 2021. "Is ammonia the fuel of the future?" *Chemical & Engineering News*. https://cen.acs.org/business/petrochemicals/ammonia-fuel-future/99/i8.

U.S. Bureau of Labor Statistics. 2023a. "Producer Price Index by Commodity: Chemicals and Allied Products: Oxygen [WPU06790304]." Retrieved from FRED, Federal Reserve Bank of St. Louis; April 2, 2023. https://fred.stlouisfed.org/series/WPU06790304.

U.S. Bureau of Labor Statistics. 2023b. "Producer Price Index by Industry: Nitrogenous Fertilizer Manufacturing: Synthetic Ammonia, Nitric Acid, Ammonium Compounds, and Urea [PCU325311325311A]." Retrieved from FRED, Federal Reserve Bank of St. Louis. https://fred.stlouisfed.org/series/PCU325311325311A.

United States Department of Energy. 2022. "DOE National Clean Hydrogen Strategy and Roadmap." https://www.hydrogen.energy.gov/pdfs/clean-hydrogen-strategy-roadmap.pdf.

Vanden Bussche, K. M. and G. F. Froment. 1996. "A Steady-State Kinetic Model for Methanol Synthesis and the Water Gas Shift Reaction on a Commercial Cu/ZnO/Al_2O_3Catalyst." *Journal of Catalysis* 161(1):1–10. https://doi.org/10.1006/jcat.1996.0156.

Villa, P., P. Forzatti, G. Buzzi-Ferraris, G. Garone, and I. Pasquon. 1985. "Synthesis of alcohols from carbon oxides and hydrogen. 1. Kinetics of the low-pressure methanol synthesis." *Industrial & Engineering Chemistry, Process Design and Development*. 24(1):12–19. https://doi.org/10.1021/i200028a003.

Vorres, K. S. 1990. "The Argonne Premium Coal Sample Program." *Energy & Fuels* 4(5):420–426. https://pubs.acs.org/doi/10.1021/ef00023a001.

Wang, S., L. Zhang, G. Li, Y. Wu, J. Hao, N. Pirrone, et al. 2010. "Mercury emission and speciation of coal-fired power plants in China." *Atmospheric Chemistry and Physics* 10(3):1183–1192.

Watt, M. 1996. "The Chemical Structure of Coal Tar and Char During Devolatilization, Thesis." https://www.et.byu.edu/~tom/Papers/Watt_thesis.pdf.

Wendt, D. S., Knighton, L.T., Boardman, R. D. "High Temperature Steam Electrolysis Process Performance and Cost Estimates." INL/RPT-22-66117, Idaho National Laboratory. https://inldigitallibrary.inl.gov/sites/sti/sti/Sort_60759.pdf.

Worsham, E. K. 2022. "Carbon Conversion Product Pathways with Nuclear Power Plant Integration." INL/RPT-22-69229, Idaho National Laboratory. https://www.osti.gov/biblio/1963875.

Wu, Y., W. Chang, M. Millan, and Y. Hao. 2023. "Synergetic removal characteristics of mercury for ultra-low emission coal-fired power plant." *Fuel* 332:126083.

Xiong, J., H. Zhao, M. Chen, and C. Zheng. 2011. "Simulation study of an 800 MWe oxy-combustion pulverized-coal-fired power plant." *Energy & Fuels* 25(5):2405–2415.

Yacob, A. R., Z. A. Majid, R. S. D. Dasril, and V. Inderan. 2008. "Comparison of various sources of high surface area carbon prepared by different types of activation." *Malaysian Journal of Analytical Science* 12(1):264–271. https://www.researchgate.net/publication/237351236_Comparison_of_various_sources_of_high_surface_area_carbon_prepared_by_different_types_of_activation.

Yahya, M. A., Z. Al-Qodah, and C. W. Z. Ngah. 2015 "Agricultural bio-waste materials as potential sustainable precursors used for activated carbon production: A review." *Renewable and Sustainable Energy Reviews* 46:218–235. https://doi.org/10.1016/j.rser.2015.02.051.

Yang, C., S. Wang, J. Yang, D. Xu, Y. Li, and J. Li. 2020. "Hydrothermal liquefaction and gasification of biomass and model compounds: a review." *Green Chemistry* 22(23):8210–8232.

Yang, Y., J. Liu, Z. Wang, and Z. Zhang. 2017. "Homogeneous and heterogeneous reaction mechanisms and kinetics of mercury oxidation in coal-fired flue gas with bromine addition." *Proceedings of the Combustion Institute* 36(3):4039–4049.

Yegaheh, M. M., T. Kaghazchi, and M. Soleimani. 2006. "Effect of Raw Materials on Properties of Activated Carbons." *Chemical Engineering Technology* 29(10):1247–1251. https://doi.org/10.1002/ceat.200500298.

Yue-yang, X., X. Jian-ming, W. Hongliang, L. Bing, G. Yiming, and L. Jun. 2014. "Research on mercury collaborative control by conventional pollutants purification facilities of coal-fired power plants." *Proceedings CSEE* 34(23):3924–3931.

Zhang, L., S. Wang, Q. Wu, F. Wang, C.-J. Lin, L. Zhang, et al. 2016. "Mercury transformation and speciation in flue gases from anthropogenic emission sources: a critical review." *Atmospheric Chemistry and Physics* 16(4):2417–2433.

Zhang, Y., J. Yang, X. Yu, P. Sun, Y. Zhao, J. Zhang, et al. 2017. "Migration and emission characteristics of Hg in coal-fired power plant of China with ultra low emission air pollution control devices." *Fuel Processing Technology* 158:272–280.

Zhao, S., Y. Duan, C. Wang, M. Liu, J. Lu, H. Tan, et al. 2017a. "Migration behavior of trace elements at a coal-fired power plant with different boiler loads." *Energy & Fuels* 31(1):747–754.

Zhao, S., Y. Duan, C. Yao, M. Liu, J. Lu, H. Tan, et al. 2017b. "Study on the mercury emission and transformation in an ultra-low emission coal-fired power plant." *Fuel* 199:653–661.

Zhao, S., D. Pudasainee, Y. Duan, R. Gupta, M. Liu, and J. Lu. 2019. "A review on mercury in coal combustion process: Content and occurrence forms in coal, transformation, sampling methods, emission and control technologies." *Progress in Energy and Combustion Science* 73:26–64.

Zheng X., W. Zhou, R. Wan, J. Luo, Y. Su, H. Huang, and Y. Chen. 2018. "Increasing municipal wastewater BNR by using the preferred carbon source derived from kitchen wastewater to enhance phosphorous uptake and short-cut nitrification-denitrification." *Chemical Engineering Journal* 344:556–564. https://doi.org/10.1016/j.cej.2018.03.124.

Zhu Z., A. Li, M. Xia, J. Wan, S. Zhong, F. Liu, and Q. Zhang. 2008. "Preparation and characterization of polymer based spherical activated carbons." *Journal of Applied Polymer Science* 26(5):645–651. https://doi.org/10.1002/app.28304.

Zhuang, Y., C. J. Zygarlicke, K. C. Galbreath, J. S. Thompson, M. J. Holmes, and J. H. Pavlish. 2004. "Kinetic transformation of mercury in coal combustion flue gas in a bench-scale entrained-flow reactor." *Fuel Processing Technology* 85(6–7):463–472.

Appendix A

Aspen Model Results

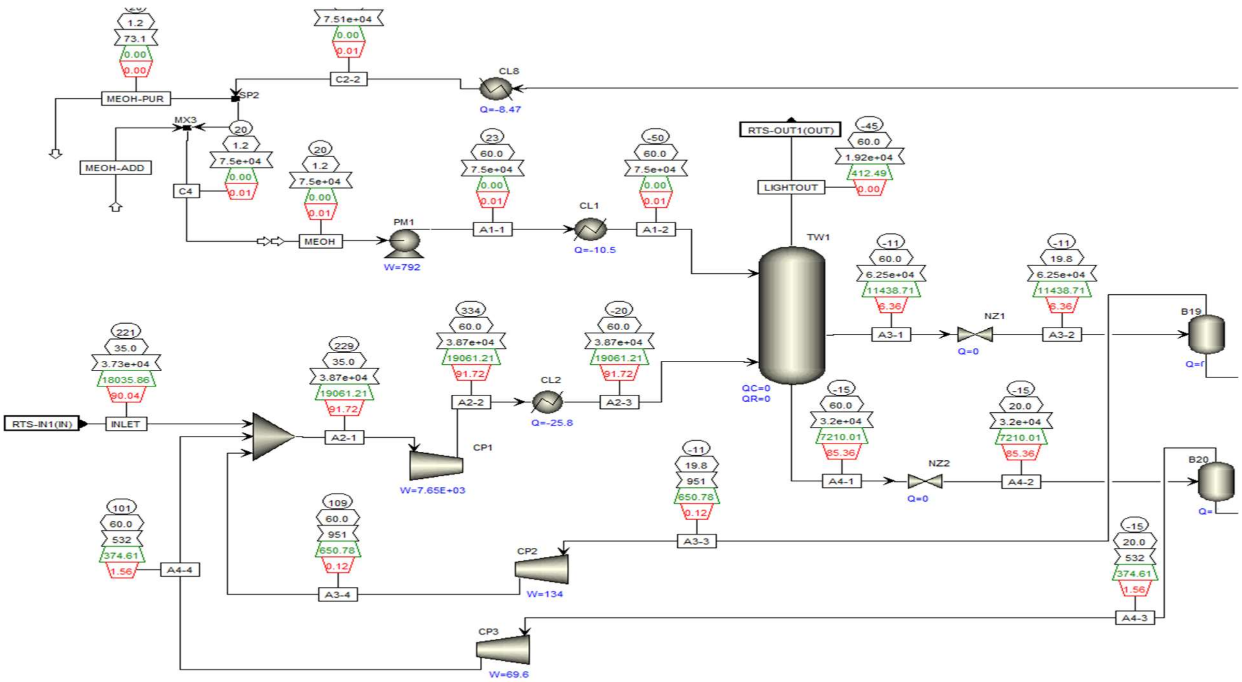

Figure A-1. Mass balance for each stream in the flue gas treatment.

Table A-1. Aspen model results for the first condition evaluated, 150 kg/h of coal and 300 kg/h of steam.

Description	Units	H2O-FEED	STEAM	STEAM4AC	BLOWDOWN	HOT-STEA	COAL	CHAR-4SG	AC	C-4-SG	SYNGAS
From	—	—	HEAT-EX1	STEAMSEP	STEAMSEP	HEAT-EX2	—	RSTOIC	SEP	SEP	RGIBBS
To	—	HEAT-EX1	STEAMSEP	HEAT-EX2	—	RGIBBS	RSTOIC	SEP	—	RGIBBS	—
Stream Class	—	MIXCINC	MIXCINC	MIXCINC	MIXCINC	MIXCINC	MIXCINC	MIXCINC	MIXCINC	MIXCINC	MIXCINC
Temperature	C	25.00	145.00	145.00	145.00	700.00	700.00	700.00	700.00	700.00	700.00
Pressure	bar	1.01	1.01	4.03	4.03	1.01	1.00	1.00	1.00	1.00	1.00
Mass Vapor Fraction	—	0.00	1.00	1.00	0.00	1.00	0.00	0.08	0.00	0.13	0.74
Mass Liquid Fraction	—	1.00	0.00	0.00	1.00	0.00	0.00	0.00	0.00	0.00	0.00
Mass Solid Fraction	—	0.00	0.00	0.00	0.00	0.00	1.00	0.92	1.00	0.87	0.26
Mass Enthalpy	cal/gm	-3829.72	-3152.82	-3155.27	-3690.24	-2876.13	293.88	274.51	123.22	366.38	-1631.05
Mass Density	gm/cc	0.96	0.00	0.00	0.84	0.00	1.53	0.00	2.61	0.00	0.00
Enthalpy Flow	cal/sec	-319142.98	-26734.73	-255051.35	-9225.61	-232486.98	12244.94	11437.94	1939.87	9498.07	-174126.58
Mass Flows	kg/hr	300.00	300.00	291.00	9.00	291.00	150.00	150.00	56.67	93.33	384.33
H2O	kg/hr	300.00	300.00	291.00	9.00	291.00	0.00	0.00	0.00	0.00	116.97

Description	Units	H2O-FEED	STEAM	STEAM4AC	BLOWDOWN	HOT-STEA	COAL	CHAR-4SG	AC	C-4-SG	SYNGAS
COALCHAR	kg/hr	0.00	0.00	0.00	0.00	0.00	150.00	0.00	0.00	0.00	0.00
ASH	kg/hr	0.00	0.00	0.00	0.00	0.00	0.00	24.59	24.59	0.00	0.00
C	kg/hr	0.00	0.00	0.00	0.00	0.00	0.00	108.50	27.12	81.37	0.00
CO	kg/hr	0.00	0.00	0.00	0.00	0.00	0.00	0.00	0.00	0.00	98.68
CO_2	kg/hr	0.00	0.00	0.00	0.00	0.00	0.00	0.00	0.00	0.00	138.18
CH4	kg/hr	0.00	0.00	0.00	0.00	0.00	0.00	0.00	0.00	0.00	1.80
H2	kg/hr	0.00	0.00	0.00	0.00	0.00	0.00	49.95	0.00	4.95	23.97
O2	kg/hr	0.00	0.00	0.00	0.00	0.00	0.00	2.28		2.28	0.00
N2	kg/hr	0.00	0.00	0.00	0.00	0.00	0.00	4.73		4.73	4.72
S	kg/hr	0.00	0.00	0.00	0.00	0.00	0.00	4.97	4.97	0.00	0.00
Mass Fractions	—	—	—	—	—	—	—	—	—	—	—
H2O	—	1.00	1.00	1.00	1.00	1.00	0.00	0.00	0.00	0.00	0.30
COALCHAR	—	0.00	0.00	0.00	0.00	0.00	1.00	0.00	0.00	0.00	0.00
ASH	—	0.00	0.00	0.00	0.00	0.00	0.00	0.16	0.43	0.00	0.00
C	—	0.00	0.00	0.00	0.00	0.00	0.00	0.72	0.48	0.87	0.00
CO	—	0.00	0.00	0.00	0.00	0.00	0.00	0.00	0.00	0.00	0.26
CO_2	—	0.00	0.00	0.00	0.00	0.00	0.00	0.00	0.00	0.00	0.36
CH4	—	0.00	0.00	0.00	0.00	0.00	0.00	0.00	0.00	0.00	0.00
H2	—	0.00	0.00	0.00	0.00	0.00	0.00	0.03	0.00	0.05	0.06
O2	—	0.00	0.00	0.00	0.00	0.00	0.00	0.02	0.00	0.02	0.00
N2	—	0.00	0.00	0.00	0.00	0.00	0.00	0.03	0.00	0.05	0.01
S	—	0.00	0.00	0.00	0.00	0.00	0.00	0.03	0.09	0.00	0.00

Table A-2. Aspen model results for the second condition evaluated, 300 kg/h of coal and 150 kg/h of steam.

Description	Units	H2O-FEED	STEAM	STEAM4AC	BLOWDOWN	HOT-STEA	COAL	CHAR-4SG	AC	C-4-SG	SYNGAS
From	—	—	HEAT-EX1	STEAMSEP	STEAMSEP	HEAT-EX2	—	RSTOIC	SEP	SEP	RGIBBS
To	—	HEAT-EX1	STEAMSEP	HEAT-EX2	—	RGIBBS	RSTOIC	SEP	—	RGIBBS	—
Stream Class	—	MIXCINC	MIXCINC	MIXCINC	MIXCINC	MIXCINC	MIXCINC	MIXCINC	MIXCINC	MIXCINC	MIXCINC
Temperature	C	25.00	145.00	145.00	145.00	700.00	700.00	700.00	700.00	700.00	700.00
Pressure	bar	1.01	1.01	4.03	4.03	1.01	1.00	1.00	1.00	1.00	1.00
Mass Vapor Fraction	—	0.00	1.00	1.00	0.00	1.00	0.00	0.08	0.00	0.13	0.74
Mass Liquid Fraction	—	1.00	0.00	0.00	1.00	0.00	0.00	0.00	0.00	0.00	0.00
Mass Solid Fraction	—	0.00	0.00	0.00	0.00	0.00	1.00	0.92	1.00	0.87	0.26
Mass Enthalpy	cal/gm	-3829.72	-3152.82	-3155.27	-3690.24	-2876.13	293.88	274.51	123.22	366.38	-637.53
Mass Density	gm/cc	0.96	0.00	0.00	0.84	0.00	1.53	0.00	2.61	0.00	0.00
Enthalpy Flow	cal/sec	-159571.49	-131367.36	-127525.67	-4612.80	-116243.49	24489.89	22875.88	3879.74	18996.14	-58821.14
Mass Flows	kg/hr	150.00	150.00	145.50	4.50	145.50	300.00	300.00	113.35	186.65	332.15
H2O	kg/hr	150.00	150.00	145.50	4.50	145.50	0.00	0.00	0.00	0.00	28.77

Description	Units	H2O-FEED	STEAM	STEAM4AC	BLOWDOWN	HOT-STEA	COAL	CHAR-4SG	AC	C-4-SG	SYNGAS
COALCHAR	kg/hr	0.00	0.00	0.00	0.00	0.00	300.00	0.00	0.00	0.00	0.00
ASH	kg/hr	0.00	0.00	0.00	0.00	0.00	0.00	49.17	49.17	0.00	0.00
C	kg/hr	0.00	0.00	0.00	0.00	0.00	0.00	216.99	54.25	162.74	87.34
CO	kg/hr	0.00	0.00	0.00	0.00	0.00	0.00	0.00	0.00	0.00	124.78
CO_2	kg/hr	0.00	0.00	0.00	0.00	0.00	0.00	0.00	0.00	0.00	50.83
CH4	kg/hr	0.00	0.00	0.00	0.00	0.00	0.00	0.00	0.00	0.00	10.72
H2	kg/hr	0.00	0.00	0.00	0.00	0.00	0.00	9.90	0.00	9.90	20.27
O2	kg/hr	0.00	0.00	0.00	0.00	0.00	0.00	4.56	0.00	4.56	0.00
N2	kg/hr	0.00	0.00	0.00	0.00	0.00	0.00	9.45	0.00	9.45	9.45
S	kg/hr	0.00	0.00	0.00	0.00	0.00	0.00	9.93	9.93	0.00	0.00
Mass Fractions	—	—	—	—	—	—	—	—	—	—	—
H2O	—	1.00	1.00	1.00	1.00	1.00	0.00	0.00	0.00	0.00	0.09
COALCHAR	—	0.00	0.00	0.00	0.00	0.00	1.00	0.00	0.00	0.00	0.00
ASH	—	0.00	0.00	0.00	0.00	0.00	0.00	0.16	0.43	0.00	0.00
C	—	0.00	0.00	0.00	0.00	0.00	0.00	0.72	0.48	0.87	0.26
CO	—	0.00	0.00	0.00	0.00	0.00	0.00	0.00	0.00	0.00	0.38
CO_2	—	0.00	0.00	0.00	0.00	0.00	0.00	0.00	0.00	0.00	0.15
CH4	—	0.00	0.00	0.00	0.00	0.00	0.00	0.00	0.00	0.00	0.03
H2	—	0.00	0.00	0.00	0.00	0.00	0.00	0.03	0.00	0.05	0.06
O2	—	0.00	0.00	0.00	0.00	0.00	0.00	0.02	0.00	0.02	0.00
N2	—	0.00	0.00	0.00	0.00	0.00	0.00	0.03	0.00	0.05	0.03
S	—	0.00	0.00	0.00	0.00	0.00	0.00	0.03	0.09	0.00	0.00

Table A-3. Summary table of Claus process.

	Units	ACIDGAS	O2	SULFUR
Stream Class	—	CONVEN	CONVEN	CONVEN
Phase	—	Vapor Phase	Vapor Phase	Liquid Phase
Temperature	C	85.0	32.0	135.0
Pressure	bar	10.0	10.0	10.0
Molar Vapor Fraction	—	1.0	1.0	0.0
Molar Liquid Fraction	—	0.0	0.0	1.0
Molar Solid Fraction	—	0.0	0.0	0.0
Mass Vapor Fraction	—	1.0	1.0	0.0
Mass Liquid Fraction	—	0.0	0.0	1.0
Mass Solid Fraction	—	0.0	0.0	0.0
Molar Enthalpy	cal/mol	-91693.2	49.1	54032.8
Mass Enthalpy	cal/gm	-2093.0	1.5	1704.0
Molar Entropy	cal/mol-K	-1.8	-4.4	40.0
Mass Entropy	cal/gm-K	0.0	-0.1	1.3
Molar Density	mol/cc	0.0	0.0	0.1
Mass Density	gm/cc	0.0	0.0	1.9
Enthalpy Flow	cal/sec	-3475784.3	19.5	27939.4

	Units	ACIDGAS	O2	SULFUR
Average MW	—	43.8	32.0	31.7
Mole Flows	kmol/day	3275.1	34.4	44.7
Mole Fractions				
Mass Flows	tons/day	158.2	1.2	1.6
H2S	tons/day	2.3E+00	0.0E+00	4.0E-04
NH3	tons/day	1.0E-03	0.0E+00	1.4E-06
HCL	tons/day	0.0E+00	0.0E+00	0.0E+00
O2	tons/day	0.0E+00	1.2E+00	0.0E+00
CO_2	tons/day	1.6E+02	0.0E+00	5.0E-02
CH4	tons/day	3.0E-12	0.0E+00	4.2E-16
CO	tons/day	0.0E+00	0.0E+00	4.6E-05
H2	tons/day	0.0E+00	0.0E+00	3.2E-10
H2O	tons/day	3.5E-05	0.0E+00	4.2E-02
COS	tons/day	0.0E+00	0.0E+00	0.0E+00
SO2	tons/day	0.0E+00	0.0E+00	3.4E-03
N2	tons/day	0.0E+00	0.0E+00	8.2E-13
S2	tons/day	0.0E+00	0.0E+00	0.0E+00
S6	tons/day	0.0E+00	0.0E+00	0.0E+00
S8	tons/day	0.0E+00	0.0E+00	9.5E-19
METHA-01	tons/day	1.2E-01	0.0E+00	1.6E-03
C2H4	tons/day	9.4E-07	0.0E+00	3.8E-10
S	tons/day	0.0E+00	0.0E+00	2.2E+00
Mass Fractions				
Volume Flow	l/min	6772.7	60.6	0.5

Appendix B

Reaction Rate Information

B-1. CLAUS PROCESS

Summary of the reactions for the thermal process in this process are disclosed below (Ghahraloud et al. 2017).

$$H_2S \leftrightarrow H_2 + S_2$$
$$H_2S + \frac{3}{2}O_2 \rightarrow SO_2 + H_2O$$
$$H_2S + \frac{1}{2}SO_2 \leftrightarrow H_2O + \frac{3}{4}S_2$$
$$CH_4 + \frac{3}{2}O_2 \rightarrow CO + 2H_2O$$
$$C_2H_6 + \frac{5}{2}O_2 \rightarrow 2CO + 3H_2O$$
$$C_3H_8 + \frac{7}{2}O_2 \rightarrow 3CO + 4H_2O$$
$$C_4H_{10} + \frac{9}{2}O_2 \rightarrow 4CO + 5H_2O$$
$$CO + \frac{1}{2}S_2 \leftrightarrow COS$$
$$CO_2 + H_2 \leftrightarrow CO + H_2O$$
$$CO + H_2S \leftrightarrow COS + H_2$$
$$NH_3 \rightarrow \frac{1}{2}N_2 + \frac{3}{2}H_2$$
$$CH_4 + 2S_2 \rightarrow CS_2 + 2H_2S$$

Within the catalytic reactors, the hydrolysis of CS2 and COS, which are generated in the thermal section, occurs. The catalyst surface serves as the site for the primary and ancillary reactions as follows:

$$2H_2S + SO_2 \leftrightarrow \frac{1}{2}S_6 + 2H_2O$$
$$COS + H_2O \rightarrow CO_2 + H_2S$$
$$CS_2 + 2H_2O \rightarrow CO_2 + 2H_2$$

The rate of the thermal and catalytic reactions is presented Table B-1 and Table B-2 (Ghahraloud et al. 2017).

Table B-1. Rate of thermal reactions.

Reaction	Rate of Reaction
1	$\gamma_{H_2S} = 4.3 \times 10^6 \exp\left(-\frac{26}{RT}\right) C_{H_2} C_{S_2} - 3.6 \times 10^8 \exp\left(-\frac{48}{RT}\right) C_{H_2S}$
2	$\gamma_{H_2S} = 14 \times \exp\left(-\frac{11}{RT}\right) P_{H_2S} P_{O_2}^{1.5}$
3	$\gamma_{H_2S} = 15900 \times \exp\left(-\frac{49.9}{RT}\right) P_{H_2S} P_{SO_2}^{0.5} - 500 \exp\left(-\frac{49.9}{RT}\right) P_{H_2O} P_{S_2}^{0.75}$
4	$\gamma_{CH_4} = 10^{13.2} \times \exp\left(-\frac{48.4}{RT}\right) C_{CH_4}^{0.7} C_{O_2}^{0.8}$
5	$\gamma_{C_2H_6} = 1.3 \times 10^{12} \exp\left(-\frac{30}{RT}\right) C_{C_2H_6}^{0.1} C_{O_2}^{1.65}$
6	$\gamma_{C_3H_8} = 10^{12} \exp\left(-\frac{30}{RT}\right) C_{C_3H_8}^{0.1} C_{O_2}^{1.65}$
7	$\gamma_{C_4H_{10}} = 8.8 \times 10^{11} \exp\left(-\frac{30}{RT}\right) C_{C_4H_{10}}^{0.1} C_{O_2}^{1.65}$
8	$\gamma_{CO} = 3.78 \times 10^5 \exp\left(-\frac{6700}{T}\right) C_{COS} C_{S_2} - 2.05 \times 10^9 \exp\left(-\frac{21630}{T}\right) C_{COS} C_t$
9	$\gamma_{CO_2} = 3.95 \times 10^{10} \exp\left(-\frac{31220}{T}\right) C_{CO_2} C_{H_2}^{0.5}$
10	$\gamma_{CO} = 1.59 \times 10^5 \exp\left(-\frac{13340}{T}\right) C_{CO} C_{H_2S}^{0.5}$
11	$\gamma_{NH_3} = 0.0042 \times \exp\left(-\frac{16.5}{RT}\right) P_{NH_3}^{1.25}$
12	$\gamma_{CH_4} = 5.53 \times 10^{10} \exp\left(-\frac{19320}{T}\right) C_{CH_4} C_{S_2}$

Table B-2. Rate of catalytic reactions.

Reaction	Rate of Reaction
13	$$\gamma_{H_2S} = \frac{-k_s\left(P_{H_2S}P_{SO_2}^{0.5} - \frac{P_{H_2O}P_{S_6}^{0.25}}{K_E}\right)}{\left(1 + K_{H_2O} + P_{H_2O}\right)^2}$$
14	$$\gamma_{COS} = \frac{k_{COS}\left(P_{COS}P_{H_2O}\right)}{\left(1 + K_{H_2O} + P_{H_2O}\right)}$$
15	$$\gamma_{CS_2} = \frac{k_{CS_2}P_{CS_2}P_{H_2O}}{\left(1 + K_{H_2O} + P_{H_2O}\right)}$$
$k_i = k_{0i} exp\left(\frac{-E_i}{RT}\right)$	
$k_{H_2O_i} = k_{H_2O_{0i}} exp\left(\frac{-\Delta H_i}{RT}\right)$	
$k_E = 9.502 \times 10^{-7} exp\left(\frac{1.11 \times 10^4}{T}\right)$	

No	$\boldsymbol{k_{0i}}$	$\boldsymbol{k_{H_2O_i}}$	$\boldsymbol{E_i}$	$\boldsymbol{\Delta H_i}$
13	6.91	0.338	30.77	—
14	19.75	3.43	40.41	98.10
15	2.30	1.25	25.27	83.22

B-2. METHANOL SYNTHESIS

Reaction rate expression for each reaction suggested by Graaf are written as below in Equation 8. Reaction rate is defined as a produced product or consumed reactant in mole per unit time per unit catalyst used. Aspen Plus fixed it in [kmol/sec/kg cat].

$$r_A = \frac{k'_A K_{\mathrm{CO}}\left[f_{CO}f_{H_2}^{1.5} - \frac{f_{CH_3OH}}{f_{H_2}^{0.5}}\frac{1}{K_{p1}}\right]}{\left(1 + K_{CO}f_{CO} + K_{CO_2}f_{CO_2}\right)\left[f_{H_2}^{0.5} + \left(K_{H_2O}/K_{H_2}^{0.5}\right)f_{H_2O}\right]}$$

$$r_B = \frac{k'_B K_{\mathrm{CO_2}}\left[f_{CO_2}f_{H_2} - f_{H_2O}f_{CO}\frac{1}{K_{p2}}\right]}{\left(1 + K_{CO}f_{CO} + K_{CO_2}f_{CO_2}\right)\left[f_{H_2}^{0.5} + \left(K_{H_2O}/K_{H_2}^{0.5}\right)f_{H_2O}\right]}$$

$$r_C = \frac{k'_C K_{\mathrm{CO_2}}\left[f_{CO_2}f_{H_2}^{1.5} - \frac{f_{CH_3OH}f_{H_2O}}{f_{H_2}^{1.5}}\frac{1}{K_{p3}}\right]}{\left(1 + K_{CO}f_{CO} + K_{CO_2}f_{CO_2}\right)\left[f_{H_2}^{0.5} + \left(K_{H_2O}/K_{H_2}^{0.5}\right)f_{H_2O}\right]} \tag{8}$$

where

f_{CO}, f_{CO_2} and f_{H_2O} = fugacity of CO, CO_2, and H_2O, respectively

k'_A, k'_B and k'_C = reaction constant

K_{p1}, K_{p2}, K_{p3} = equilibrium constant for reaction A, B, and C, respectively

$K_{CO}, K_{CO_2}, K_{H_2O}$ and K_{H_2} = equilibrium constant of surface adsorption of each component, CO, CO_2 H_2O, and H_2, respectively.

Fugacity is a measure of chemical potential in the form of adjusted pressure, and can be calculated by the equation of states determined. The reaction constant is expressed as the Arrhenius form, and the equilibrium constant is a function of temperature expressed in Equation 9. Mathematically, both are the same expression

$$k = k_0 \exp(-E_a/RT)$$

$$Ln\,(K) = A - B/T \tag{9}$$

where

k_0 = pre-exponential factor

E_a = s activation energy of the reaction

R = universal constant of 8.314 x 10^{-3} kJ/mol K.

Coefficient used for Graaf model is tabulated in Table B-3.

On the other hand, Van den Bussche and Fremont (1996) explained the mechanism of methanol synthesis that CO is converted to CO_2 via water gas shift reaction, and CO_2 is converted via hydrogenation. In this model, only reaction b and c are considered, and adsorption of each component and reaction occurs at same site of catalysis. Reaction rate is written as below, and their coefficient are tabulated in Table B-4

$$r_B = \frac{k_{bf}\,P_{CO_2} - k_{bb}\frac{P_{CO}P_{H_2O}}{P_{H_2}}}{\left(1+K_{B1}\frac{P_{H_2O}}{P_{H_2}}+K_{B2}P_{H_2}^{0.5}+K_{B3}P_{H_2O}\right)^1}\frac{kmol}{kg_{cat}\cdot sec} \tag{10}$$

$$r_C = \frac{k_{cf}\,P_{CO_2}\,P_{H_2} - k_{cb}\frac{P_{MeOH}\,P_{H_2O}}{P_{H_2}^2}}{\left(1+K_{C1}\frac{P_{H_2O}}{P_{H_2}}+K_{C2}P_{H_2}^{0.5}+K_{C3}P_{H_2O}\right)^3}\frac{kmol}{kg_{cat}\cdot sec} \tag{11}$$

Table B-3. Coefficients for reaction constant and equilibrium constant used in Garr model based in unit of [kmol], [kg cat], [sec], [K], and [Pa].

k'	Dimension	k_0	Ea [kJ/mol]
k'_A	[kmol] $[sec]^{-1}$ $[kg\ cat]^{-1}$ $[Pa]^{-1}$	0.489	113
k'_B	[kmol] $[sec]^{-1}$ $[kg\ cat]^{-1}$ $[Pa]^{-0.5}$	3,060,000	152.9
k'_C	[kmol] $[sec]^{-1}$ $[kg\ cat]^{-1}$ $[Pa]^{-1}$	0.00109	87.5
K	Dimension	Coef.A	Coef.B
K_{p1}	$[Pa]^{-2}$	−52.0867	11,833
K_{p2}	(non-dimensional)	4.6719	−4,773
K_{p3}	$[Pa]^{-2}$	1.3631	7,060
K_{CO}	$[Pa]^{-1}$	−22.2557	5,629
K_{CO_2}	$[Pa]^{-1}$	−25.6779	7,421
$K_{H2O}/K_{H2^{0.5}}$	$[Pa]^{-0.5}$	−20.0229	10,103

Table B-4. Coefficients for reaction constant and equilibrium constant used in Van den Bussche and Froment model based in unit of [kmol], [kg cat], [sec], [K], and [Pa].

	Arrhenius Form	A (ln k_0)	-B (-Ea/R)
Reaction B			
k_{bf}	1.07e-13 exp (+4413.76/T)	−29.8659	4413.76
k_{bb}	4.182e7 exp (−2645.97/T)	17.5489	−2645.97
K_{B1}	3453.38	8.1471	—
K_{B2}	1.578e-3 exp (+2068.44/T)	−6.4516	2068.44
K_{B3}	6.62e-16 exp(+14928.92/T)	−34.9513	14928.92
Reaction C			
k_{cf}	122 exp(−11398.24/T)	4.804	−11398.2
k_{cb}	1.1412 exp(−6624.98/T)	0.1321	6624.98
K_{C1}	3453.38	8.1471	—
K_{C2}	1.578e-3 exp (+2068.44/T)	−6.4516	2068.44
K_{C3}	6.62e-16 exp(+14928.92/T)	−34.9513	14928.92

B-3. MERCURY REMOVAL

SCR equipment is the dominant method for nitrogen oxide (NO) removal from coal combustion in CFPPs, in which NH_3 is used as the reducing agent. For the SCR process the common catalyst used is composed of by vanadium pentoxide (V_2O_5) and tungsten trioxide (WO_3) supported on titanium dioxide (TiO_2), at working temperatures of 300–400°C (Zhang et al. 2016). During operations, it is believed that NO is reduced by NH_3, which is injected upstream of the SCR at temperatures above 300°C. NH_3 strongly adsorbs to the V_2O_5 sites, and NO reacts to the adsorbed NH_3 to form N_2 and H_2O through the Eley-Rideal mechanism (Niksa and Fujiwara 2005). Similarly, it is assumed that HCl is adsorbed on the WO_3 portion of catalyst to produce active sites and later would react with gaseous or weakly bound Hg^0 (Niksa and Fujiwara 2005). This phenomenon and other possible heterogenous reactions that take place on the catalyst are described by the Langmuir-Hinshelwood mechanism (He et al. 2009).

The efficacy of the SCR process for mercury oxidization has been widely investigated at laboratory, pilot, and full scale for several levels of HCl concentrations, NO concentrations, NH_3/NO ratios, temperatures, and different coal types (Gutberlet et al. 2000; Richardson et al. 2002; Bock et al. 2003; Lee et al. 2003; Machalek et al. 2003; Hocquel 2004; Lee et al. 2004; Benson et al. 2005; Eswaran and Stenger 2005; Yue-yang et al. 2014). Laboratory and field tests on mercury concentration in flue gas at the inlet and outlet of SCR have verified that SCR has a co-effect on Hg^0 oxidation, where Hg^0 oxidizes to Hg^{2+}, particularly in presence of HCl (Yue-yang et al. 2014). Several studies have observed a direct correlation between the HCl concentration in simulated flue gas and the potential extent of mercury oxidation (Bock et al. 2003; Lee et al. 2003; Hocquel 2004; Lee et al. 2004; Eswaran and Stenger 2005). Therefore, it is confirmed that active Cl is the oxidizer for Hg^0 oxidation on the SCR catalyst surface, and Hg-Cl coupling and NO–NH_3 redox reactions occur on the active sites of SCR catalysts simultaneously (Zhang et al. 2016).

The ESPs have shown good performance in capturing Hg^p in flue gas, benefiting from high PM removal efficiency (> 99%). As mentioned before, along flue gas cooling, some parts of the Hg^0 and Hg^{2+} could be adsorbed onto fly ash to generate Hg^p, and a portion of Hg^0 might react with fly ash to produce Hg^{2+} or Hg^p as well. The mercury removal rate across ESP is influenced by flue gas temperature, mercury species in flue gas, and fly ash components (unburned carbon and metal oxides). High removal efficiencies (>86.73%) are seen for ESP co-capturing at around 375–400°C (Sung et al. 2017). ESP is a particulate control device that uses an electrical force (charge) to remove certain impurities to collection plates, particles passing through the precipitator are given a negative electrical charge by being forced to pass through a region, called a corona, where the gas ions flow. Once the particle has been negatively charged, it is forced to the positively charged plate and drops by gravity. Particles are removed from the plate by a knocking action (Kumar and Kumar 2018).

The performance of an ESP is significantly influenced by the resistivity of the particles in the flue gas. Particle resistivity is a property that determines how effectively particles are deposited and removed from the collection plates within the ESP. If the particles have very high resistivity, they are slow to conduct away their charge, causing a negative charge to build up on the plates, inhibiting other particles from depositing. If the particles have very low resistivity, they rapidly lose their charge when reaching the plate and pick up the charge of the plate, causing them to be repelled back into the gas stream where they are recharged negatively. The impurities removed by ESP have the desirable "moderate resistivity," meaning that they conduct away some of their charge when they reach the plate so as not to inhibit deposition of other particles, but they retain enough of their charge to hold them lightly to the plate. The decontaminated flue gas can pass through because of low resistivity.

WFGD reduces SO_2 emissions in flue gas (Zhao et al. 2019). Current designs can achieve more than 99% SO_2 removal, and 99.5% of WFGD systems are coupled to the SCR/ESP configuration. WFGD has a high removal rate of 83.45–94.53% (Zhao et al. 2019), capturing mercury in its various forms (PM, Hg^{2+}, and Hg^0) due to the high-water solubility of elemental and oxidized mercury in flue gas. However, re-emission of Hg^0 can happen during the Hg^{2+} removal process. This occurs because Hg^{2+} and Hg^0 in flue gas could combine into Hg_2^{2+} by dissolving in the water layer covering the external surface of the desulfurizer. Hg_2^{2+} can later react with OH^- to generate Hg^0 and HgO (Zhang et al. 2017), as shown in reactions 1, 2, and 3:

$$Hg^{2+} + Hg^0 \leftrightarrow {Hg_2}^{2+}$$ Reaction 1

$${Hg_2}^{2+} + 2OH^- \leftrightarrow H_2O + HgO + Hg^0$$ Reaction 2

$$HgO + SO_2 \leftrightarrow Hg^0 + SO_3$$ Reaction 3

It is also believed that dissolved Hg $^{2+}$ in a limestone-water solution could react with sulfite and sulfate to produce $HgSO_3$ and $HgSO_4$, where both sulfite and sulfate are formed from SO_2 dissolving in the scrubber solution. Some of the formed $HgSO_3$ and $HgSO_4$ may participate in further reactions to release Hg^0 (Zhao et al. 2017b). This is seen in reactions 4 and 5.

$$Hg^{2+} + {SO_3}^2 \rightarrow HgSO_3 \rightarrow Hg^0$$ Reaction 4

$$Hg^{2+} + {SO_4}^2 \rightarrow HgSO_4 \rightarrow Hg^0$$ Reaction 5

Although these reactions are possible, Hg^0 re-emission is mainly affected by process conditions such as the operating temperature, pH, O_2 concentration in flue gas, and transitional metal ions concentration.

Appendix C

Stream Information of Aspen Plus Model

Dryer Unit

Table C-1. Aspen model results for stream of dryer unit.

	Units	AIR-DRY	AIR-IN	AIR-WET	DRY-COAL
From		DRY-HT2		DRYER1	DRYER1
To		DRYER1	DRY-HT2	B7	DRY-PUP
Temperature	C	300	25	92.76139	92.76139
Pressure	bar	1.01325	1.01325	1.01325	1.01325
Mass Vapor Fraction		1	1	1	0
Mass Liquid Fraction		0	0	0	0
Mass Solid Fraction		0	0	0	1
Enthalpy Flow	MW	1.389692	−0.58811	−2.47058	−6.32622
Mass Flows	tonne/day	600	600	615.3535	984.6465
CHAR	tonne/day	0	0	0	0
COAL	tonne/day	0	0	0	984.6465
ASH	tonne/day	0	0	0	0
SAND	tonne/day	0	0	0	0
H2O	tonne/day	3.779622	3.779622	19.13316	0
CO	tonne/day	0	0	0	0
CO_2	tonne/day	0	0	0	0
CH4	tonne/day	0	0	0	0
C2H4	tonne/day	0	0	0	0
N2	tonne/day	471.0129	471.0129	471.0129	0
O2	tonne/day	125.2075	125.2075	125.2075	0
H2	tonne/day	0	0	0	0
H2S	tonne/day	0	0	0	0
NH3	tonne/day	0	0	0	0
HCL	tonne/day	0	0	0	0
BENZENE	tonne/day	0	0	0	0
MEOH	tonne/day	0	0	0	0

Pyrolysis Unit

Table C-2. Aspen model results for stream of pyrolysis unit.

	Unit	S1	S2	S3	S4	S5	S6	S7	S8	S9	S10	PYR-CHAR	SAND-IN	SAND-PUR
From				PY-MX1	PY-HT1	PYRO	CLS	CYCL1	PY-MX2	PIPE	NUC-HT	CLS		CYCL1
To		PY-MX1	PY-MX1	PY-HT1	PYRO	CLS	CYCL1	PY-MX2	PIPE	NUC-HT	PY-MX1		PY-MX2	
Temp.	C	92.76	74.39	500.94	500.00	500.00	500.00	500.00	498.24	498.24	750.00	500.00	25.00	500.00
Pressure	bar	5.00	5.00	5.00	5.00	5.00	5.00	5.00	5.00	4.99	4.99	5.00	5.00	5.00
Mass Vapor Fraction		0.00	1.00	0.51	0.51	0.62	0.70	0.71	0.70	0.70	0.70	0.49	0.00	0.00
Mass Liquid Fraction		0.00	0.00	0.00	0.00	0.00	0.00	0.00	0.00	0.00	0.00	0.00	0.00	0.00
Mass Solid Fraction		1.00	0.00	0.49	0.49	0.38	0.30	0.29	0.30	0.30	0.30	0.51	1.00	1.00
Enthalpy Flow [MW]		−6.33	−24.73	−193.36	−193.43	−194.10	−172.41	−170.38	−172.49	−172.49	−162.31	−21.69	−2.11	−2.03
Mass Flows	tonne/day	984.65	240.00	3222.94	3222.94	3222.98	1998.21	1986.27	1998.27	1998.27	1998.29	1224	12.00	11.94
CHAR	tonne/day	0.00	0.00	0.31	0.31	624.53	0.31	0.31	0.31	0.31	0.31	624.24	0.00	0.01
COAL	tonne/day	984.65	0.00	984.65	984.65	0.02	0.00	0.00	0.00	0.00	0.00	0.02	0.00	0.00
ASH	tonne/day	0.00	0.00	0.00	0.00	0.00	0.00	0.00	0.00	0.00	0.00	0.00	0.00	0.00
SAND	tonne/day	0.00	0.00	596.95	596.95	596.95	596.87	584.93	596.93	596.93	596.95	0.09	12.00	11.94
H2O	tonne/day	0.00	0.00	98.12	98.12	140.17	98.12	98.12	98.12	98.12	98.12	42.05	0.00	0.00
CO	tonne/day	0.00	0.00	127.76	127.76	182.51	127.76	127.76	127.76	127.76	127.76	54.75	0.00	0.00
CO_2	tonne/day	0.00	240.00	844.11	844.11	863.02	604.11	604.11	604.11	604.11	604.11	258.91	0.00	0.00
CH4	tonne/day	0.00	0.00	83.59	83.59	119.42	83.59	83.59	83.59	83.59	83.59	35.83	0.00	0.00
C2H4	tonne/day	0.00	0.00	0.00	0.00	0.00	0.00	0.00	0.00	0.00	0.00	0.00	0.00	0.00
N2	tonne/day	0.00	0.00	0.00	0.00	0.00	0.00	0.00	0.00	0.00	0.00	0.00	0.00	0.00
O2	tonne/day	0.00	0.00	0.00	0.00	0.00	0.00	0.00	0.00	0.00	0.00	0.00	0.00	0.00
H2	tonne/day	0.00	0.00	0.00	0.00	0.00	0.00	0.00	0.00	0.00	0.00	0.00	0.00	0.00
H2S	tonne/day	0.00	0.00	5.86	5.86	8.37	5.86	5.86	5.86	5.86	5.86	2.51	0.00	0.00
NH3	tonne/day	0.00	0.00	6.76	6.76	9.66	6.76	6.76	6.76	6.76	6.76	2.90	0.00	0.00
HCL	tonne/day	0.00	0.00	0.14	0.14	0.20	0.14	0.14	0.14	0.14	0.14	0.06	0.00	0.00
C6H6	tonne/day	0.00	0.00	474.69	474.69	678.12	474.69	474.69	474.69	474.69	474.69	203.44	0.00	0.00

Hydrothermal Gasification Unit

Table C-3. Aspen model results for stream of Hydrothermal Gasification Unit.

	Units	DIRT-H2O	GAS-IN	GAS-OUT1	GAS-OUT2	H2O-IN	HG1	HG2	HG3	HG4	HG5	HG6	HG7	HG8	HG9	HG10	S1	S2	S3	S4	TAR-RICH	WATER-1	WATER-2
From		FLASH3		HT9	FLASH3		MX1	PP1	HT3	HX5	HT6	RXT1	HT7	HX5	HT8	NZ1	HT1	FLASH1	HT2	FLASH2	FLASH2	HT1-B	FLASH1
To			HT1			HT1-B	PP1	HT3	HX5	HT6	RXT1	HT7	HX5	HT8	NZ1	FLASH3	FLASH1	HT2	FLASH2	HT9	MX1	MX1	MX1
Temp.	C	38.37	500.	40.00	38.37	25.00	39.28	44.21	120.	419	600.	600.	600.	250.	35.00	38.37	50.00	50.00	-40.00	-40.00	-40.00	41.38	50.00
Press.	bar	35.00	5.00	5.00	35.00	5.00	5.00	250.	250.	250.	250.	250.	250.	250.	250.	35.00	5.00	5.00	5.00	5.00	5.00	5.00	5.00
Mass Vapor Fraction		0.00	1.00	1.00	1.00	0.00	0.00	0.00	0.00	1.00	1.00	1.00	1.00	0.09	0.06	0.07	0.94	1.00	0.57	1.00	0.00	0.00	0.00
Mass Liquid Fraction		1.00	0.00	0.00	0.00	1.00	1.00	1.00	1.00	0.00	0.00	0.00	0.00	0.91	0.94	0.93	0.06	0.00	0.43	0.00	1.00	1.00	1.00
Mass Solid Fraction		0.00	0.00	0.00	0.00	0.00	0.00	0.00	0.00	0.00	0.00	0.00	0.00	0.00	0.00	0.00	0.00	0.00	0.00	0.00	0.00	0.00	0.00
Enthalpy Flow [MW]		-1266	-30.4	-28.1	-45.6	-1322	-1326	-1322	-1295	-1104	-1046	-1038	-1038	-1230	-1311	-1311	-36.23	-29.62	-31.75	-28.40	-3.34	-1316	-6.61
Mass Flows	tonne/day	6942.	600.	320.	537.8	7200.	7480.	7480.	7480.	7480.	7480.	7480	7480.	7480.	7480.	7480.	600.4	563.	563.3	320.2	243.0	7200.	37.09
CHAR	tonne/day	0.00	0.00	0.00	0.00	0.00	0.00	0.00	0.00	0.00	0.00	0.00	0.00	0.00	0.00	0.00	0.00	0.00	0.00	0.00	0.00	0.00	0.00
COAL	tonne/day	0.00	0.00	0.00	0.00	0.00	0.00	0.00	0.00	0.00	0.00	0.00	0.00	0.00	0.00	0.00	0.00	0.00	0.00	0.00	0.00	0.00	0.00
ASH	tonne/day	0.00	0.00	0.00	0.00	0.00	0.00	0.00	0.00	0.00	0.00	0.00	0.00	0.00	0.00	0.00	0.00	0.00	0.00	0.00	0.00	0.00	0.00
SAND	tonne/day	0.00	0.00	0.00	0.00	0.00	0.00	0.00	0.00	0.00	0.00	0.00	0.00	0.00	0.00	0.00	0.00	0.00	0.00	0.00	0.00	0.00	0.00
H2O	tonne/day	6885.	42.05	0.02	1.60	7200.	7242.	7242.	7242.	7242.	7242.	6886.	6886.	6886.	6886.	6886.	42.05	6.10	6.10	0.02	6.08	7200.	35.96
CO	tonne/day	0.19	54.75	53.13	33.87	0.00	1.62	1.62	1.62	1.62	1.62	34.06	34.06	34.06	34.06	34.06	54.75	54.75	54.75	53.13	1.62	0.00	0.00
CO2	tonne/day	55.15	258.9	223	382.0	0.00	28.99	28.99	28.99	28.99	28.99	437.	437.	437.	437.	437.2	258.9	258.8	258.8	229.9	28.92	0.00	0.07
CH4	tonne/day	0.66	35.83	35.39	82.65	0.00	0.44	0.44	0.44	0.44	0.44	83.32	83.32	83.32	83.32	83.32	35.83	35.83	35.83	35.39	0.43	0.00	0.00
C2H4	tonne/day	0.00	0.00	0.00	0.00	0.00	0.00	0.00	0.00	0.00	0.00	0.00	0.00	0.00	0.00	0.00	0.00	0.00	0.00	0.00	0.00	0.00	0.00
N2	tonne/day	0.01	0.00	0.00	1.75	0.00	0.00	0.00	0.00	0.00	0.00	1.75	1.75	1.75	1.75	1.75	0.00	0.00	0.00	0.00	0.00	0.00	0.00
O2	tonne/day	0.00	0.00	0.00	0.00	0.00	0.00	0.00	0.00	0.00	0.00	0.00	0.00	0.00	0.00	0.00	0.00	0.00	0.00	0.00	0.00	0.00	0.00
H2	tonne/day	0.20	0.00	0.00	34.81	0.00	0.00	0.00	0.00	0.00	0.00	35.01	35.01	35.01	35.01	35.01	0.00	0.00	0.00	0.00	0.00	0.00	0.00
H2S	tonne/day	0.34	2.51	1.12	1.06	0.00	1.39	1.39	1.39	1.39	1.39	1.39	1.39	1.39	1.39	1.39	2.51	2.51	2.51	1.12	1.39	0.00	0.00
NH3	tonne/day	0.41	2.90	0.36	0.00	0.00	2.54	2.54	2.54	2.54	2.54	0.41	0.41	0.41	0.41	0.41	2.90	2.22	2.22	0.36	1.86	0.00	0.67
HCL	tonne/day	0.06	0.06	0.00	0.00	0.00	0.06	0.06	0.06	0.06	0.06	0.06	0.06	0.06	0.06	0.06	0.06	0.00	0.00	0.00	0.00	0.00	0.06
C6H6	tonne/day	0.00	203.	0.33	0.00	0.00	203.	203.	203.	203.	203.	0.00	0.00	0.00	0.00	0.00	203.4	203.1	203.1	0.33	202.7	0.00	0.33
MEOH	tonne/day	0.00	0.00	0.00	0.00	0.00	0.00	0.00	0.00	0.00	0.00	0.00	0.00	0.00	0.00	0.00	0.00	0.00	0.00	0.00	0.00	0.00	0.00

Activated carbon process unit

Table C-4. Aspen model results for stream of Activated carbon process unit.

	Units	1	AC-1	AC-2	AC-3	AC-4	AC-5	AC-6	AC-FINAL	AC-WATER	FEED-H2O	S1	S2	S3	STEAM	SYNGAS3
From				B5	RSTOIC	SEP1	GASIFICA	B1	SEP1	B4		B	B2	B2	B3	B4
To		GASIFICA	B5	RSTOIC	SEP1	GASIFICA	B1	B4			B	B2	B3		GASIFICA	
Temperature	C	700	500	700	700	700	700	60	700	60	25	200	200		700	60
Pressure	bar	5	5	5	5	5	5	5	5	5	1	1	5	5	5	5
Mass Vapor Fraction		1	0	0	0.07965	0.27133	1	0.52429	0	0	0	1	1		1	1
Mass Liquid Fraction		0	0	0	0	0	0	0.47570	0	1	1	0	0		0	0
Mass Solid Fraction		0	1	1	0.92035	0.72866	0	0	1	0	0	0	0		0	0
Enthalpy Flow [MW]		2.80886	8.73995	11.6273	8.29003	4.17941	-91.225	-113.36	4.1106	-73.359	-57.901	-47.282	-47.323		-43.494	-40.001
Mass Flows	tonne/day	356.712	624.323	624.323	624.298	183.260	851.972	851.972	441.037	405.285	312	312	312	0	312	446.687
CHAR	tonne/day	0	624.216	624.216	0	0	0	0	0	0	0	0	0	0	0	0
COAL	tonne/day	0	0.02063	0.02063	0.02063	0	0	0	0.02063	0	0	0	0	0	0	0
ASH	tonne/day	0	0	0	102.309	0	0	0	102.309	0	0	0	0	0	0	0
SAND	tonne/day	0	0.08581	0.08581	0.08581	0	0	0	0.08581	0	0	0	0	0	0	0
H2O	tonne/day	0	0	0	0	0	404.245	404.245	0	394.368	312	312	312	0	312	9.87666
CO	tonne/day	0	0	0	0	0	28.5022	28.5022	0	0.05529	0	0	0	0	0	28.4469
CO_2	tonne/day	0	0	0	0	0	368.557	368.557	0	8.55473	0	0	0	0	0	360.002
CH4	tonne/day	0	0	0	0	0	0.08928	0.08928	0	0.00022	0	0	0	0	0	0.08906
C2H4	tonne/day	0	0	0	0	0	1.08E-8	1.08E-8	0	5.4E-11	0	0	0	0	0	1.07E-8
N2	tonne/day	0	0	0	19.6628	19.6628	19.6525	19.6525	0	0.01289	0	0	0	0	0	19.6396
O2	tonne/day	356.712	0	0	9.46312	9.46312	9.0E-18	9.0E-18	0	0	0	0	0	0	0	0
H2	tonne/day	0	0	0	20.5991	20.5991	8.95348	8.95348	0	0.00015	0	0	0	0	0	8.95333
H2S	tonne/day	0	0	0	0	0	21.9605	21.9605	0	2.29092	0	0	0	0	0	19.6695
NH3	tonne/day	0	0	0	0	0	0.01250	0.01250	0	0.00222	0	0	0	0	0	0.01028
HCL	tonne/day	0	0	0	0	0	0	0	0	0	0	0	0	0	0	0
BENZENE	tonne/day	0	0	0	0	0	1.3E-25	1.3E-25	0	0	0	0	0	0	0	0
MEOH	tonne/day	0	0	0	0	0	4.82E-7	4.82E-7	0	3.85E-7	0	0	0	0	0	9.79E-8
C	tonne/day	0	0	0	451.496	112.874	0	0	338.622	0	0	0	0	0	0	0
S	tonne/day	0	0	0	20.6615	20.6615	0	0	0	0	0	0	0	0	0	0

Autothermal Gasification Unit

Table C-5. Aspen model results for stream of Autothermal Gasification Unit.

	Units	A00	A0	A1	A2	A3	A4	A5	A6	A7	A8	A9
From		B10			B6	B5	B8	B9	B11	B1	B12	B12
To		B8	B10	B6	B5	B8	B9	B11	B1	B12		
Temperature	C	700.00	25.00	35.00	28.60	700.00	699.91	700.00	200.00	35.00	35.00	35.00
Pressure	bar	1.00	1.00	35.00	1.00	1.00	1.00	1.00	1.00	35.00	35.00	35.00
Mass Vapor Fraction		1.00	0.51	1.00	1.00	1.00	1.00	1.00	1.00	0.81	1.00	0.00
Mass Liquid Fraction		0.00	0.49	0.00	0.00	0.00	0.00	0.00	0.00	0.19	0.00	1.00
Mass Solid Fraction		0.00	0.00	0.00	0.00	0.00	0.00	0.00	0.00	0.00	0.00	0.00
Enthalpy Flow [MW]		-15.78	-21.98	-73.88	-73.88	-60.89	-76.67	-78.54	-91.13	-100.67	-63.37	-37.30
Mass Flows	tonne/day	240.00	240.00	858.09	858.09	858.09	1098.09	1098.09	1098.09	1098.09	893.87	204.23
CHAR	tonne/day	0.00	0.00	0.00	0.00	0.00	0.00	0.00	0.00	0.00	0.00	0.00
COAL	tonne/day	0.00	0.00	0.00	0.00	0.00	0.00	0.00	0.00	0.00	0.00	0.00
ASH	tonne/day	0.00	0.00	0.00	0.00	0.00	0.00	0.00	0.00	0.00	0.00	0.00
SAND	tonne/day	0.00	0.00	0.00	0.00	0.00	0.00	0.00	0.00	0.00	0.00	0.00
H2O	tonne/day	120.00	120.00	1.62	1.62	1.62	121.62	204.96	204.96	204.96	2.06	202.90
CO	tonne/day	0.00	0.00	87.00	87.00	87.00	87.00	394.13	394.13	394.13	394.08	0.04
CO_2	tonne/day	0.00	0.00	612.01	612.01	612.01	612.01	433.97	433.97	433.97	432.71	1.26
CH4	tonne/day	0.00	0.00	118.04	118.04	118.04	118.04	7.45	7.45	7.45	7.45	0.00
C2H4	tonne/day	0.00	0.00	0.00	0.00	0.00	0.00	0.00	0.00	0.00	0.00	0.00
N2	tonne/day	0.00	0.00	1.75	1.75	1.75	1.75	2.03	2.03	2.03	2.03	0.00
O2	tonne/day	120.00	120.00	0.00	0.00	0.00	120.00	0.00	0.00	0.00	0.00	0.00
H2	tonne/day	0.00	0.00	34.81	34.81	34.81	34.81	53.37	53.37	53.37	53.36	0.01
H2S	tonne/day	0.00	0.00	2.17	2.17	2.17	2.17	2.17	2.17	2.17	2.16	0.01
NH3	tonne/day	0.00	0.00	0.36	0.36	0.36	0.36	0.01	0.01	0.01	0.00	0.01
HCL	tonne/day	0.00	0.00	0.00	0.00	0.00	0.00	0.00	0.00	0.00	0.00	0.00
BENZENE	tonne/day	0.00	0.00	0.33	0.33	0.33	0.33	0.00	0.00	0.00	0.00	0.00
MEOH	tonne/day	0.00	0.00	0.00	0.00	0.00	0.00	0.00	0.00	0.00	0.00	0.00

Mercury removal Unit

Table C-6. Mercury removal block parameters on each unit and molar balance for each stream.

Material																
Stream Name	Units	FLUEGAS	ARTIF-HG	ARTI-HCL	ARTI-O2	HG+FLUEG	OXREDGAS	OXREDG-C	TO-HG2+X	TO-HGP	CLEANGA1	FLYASH1	CLEANGA2	SOLID-HG	CFLUEGAS	LIMESTO
Description																
From						MIXER4HG	SCR	HEAT-EX1	SPLIT	SPLIT	ESPHG2+X	ESPHG2+X	ESPHGP	HGREMOVE	CGAS-MIX	
To		MIXER4HG	MIXER4HG	MIXER4HG	MIXER4HG	SCR	HEAT-EX1	SPLIT	ESPHG2+X	ESPHGP	CGAS-MIX	HGREMOVE	CGAS-MIX		RADFRAC	RADFRA
Stream Class		MIXCIPSD	MIXCIPSD	MIXCIPSD	MIXCIPSD	MIXCIPSD	MIXCIPSD	MIXCIPSD	MIXCIPSD	MIXCIPSD	MIXCIPSD	MIXCIPSD	MIXCIPSD	MIXCIPSD	MIXCIPSD	MIXCIPSI
Temperature	C	400	400	400	400	400	400	220	220	220	220	220	220	219.730038	220	40
Pressure	bar	1.01325	1.01325	1.01325	1.01325	1.01325	1.01325	1.01325	1.01325	1.01325	1.013248354	1.01325	1.0132484	1.01325	1.013248	1.15
Molar Vapor Fraction		1	1	1	1	1	0.9999999	0.99999991	0.9999999	1	1	0	1	0	1	0
Molar Liquid Fraction		0	0	0	0	0	0	0	0	0	0	0	0	0	0	1
Molar Solid Fraction		0	0	0	0	0	9.33E-08	9.33E-08	9.33E-08	9.33E-08	9.33E-12	1	9.33E-12	1	9.33E-12	0
Mass Vapor Fraction		1	1	1	1	1	0.9999991	0.9999991	0.9999991	0.999999	1	0	1	0	1	0
Mass Liquid Fraction		0	0	0	0	0	0	0	0	0	0	0	0	0	0	1
Mass Solid Fraction		0	0	0	0	0	9.05E-07	9.05E-07	9.05E-07	9.05E-07	9.05E-11	1	9.05E-11	1	9.05E-11	0
Mole Flows	**kmol/hr**	**115.481573**	**8.59E-07**	**2.16E-05**	**4.05E-12**	**115.481595**	**115.48159**	**115.481594**	**57.740797**	**57.7408**	**57.74079174**	**5.39E-06**	**57.740792**	**1.08E-05**	**115.4816**	**1000**
NO	kmol/hr	0	0	0	0	0	0	0	0	0	0	0	0	0	0	0
NH3	kmol/hr	0.52196563	0	0	0	0.52196563	0.5219656	0.52196563	0.2609828	0.260983	0.260982813	0	0.2609828	0	0.521966	0
HG	kmol/hr	0	8.59E-07	0	0	8.59E-07	0	0	0	0	0	0	0	0	0	0
HCL	kmol/hr	0.00680262	0	2.16E-05	0	0.0068242	0.0068027	0.00680265	0.0034013	0.003401	0.003401327	0	0.0034013	0	0.006803	0
O2	kmol/hr	0	0	0	4.05E-12	4.05E-12	0	0	0	0	0	0	0	0	0	0
N2	kmol/hr	0.09095354	0	0	0	0.09095354	0.0909535	0.09095354	0.0454768	0.045477	0.04547677	0	0.0454768	0	0.090954	0
H2O	kmol/hr	3.31881035	0	0	0	3.31881035	3.3188211	3.31882112	1.6594106	1.659411	1.659410562	0	1.6594106	0	3.318821	1000
CO2	kmol/hr	48.0858326	0	0	0	48.0858326	48.085833	48.0858326	24.042916	24.04292	24.04291628	0	24.042916	0	48.08583	0
SO2	kmol/hr	0	0	0	0	0	0	0	0	0	0	0	0	0	0	0
HGCL2	kmol/hr	0	0	0	0	0	1.08E-05	1.08E-05	5.39E-06	5.39E-06	5.39E-10	5.39E-06	5.39E-10	1.08E-05	1.08E-09	0
CO	kmol/hr	9.16812412	0	0	0	9.16812412	9.1681241	9.16812412	4.5840621	4.584062	4.584062059	0	4.5840621	0	9.168124	0
CH4	kmol/hr	47.7082815	0	0	0	47.7082815	47.708281	47.7082815	23.854141	23.85414	23.85414074	0	23.854141	0	47.70828	0
H2S	kmol/hr	0.28910081	0	0	0	0.28910081	0.2891008	0.28910081	0.1445504	0.14455	0.144550404	0	0.1445504	0	0.289101	0
BENZENE	kmol/hr	0.01714589	0	0	0	0.01714589	0.0171459	0.01714589	0.0085729	0.008573	0.008572944	0	0.0085729	0	0.017146	0
H2	kmol/hr	6.27451879	0	0	0	6.27451879	6.2745188	6.27451879	3.1372594	3.137259	3.137259396	0	3.1372594	0	6.274519	0
TOLUENE	kmol/hr	0	0	0	0	0	0	0	0	0	0	0	0	0	0	0
AIR	kmol/hr	0	0	0	0	0	0	0	0	0	0	0	0	0	0	0
CALCI-01	kmol/hr	0	0	0	0	0	0	0	0	0	0	0	0	0	0	0
MEOH	kmol/hr	9.21E-06	0	0	0	9.21E-06	9.21E-06	9.21E-06	4.61E-06	4.61E-06	4.61E-06	0	4.61E-06	0	9.21E-06	0
C2H4	kmol/hr	2.77E-05	0	0	0	2.77E-05	2.77E-05	2.77E-05	1.38E-05	1.38E-05	1.38E-05	0	1.38E-05	0	2.77E-05	0
Total Mole Flow	**kmol/hr**	**115.481573**	**8.59E-07**	**2.16E-05**	**4.05E-12**	**115.481595**	**115.48159**	**115.481594**	**57.740797**	**57.7408**	**57.74079174**	**5.39E-06**	**57.740792**	**1.08E-05**	**115.4816**	**1000**
Mole Fractions																
Stream Name	Units	FLUEGAS	ARTIF-HG	ARTI-HCL	ARTI-O2	HG+FLUEG	OXREDGAS	OXREDG-C	TO-HG2+X	TO-HGP	CLEANGA1	FLYASH1	CLEANGA2	SOLID-HG	CFLUEGAS	LIMESTO
NO		0	0	0	0	0	0	0	0	0	0	0	0	0	0	0
NH3		0.0045199	0	0	0	0.0045199	0.0045199	0.0045199	0.0045199	0.00452	0.004519904	0	0.0045199	0	0.00452	0
HG		0	1	0	0	7.44E-09	0	0	0	0	0	0	0	0	0	0
HCL		5.89E-05	0	1	0	5.91E-05	5.89E-05	5.89E-05	5.89E-05	5.89E-05	5.89E-05	0	5.89E-05	0	5.89E-05	0
O2		0	0	0	1	3.51E-14	0	0	0	0	0	0	0	0	0	0
N2		0.0007876	0	0	0	0.0007876	0.0007876	0.0007876	0.0007876	0.000788	0.000787602	0	0.0007876	0	0.000788	0
H2O		0.02873887	0	0	0	0.02873887	0.028739	0.02873896	0.028739	0.028739	0.028738964	0	0.028739	0	0.028739	1
CO2		0.41639399	0	0	0	0.41639391	0.4163939	0.41639391	0.4163939	0.416394	0.416393949	0	0.4163939	0	0.416394	0
SO2		0	0	0	0	0	0	0	0	0	0	0	0	0	0	0
HGCL2		0	0	0	0	0	9.33E-08	9.33E-08	9.33E-08	9.33E-08	9.33E-12	0.9999	9.33E-12	0.9999	9.33E-12	0
CO		0.07939036	0	0	0	0.07939035	0.0793903	0.07939035	0.0793903	0.07939	0.079390357	0	0.0793904	0	0.07939	0
CH4		0.41312463	0	0	0	0.41312455	0.4131245	0.41312455	0.4131245	0.413125	0.413124587	0	0.4131246	0	0.413125	0
H2S		0.00250344	0	0	0	0.00250344	0.0025034	0.00250344	0.0025034	0.002503	0.002503436	0	0.0025034	0	0.002503	0
BENZENE		0.00014847	0	0	0	0.00014847	0.0001485	0.00014847	0.0001485	0.000148	0.000148473	0	0.0001485	0	0.000148	0
H2		0.05433351	0	0	0	0.0543335	0.0543335	0.0543335	0.0543335	0.054333	0.054333502	0	0.0543335	0	0.054334	0
TOLUENE		0	0	0	0	0	0	0	0	0	0	0	0	0	0	0
AIR		0	0	0	0	0	0	0	0	0	0	0	0	0	0	0
CALCI-01		0	0	0	0	0	0	0	0	0	0	0	0	0	0	0
MEOH		7.98E-08	0	0	0	7.98E-08	7.98E-08	7.98E-08	7.98E-08	7.98E-08	7.98E-08	0	7.98E-08	0	7.98E-08	0
C2H4		2.40E-07	0	0	0	2.40E-07	2.40E-07	2.40E-07	2.40E-07	2.40E-07	2.40E-07	0	2.40E-07	0	2.40E-07	0

Table C-7. Aspen model results for stream of Rectisol process Unit (continued, 1/3).

	Units	A1-1	A1-2	A2-1	A2-2	A2-3	A3-1	A3-2	A3-3	A3-4	A4-1	A4-2	A4-3	A4-4	INLET	LIGHTOUT	MEOH	MEOH-PUR
From		PM1	CL1	MX1	CP1	CL2	TW1	NZ1	B19	CP2	TW1	NZ2	B20	CP3		TW1		SP2
To		CL1	TW1	CP1	CL2	TW1	NZ1	B19	CP2	MX1	NZ2	B20	CP3	MX1	MX1		PM1	
Temp	°C	22.63	-50.00	229.21	334.07	-20.00	-11.17	-10.90	-10.90	109.40	-15.37	-15.40	-15.40	101.05	220.60	-45.24	20.00	20.00
Pressure	bar	60.00	60.00	35.00	60.00	60.00	60.00	19.80	19.80	60.00	60.00	20.00	20.00	60.00	35.00	60.00	1.20	1.20
Mass Vapor Fraction		0	0	0	1	1	0.997765	0	0.015207	1	1	0	0.01662	1	1	1	1	0
Mass Liquid Fraction		1	1	1	0	0	0.002235	1	0.984793	0	0	1	0.98338	0	0	0	0	1
Mass Solid Fraction		0	0	0	0	0	0	0	0	0	0	0	0	0	0	0	0	0
Enthalpy Flow [MW]		-133.5	-154.8	-157.8	-62.6	-60.5	-67.7	-135.5	-135.5	-1.9	-1.9	-70.2	-70.2	-1.1	-1.1	-59.6	-20.2	-155.1
Mass total	tonne/day	1800.0	1800.0	929.6	929.6	929.6	1500.1	1500.1	22.8	22.8	768.4	768.4	12.8	12.8	894.0	461.1	1800.0	1.8
CHAR	tonne/day	0	0	0	0	0	0	0	0	0	0	0	0	0	0	0	0	0
COAL	tonne/day	0	0	0	0	0	0	0	0	0	0	0	0	0	0	0	0	0
ASH	tonne/day	0	0	0	0	0	0	0	0	0	0	0	0	0	0	0	0	0
SAND	tonne/day	0	0	0	0	0	0	0	0	0	0	0	0	0	0	0	0	0
H2O	tonne/day	0	0	2.06	2.06	2.06	0.00	0.00	0.00	0.00	2.06	2.06	0.00	0.00	2.06	0.00	0.00	0.00
CO	tonne/day	0	0	403.87	403.87	403.87	9.68	9.68	6.43	6.43	5.05	5.05	3.36	3.36	394.08	389.14	0.00	0.00
CO2	tonne/day	0	0	457.47	457.47	457.47	274.53	274.53	15.62	15.62	173.04	173.04	8.99	8.99	432.86	9.90	0.00	0.00
CH4	tonne/day	0	0	7.80	7.80	7.80	0.65	0.65	0.23	0.23	0.33	0.33	0.12	0.12	7.45	6.82	0.00	0.00
C2H4	tonne/day	0	0	1.9E-05	1.9E-05	1.9E-05	8.2E-06	8.2E-06	7.7E-07	7.7E-07	4.2E-06	4.2E-06	3.6E-07	3.6E-07	1.8E-05	6.2E-06	0.0E+00	3.2E-18
N2	tonne/day	0	0	2.091848	2.091848	2.091848	0.060362	0.060362	0.037536	0.037536	0.031077	0.031077	0.019443	0.019443	2.034869	2.000409	0	0
O2	tonne/day	0	0	0	0	0	0	0	0	0	0	0	0	0	0	0	0	0
H2	tonne/day	0	0	54.059	54.059	54.059	0.558	0.558	0.464	0.464	0.279	0.279	0.233	0.233	53.363	53.223	0.000	0.000
H2S	tonne/day	0.000191	0.000191	2.201	2.201	2.201	0.153	0.153	0.003	0.003	2.049	2.049	0.038	0.038	2.161	0.000	0.000	0.000
NH3	tonne/day	0	0	0.001	0.001	0.001	0.000	0.000	0.000	0.000	0.001	0.001	0.000	0.000	0.001	0.000	0.000	0.000
HCL	tonne/day	0	0	0	0	0	0	0	0	0	0	0	0	0	0	0	0	0
C6H6	tonne/day	0	0	0	0	0	0	0	0	0	0	0	0	0	0	0	0	0
MEOH	tonne/day	1800	1800	0.039088	0.039088	0.039088	1214.454	1214.454	0.028329	0.028329	585.5432	585.5432	0.010762	0.010762	3.4E-07	0.041236	1800	1.751602

Table C-7 Aspen model results for stream of Rectisol process Unit (continued, 2/3).

	Units	B1-1	B1-2	B1-3	B1-4	B2-1	B2-2	B2-3	B3-1	B3-2	B3-3	B3-4	B4-1	B5-1	B5-2	B5-3	B6-1	B6-2	B7-1	B7-2	B8-1	B8-2	B10-1
From		B19	CL3	SP1	NZ3	B20	CL4	NZ4	TW2	CL6	B18	NZ5	B18	B23	CP4	CL5	B23	PM3	TW3	PM2	SP1	NZ6	TW3
To		CL3	SP1	NZ3	TW2	CL4	NZ4	TW2	CL6	B18	NZ5	B23	TW2	CP4	CL5	TW2	PM3	TW3	PM2	TW2	NZ6	TW3	CL7
Temp	°C	-10.90	-45.00	-45.00	-44.89	-15.40	20.00	20.00	-16.42	-17.00	-17.00	-32.36		-32.36	65.23	20.00	-32.36	-32.33	-44.01	-43.86	-45.00	-48.23	-20.87
Pressure	bar	19.80	19.80	19.80	6.00	20.00	6.00	6.00	6.00	6.00	6.00	2.00	6.00	2.00	6.00	6.00	2.00	2.70	2.70	6.00	19.80	2.70	2.70
Mass Vapor Fraction		0	0	0	0.0045	0	0.1749	0.1749	0	0	0	0.0814		1	1	1	0	0	0	0	0	0.0224	0
Mass Liquid Fraction		1	1	1	0.9954	1	0.8250	0.8250	1	1	1	0.9185		0	0	0	1	1	1	1	1	0.9775	1
Mass Solid Fraction		0	0	0	0	0	0	0	0	0	0	0		0	0	0	0	0	0	0	0	0	0
Enthalpy Flow [MW]		-133.5	-134.6	-121.1	-121.1	-69.1	-68.0	-68.0	-188.9	-189.0	-189.0	-189.0		-17.7	-17.5	-17.6	-171.3	-171.3	-9.7	-9.7	-13.5	-13.5	-173.0
Mass total	tonne/day	1477.3	1477.3	1329.5	1329.5	755.6	755.6	755.6	2094.9	2094.9	2094.9	2094.9	0.0	170.7	170.7	170.7	1924.2	1924.2	106.2	106.2	147.7	147.7	1951.1
CHAR	tonne/day	0	0	0	0	0	0	0	0	0	0	0	0	0	0	0	0	0	0	0	0	0	0
COAL	tonne/day	0	0	0	0	0	0	0	0	0	0	0	0	0	0	0	0	0	0	0	0	0	0
ASH	tonne/day	0	0	0	0	0	0	0	0	0	0	0	0	0	0	0	0	0	0	0	0	0	0
SAND	tonne/day	0	0	0	0	0	0	0	0	0	0	0	0	0	0	0	0	0	0	0	0	0	0
H2O	tonne/day	0.00	0.00	0.00	0.00	2.06	2.06	2.06	2.06	2.06	2.06	2.06	0.00	0.00	0.00	0.00	2.06	2.06	0.00	0.00	0.00	0.00	2.06
CO	tonne/day	3.25	3.25	2.93	2.93	1.69	1.69	1.69	0.00	0.00	0.00	0.00	0.00	0.00	0.00	0.00	0.00	0.00	0.00	0.00	0.33	0.33	0.00
CO2	tonne/day	258.91	258.91	233.02	233.02	164.05	164.05	164.05	323.51	323.51	323.51	323.51	0.00	169.69	169.69	169.69	153.82	153.82	18.36	18.36	25.89	25.89	147.08
CH4	tonne/day	0.42	0.42	0.38	0.38	0.22	0.22	0.22	0.00	0.00	0.00	0.00	0.00	0.00	0.00	0.00	0.00	0.00	0.00	0.00	0.04	0.04	0.00
C2H4	tonne/day	7.5E-6	7.5E-6	6.7E-6	6.7E-6	3.8E-6	3.8E-6	3.8E-6	1.8E-6	1.8E-6	1.8E-6	1.8E-6	0	1.2E-6	1.2E-6	1.2E-6	5.5E-7	5.5E-7	1.2E-7	1.2E-7	7.5E-7	7.5E-7	4.7E-7
N2	tonne/day	0.0228	0.0228	0.0204	0.0205	0.0116	0.0116	0.0116	1.E-10	1.E-10	1.E-10	1.E-10	0	1.E-10	1.E-10	1.E-10	2.E-12	2.E-12	1.E-11	1.E-11	0.0023	0.0023	5E-23
O2	tonne/day	0	0	0	0	0	0	0	0	0	0	0	0	0	0	0	0	0	0	0	0	0	0
H2	tonne/day	0.095	0.095	0.085	0.085	0.045	0.045	0.045	0.000	0.000	0.000	0.000	0.000	0.000	0.000	0.000	0.000	0.000	0.000	0.000	0.009	0.009	0.000
H2S	tonne/day	0.150	0.150	0.135	0.135	2.011	2.011	2.011	2.862	2.862	2.862	2.862	0.000	0.713	0.713	0.713	2.149	2.149	0.044	0.044	0.015	0.015	2.117
NH_3	tonne/day	0.000	0.000	0.000	0.000	0.001	0.001	0.001	0.001	0.001	0.001	0.001	0.000	0.000	0.000	0.000	0.001	0.001	0.000	0.000	0.000	0.000	0.001
HCL	tonne/day	0	0	0	0	0	0	0	0	0	0	0	0	0	0	0	0	0	0	0	0	0	0
C6H6	tonne/day	0	0	0	0	0	0	0	0	0	0	0	0	0	0	0	0	0	0	0	0	0	0
MEOH	tonne/day	1214.4	1214.4	1092.9	1092.9	585.53	585.53	585.53	1766.4	1766.4	1766.4	1766.4	0	0.2499	0.2499	0.2499	1766.1	1766.1	87.82	87.82	121.44	121.44	1799.8

Table C-7. Aspen model results for stream of Rectisol process Unit (3/3).

	Units	C0	C1-1	C1-2	C2-1	C2-2	C2-3	C4	CO2-OUT1	CO2-OUT2	H2SOUT
From		TW4	CL7	NZ7	TW4	CL8	SP2	MX3	TW2	TW3	CL9
To		CL9	NZ7	TW4	CL8	SP2	MX3				
Temp	°C	-46.33	-40.00	-41.93	69.71	20.00	20.00	20.00	-29.99	-45.28	20.00
Pressure	bar	1.20	2.70	1.20	1.20	1.20	1.20	1.20	6.00	2.70	1.20
Mass Vapor Fraction		1	0	0.0100	0	0	0	0	1	1	1
Mass Liquid Fraction		0	1	0.990	1	1	1	1	0	0	0
Mass Solid Fraction		0	0	0	0	0	0	0	0	0	0
Enthalpy Flow [MW]		-15.3	-173.8	-173.8	-153.1	-155.4	-155.3	-155.3	-27.5	-1.5	-15.3
Mass total	tonne/day	149.3	1951.1	1951.1	1801.8	1801.8	1800.0	1800.0	267.2	14.7	149.3
CHAR	tonne/day	0	0	0	0	0	0	0	0	0	0
COAL	tonne/day	0	0	0	0	0	0	0	0	0	0
ASH	tonne/day	0	0	0	0	0	0	0	0	0	0
SAND	tonne/day	0	0	0	0	0	0	0	0	0	0
H2O	tonne/day	0.00	2.06	2.06	2.06	2.06	2.06	2.06	0.00	0.00	0.00
CO	tonne/day	0.00	0.00	0.00	0.00	0.00	0.00	0.00	4.62	0.33	0.00
CO2	tonne/day	147.08	147.08	147.08	0.00	0.00	0.00	0.00	261.62	14.26	147.08
CH4	tonne/day	0.00	0.00	0.00	0.00	0.00	0.00	0.00	0.59	0.04	0.00
C2H4	tonne/day	4.7E-07	4.7E-7	4.7E-7	3.3E-15	3.3E-15	3.3E-15	3.3E-15	1.0E-5	7.0E-7	4.7E-7
N2	tonne/day	0	4E-23	4E-23	0	0	0	0	0.0321	0.0022	0
O2	tonne/day	0	0	0	0	0	0	0	0	0	0
H_2	tonne/day	0.000	0.000	0.000	0.000	0.000	0.000	0.000	0.130	0.009	0.000
H2S	tonne/day	2.117	2.117	2.117	0.000	0.000	0.000	0.000	0.041	0.003	2.117
NH3	tonne/day	0.001	0.001	0.001	0.000	0.000	0.000	0.000	0.000	0.000	0.001
HCL	tonne/day	0	0	0	0	0	0	0	0	0	0
C6H6	tonne/day	0	0	0	0	0	0	0	0	0	0
MEOH	tonne/day	0.109185	1799.8	1799.8	1799.6	1799.6	1797.9	1797.9	0.1502	0.0051	0.1091

Methanol synthesis Unit

Table C-8. Aspen model results for stream of Methanol synthesis Unit

	Units	FLS-G1	FLS-L1	FLS-L2	GAS	GAS-OUT	H2O	INLET	MEOH	MEOH-H2O	PURGE	PURGE2	RF-1	RF-2	RX0	RX1A	RX2	RX3	S1	S3	S4
From		ME-FLASH	ME-FLASH	ME-NZ1	ME-DIST1	ME-MX3	ME-DIST2		ME-DIST2	ME-DIST1	ME-SPLIT	ME-NZ2	ME-SPLIT	ME-HT3	ME-MX1	ME-PLUG	ME-MIX2	ME-HT2		B3	B3
To		ME-SPLIT	ME-NZ1	ME-DIST1	ME-MX3			ME-MX1		ME-DIST2	ME-NZ2	ME-MX3	ME-HT3	ME-MX1	B3	ME-MIX2	ME-HT2	ME-FLASH	ME-MX1	ME-PLUG	ME-EQUIL
Temperature	C	40.00	40.00	41.11	-14.04	53.93	179.85	280.00	135.41	135.01	40.00	54.81	40.00	280.00	279.63	279.63	279.63	40.00	280.00	279.63	279.63
Pressure	bar	50.00	50.00	10.00	10.00	1.50	10.00	50.00	10.00	10.00	50.00	1.50	50.00	50.00	50.00	50.00	50.00	50.00	50.00	50.00	50.00
Mass Vapor Fraction		1.00	0.00	0.00	1.00	1.00	0.00	1.00	1.00	0.00	1.00	1.00	1.00	1.00	1.00	1.00	1.00	0.67	1.00	1.00	1.00
Mass Liquid Fraction		0.00	1.00	1.00	0.00	0.00	1.00	0.00	0.00	1.00	0.00	0.00	0.00	0.00	0.00	0.00	0.00	0.33	0.00	0.00	0.00
Mass Solid Fraction		0.00	0.00	0.00	0.00	0.00	0.00	0.00	0.00	0.00	0.00	0.00	0.00	0.00	0.00	0.00	0.00	0.00	0.00	0.00	0.00
Enthalpy Flow [MW]		-24.69	-35.31	-35.31	-0.41	-2.87	-0.23	-15.47	-28.34	-33.13	-2.47	-2.47	-22.22	-11.28	-25.71	-40.02	-40.02	-60.00	1.03	-25.71	-25.71
Mass Flows	tonne/day	809.62	404.15	404.15	4.82	85.78	1.32	461.12	398.00	399.33	80.96	80.96	728.65	728.64	1213.7	1213.7	1213.7	1213.7	24.00	1213.7	1213.7
CHAR	tonne/day	0	0	0	0	0	0	0	0	0	0	0	0	0	0	0	0	0	0	0	0
COAL	tonne/day	0	0	0	0	0	0	0	0	0	0	0	0	0	0	0	0	0	0	0	0
ASH	tonne/day	0	0	0	0	0	0	0	0	0	0	0	0	0	0	0	0	0	0	0	0
SAND	tonne/day	0	0	0	0	0	0	0	0	0	0	0	0	0	0	0	0	0	0	0	0
H2O	tonne/day	0.04	1.72	1.72	0.00	0.00	1.32	0.00	0.40	1.72	0.00	0.00	0.04	0.04	0.04	1.77	1.77	1.77	0.00	0.04	0.04
CO	tonne/day	413.82	1.22	1.22	1.22	42.61	0.00	389.14	0.00	0.00	41.38	41.38	372.43	372.44	761.58	415.04	415.04	415.04	0.00	761.58	761.58
CO_2	tonne/day	21.84	3.50	3.50	3.10	5.29	0.00	9.90	0.40	0.40	2.18	2.18	19.66	19.66	29.56	25.35	25.35	25.35	0.00	29.56	29.56
CH4	tonne/day	63.42	0.47	0.47	0.47	6.81	0.00	6.82	0.00	0.00	6.34	6.34	57.08	57.08	63.89	63.89	63.89	63.89	0.00	63.89	63.89
C2H4	tonne/day	4.87E-5	1.37E-6	1.37E-6	1.37E-6	6.24E-6	1.1E-24	6.24E-6	3.86E-9	3.86E-9	4.87E-6	4.87E-6	4.38E-5	4.38E-5	5.01E-5	5.01E-5	5.01E-5	5.01E-5	0	5.01E-5	5.01E-5
N_2	tonne/day	19.807	0.018	0.018	0.018	1.999	0.000	2.000	0.000	0.000	1.981	1.981	17.826	17.825	19.825	19.825	19.825	19.825	0.000	19.825	19.825
O2	tonne/day	0	0	0	0	0	0	0	0	0	0	0	0	0	0	0	0	0	0	0	0
H_2	tonne/day	267.47	0.001	0.001	0.001	26.748	0.000	53.223	0.000	0.000	26.747	26.747	240.72	240.71	317.93	267.47	267.47	267.47	24.000	317.93	317.93
H2S	tonne/day	5.88E-5	1.72E-5	1.72E-5	7.35E-7	6.62E-6	2.0E-16	2.30E-5	1.64E-5	1.64E-5	5.88E-6	5.88E-6	5.29E-5	5.29E-5	7.60E-5	7.60E-5	7.60E-5	7.60E-5	0	7.60E-5	7.60E-5
NH_3	tonne/day	0	0	0	0	0	0	2.5E-18	0	0	0	0	0	0	2.5E-18	2.5E-18	2.5E-18	2.5E-18	0	2.5E-18	2.5E-18
HCL	tonne/day	0	0	0	0	0	0	0	0	0	0	0	0	0	0	0	0	0	0	0	0
BENZENE	tonne/day	0	0	0	0	0	0	0	0	0	0	0	0	0	0	0	0	0	0	0	0
MEOH	tonne/day	23.21	397.21	397.21	0.00	2.33	0.00	0.04	397.21	397.21	2.32	2.32	20.89	20.88	20.93	420.42	420.42	420.42	0.00	20.93	20.93

Appendix D

Compiled Data from Literature

Table D-1. Summary of Pittsburgh #8 coal attributes for different sample

Ref	(1)	(2)		(3)	(3)		(3)	(3)	
	PSOC-1451			APCS4	DECS12		DECS23	DECS34	
Location	Washington PA	Not mentioned		Greene PA	Greene PA		Washington PA	Washington PA	
Year	1985			1986	1989		1994	2004	
Proximate									
Moisture	2.54 (As rec'd)	2.4 (As rec'd)							
Ash (Dry)	13.67	10.25		9.00	10.30		9.40	7.40	
VM (Dry)	34.43	36.07		36.34	34.77		37.11	36.82	
FC (Dry)	51.9	53.69		52.73	53.49		50.61	54.32	
Ultimate									
Ash (Dry)	13.67	10.25		9.00	10.30		9.40	7.40	
C (Dry)	71.88	74.77		75.71	74.76		74.21	78.11	
H (Dry)	4.67	5.12		4.81	5.12		5.09	5.19	
N (Dry)	1.36	1.26		-	-		-	-	
S (Dry)	1.36	1.17		2.19	1.12		3.87	1.58	
Cl (Dry)	0.08	0.21		-	-		-	-	
O (Dry, diff)	6.99	7.22**		6.89*	7.3*		6.03*	6.32*	
MM	15.51	11.71		10.92	11.74		12.28	8.86	
C (DMMF)	85.08	84.68		85.00	84.70		84.60	85.70	
H (DMMF)	5.53	5.79		5.40	5.80		5.80	5.70	
H/C ratio	0.78	0.82	0.76	0.82	0.82	0.80	0.77	0.90	0.81
Sulfur									
Pyritic	0.82						1.37		3.15
Sulfatic	0.01						0.01		0.12
Organic	0.53						0.81		1

Major Element									
SIO2	3.36	5.72							
AL2O3	1.71	2.64							
TIO2	0.09	0.12							
Fe2O3	0.85	0.65							
MgO	0.07	0.09							
CaO	0.28	0.33							
Na2O	0.06	0.05							
K2O	0.22	0.22							
P2O5	0.02	0.06							
SO3	0.12	0.22							

* Calculated with assumption that nitrogen's weight percent of 1.4% and.
** Amount of Chlorine was not accounted on oxygen calculation in original data. Amount of Oxygen is changed accordingly.
*** Original date was 16.12, which was too big compared with other reference data. we subtracted amount of ash from original data of oxygen data.

Table D-2. Result of ultimate analysis for char produced from the Pittsburgh #8 coal in different conditions.

Condition			Ultimate Analysis					
Temp [°C]	Size [µm]	Res. Time [ms]	Ash	C	H	N	O	S
Fletcher and Hardesty (1992)								
Coal[!]			13.67	83.26	5.41	1.58	8.10	1.58
1050	106–125	337	15.9	82.49	4.09	1.87	10.26	1.29
1250	106–125	254	18.2	88.79	2.99	1.74	5.24	1.24
1050	63–75	287	8.6	86.29	3.79	1.89	7.03	1
1050	63–75	287	8.44	85.33	3.89	1.89	8.03	0.85
1250	63–75	288	8.75	89.77	2.33	1.77	5.3	0.84
Watt (1996)								
Coal			4.11	84.7	5.4	1.71	6.19*	2.00*
850		140	—	84.93	5.43	1.25	6.39*	2.00*
900		160	—	83.73	3.9	1.86	8.51*	2.00*
1050		210	—	88.11	3.32	1.91	4.66*	2.00*

Condition			Ultimate Analysis					
Temp [°C]	Size [µm]	Res. Time [ms]	Ash	C	H	N	O	S
1220		230	—	91.36	2.51	2.03	2.10*	2.00*
1650		15	—	92.44	1.55	1.69	2.32*	2.00*
Hambly (1998)								
Coal			4.29	82.77	5.61	1.74	8.9	0.98
820	63–75	170	4.03	84.9	5.49	1.8	6.58	1.24
1080	63–75	285	7.36	89.83	3.6	2.1	3.63	0.84
1220	63–75	412	8.18	93.59	2.6	2.14	0.87	0.8
Perry (2000)								
Coal			—	82.77	5.48	1.64	6.73	3.38
950		263	—	82.46	4.06	1.78	5.73	5.97
1000		252	—	87.49	3.37	1.92	3.41	3.82
1100		234	—	87.99	3.08	1.78	3.43	3.72
1250		294	—	92.18	1.72	1.76	0.66	3.68
1650		18	—	88.56	2.64	1.73	2.59	4.48
Rowan et al. (2014)								
Coal			10.65	81.53	6.12	3.27	6.35**	2.73
500	300–500	—	16.39	86.51	3.95	3.77	1.81**	3.96
500	850–1000	—	14.73	89.61	3.87	2.93	0.5**	3.08

Dry ash-free basis is assumed if a specific basis is not mentioned. Ash is written for a dry basis.

! Chlorine amount of 0.09% in DAF.

* Amount of sulfur of 2% is assumed to calculate amount of oxygen.

** Original date was too big compared with other reference data. We subtracted the amount of ash from original data of oxygen data.

Table D-3. Compilation of various APCDs in CFPP around the world (Zhao et al. 2019).

Coal Type	Boiler Type & Capacity (MW)	APCDs Configuration	Hg^0 oxi. Rate by SCR (%)	Mercury Removal Rate (%)				Countries
				ESP (or ESP+FF)	WFGD	WESP	APCDs (Hg^t)	
Lignite	PC-2*300	SCR+ESP+WFGD	—	—	94.53(Hg^{2+}); 67.38(Hg^t)	—	—	China

Coal Type	Boiler Type & Capacity (MW)	APCDs Configuration	Hg^0 oxi. Rate by SCR (%)	Mercury Removal Rate (%)				Countries
				ESP (or ESP+FF)	WFGD	WESP	APCDs (Hg^t)	
Lignite	CFB-2*135	ESP+FF+WFGD	—	—	87.39(Hg^{2+}); 50.50(Hg^t)	—	—	China
Bituminous	PC-150	MCS+FF	—	—	-	—	—	Canada
Bituminous	PC-300	ESP	—	22.80 (ESP)	—	—	22.8	China
Bituminous	PC-600	ESP+WFGD	—	28.33 (ESP)	16.73 (Hg^t)	—	40.57	China
Bituminous	PC-500,600	SCR+ESP+WFGD	6.5–73.8	28.3–64.7 (ESP)	7.9–42.3 (Hg^t)	—	43.8–71.4	South Korea
Bituminous	PC-500,600	ESP+WFGD	—	32.7–54.2 (ESP)	3.9–9.1 (Hg^t)	—	35.3–58.4	
Not specified	PC-190	SCR+ESP+WFGD	71	—	89.5- 98.0(Hg^{2+}) 54.9- 90.2 (Hg^t)	—	—	Not specified
Subbituminous	PC-225, 370	ESP + WFGD, SNCR + ESP + WFGD	—	65 (ESP)	19–38 (Hg^t)	—	72–84	Poland
Lignite	PC-370	ESP + WFGD	—		38 (Hg^t)	—		
bituminous	PC-300	SCR+ESP+SWFGD	57−64	—	67–82 (SWFGD, Hg^{2+})	—	69	Not specified
Bituminous	PC-800	SCR+ESP+WFGD	45.4	68.5–77 (ESP)	45.4–55.5 (Hg^t)	—	87–89.5	South Korea
Semi-anthracite	PC-400	ESP+WFGD	—	43.2 (ESP)	70.5 (Hg^t)	—	83.2	
Bituminous	PC-200,600	ESP+WFGD	—	24 (ESP)	—	—	73	China
Anthracite	PC-300	ESP+WFGD	—		—	—		
Lignite	PC-600	ESP+WFGD	—		—	—		
Bituminous	PC-100	ESP+(CFB-FGD)+FF	—		—	—	66	
Lignite	PC-165	SCR+ESP+WFGD	—		—	—	—	
Anthracite	PC	ESP	—	>51 (ESP)	—	—	>51	South Korea
Bituminous	PC	ESP+EFGD	—	—	—	—	59	
Bituminous	PC	SCR+ESP+WFGD	—	—	—	—	69	
Not specified	PC-50-600	ESP, ESP+WFGD, FF	—	11.5 (ESP), 52.3 (FF)	—	—	—	China
Not specified	CFB-135	ESP	—		—	—	—	
Bituminous	PC-98-758	ESP+WFGD	—	—	—	—	51.8	China
Anthracite	PC-162	ESP+WFGD	—	—	—	—		
Bituminous	PC-200	SCR+ESP+WFGD	—	-	-	-	87.6	China
Not specified	PC-300, 330	SCE+LTE+ESP+WFGD+WESP	41.43, 47.68	41.47 (ESP)	65.36, 66.93 (Hg^t)	47.42,	88.57,	China

Coal Type	Boiler Type & Capacity (MW)	APCDs Configuration	Hg^0 oxi. Rate by SCR (%)	Mercury Removal Rate (%)				Countries
				ESP (or ESP+FF)	WFGD	WESP	APCDs (Hg^t)	
						34.52	89.07	
Not specified	PC-330	SCR+LTE+ESP+WFGD	51.61	43.04 (ESP)	54.81 (Hg^t)	—	76.4	
Bituminous, Lignite	PC-350	SCR+(ESP+FF)+WFGD	50.13- 67.68	99.95–99.97 (Hg^p) (ESP+FF)	—	—	58.78- 73.32	China
Bituminous	PC-660	SCR+ESP+WFGD+WESP	45.47	—	83.45 (Hg^{2+})	—	56.59	China
Bituminous, Bituminous& petroleum coke	CFB-410t/h	SNCR+ESP+(IFD-WFGD), SNCR+FF+(IFD-WFGD)	—	68.3 (ESP), 70.0–71.6 (FF)	11.32–42.41 (Hg^t)	—	73.4–81.8	China
Bituminous	PC-500, 600	SCR+ESP+WFGD	7.3–79.9	71.3–90.4 (ESP)	26.3–66.2 (Hg^t)	-	89.5–94.9	South Korea
Anthracite& semi-anthracite	PC-400	ESP+WFGD, ESP+FF+WFGD	—	—	—	—	62.44 (without FF), 86.73(with FF)	
Not specified	Not specified	—	—	—	8–72 (av.54, Hg^t)	—	—	Not specified
Not specified	Not specified	—	—	24–49.6 (ESP, av.33.17), 28.5–90(FF, av. 67.92)	30.9–70(av.57.22, Hg^t)	—	—	Not specified
Bituminous	PC	CS ESP CS ESP+ FGD CS ESP+ FGD+SCR	—	50 (CS ESP)	—	—	75 (CS ESP+WFGD);90 (SCR+CS ESP+WFGD)	Netherlands
Subbituminous	PC-810	low-NOx system+wet venturi FGD system	—	—	17.61(av., wet venturi FGD system)	—	34.5 (boiler modification)	the U.S.

PC: Pulverized coal furnace; CFB: Circulating fluidized bed furnace; HA: hopper A; HB: Hopper B; SNCR: Selective non-catalytic reduction; SCR: Selective catalytic reduction; ESP: Electrostatic precipitator; FF: Fabric filter; WFGD: Wet flue gas desulfurization; WESP: Wet electrostatic precipitator; MCS: Mechanical cyclone separator; SWFGD: Seawater flue gas desulfurization; LTE: Low-temperature economizer; IFD: In-furnace desulphurization; WFGD&WESP: WFGD and WESP integration system; av.: Average value.